Trinity College Dublin
Coláiste na Tríonóide, Baile Átha Cliath
The University of Dublin

School of Physics

Foams and Complex Systems

Arrangements of lines of hard and soft spheres in confinement

John Ryan-Purcell

Supervisor: Prof. Stefan Hutzler

February 18, 2024

A dissertation submitted in partial fulfilment
of the requirements for the degree of
PhD Physics

Declaration

I hereby declare that this dissertation is entirely my own work and that it has not been submitted as an exercise for a degree at this or any other university.

I have read and I understand the plagiarism provisions in the General Regulations of the University Calendar for the current year, found at `http://www.tcd.ie/calendar`.

I have completed the Online Tutorial on avoiding plagiarism 'Ready Steady Write', located at `http://tcd-ie.libguides.com/plagiarism/ready-steady-write`.

Signed: John Ryan Purcell Date: *18/02/2024*

Abstract

Chains of particles, ranging from one-dimensional to three-dimensional structures, offer an avenue of research spanning condensed matter physics to microengineering, providing insights into material behavior across diverse length scales. In this thesis we examine a system of a line of contacting spheres, placed in a transverse confining potential, which may buckle under compression or when tilted away from the horizontal, once a critical tilt angle is exceeded. We examine this system for both the case of hard and soft spheres, through the use of computer simulations and analytical calculations. We compare our results to existing experimental work.

For the case of hard spheres, under infinitesimal compression and/or tilt, the spheres form a zig-zag pattern. These structures may be calculated using a recursion relationship based on the condition of mechanical equilibrium and geometrical constraints. For small sphere displacements, we propose a continuous formulation of these iterative equations in the form of a second-order differential equation. We explore solutions to this equation numerically, but we also find approximate analytic expressions in terms of the Jacobi, Whittaker and Airy functions.

The analysis of Whittaker functions yields exact results for the case of tilting without compression. Airy functions yield results for profiles that are both tilted and compressed. For the case of compression without tilting, we provide a detailed analysis of the relevant Jacobi functions. This analysis gives further insight into the localised nature of the buckling at small compression.

We also extend our analysis to the case of a line of contacting bubbles (soft spheres), placed in a transverse confining potential, under compression. We implement the Morse-Witten theory, which is based on a linearised version of the Laplace-Young equation, to describe bubbles under the action of applied forces. We develop a simulation method for a system of Morse-Witten bubbles which we use to find structures of bubbles in mechanical equilibrium. We find these structures correspond to the analytical and experimental work presented in this thesis.

Finally, we present an outlook for how this work may be extended in the future. We discuss how the continuum model may be generalised for a variety of boundary conditions, or how it may be used to find further mechanically stable structures. The Morse-Witten model simulations may be extended to larger systems, and without the confining potential, may be used to simulate dense packings of bubbles, i.e. foams.

Acknowledgements

"A straight line may be the shortest distance between two points, but it is by no means the most interesting." - The Third Doctor, Jon Pertwee

And what a winding road it has been to get here. The last four years have been full of ups and downs, both personally and globally. Never did I think that for most of four years I would be working from the desk in my bedroom, but COVID changed the landscape of research completely. It is a testament to the people around me that I have been able to make it this far, and I'd like to thank them here.

To Stefan Hutzler, my supervisor, for his usupport, guidance and mentorship. I could not have asked for a more hands-on supervisor, and our extended calls and meetings over the pandemic were instrumental in keeping my research on track. Similarly I am deeply grateful to Denis Weaire, who provided constructive feedback and insightful suggestions. Our chats in his office have greatly enriched the quality of this thesis.

I would like to acknowledge the financial support provided by Microgravity Application Project by ESA, which made this research possible. I enjoyed our discussions, even though they were limited to online meetings! Hopefully we will be able to meet in person. Special thanks also to the School of Physics, who ensured that my stipend "moved with the times" and facilitated me staying in Dublin.

To the Foams and Complex Systems group, both present and former members, I am indebted. Your camaraderie and our stimulating group meeting discussions have made this not only a productive journey, but an enjoyable one. In particular I'd like to thank Ali Irannezhad and Jennifer Quirke, without whom this thesis would be bereft of experimental images and data! I'd also like to thank the summer students with whom I worked closely and who provided real improvements to my simulations: Aleksander Prymek and Mikey Whelan. Also I'd like to thank Adil Mughal of Aberystwyth University, who helped provide many complementary simulations to help keep my work

on track.

To all those who assisted me in the writing of this thesis, thank you for both your time and patience. To Jens Winkelmann, who ensured that the introduction was not a terrifying wall of text and to Conor Murphy, who found countless errors that had slipped through the cracks.

I am lucky to count many of the people named above as friends, and there are many others who helped me so much on this journey: my weekly chats with Dave Holland, ranking up with the Smite crew and Commander nights with the gang. However my long-suffering roommate-housemate-friend Luke Gayer deserves a special mention. He is coming to the end of his own PhD journey, and I hope that our chats about "anything other than the thesis" were as much of a relief to him as they were to me. He's been my best study partner since secondary school. Best of luck in what you do next, my friend.

To my family, who have had to put up with some months of "radio silence" from me recently, I owe everything. Without their love and support, none of this would have been possible at all. They have been right with me from beginning to end. I love you all.

My grandmother Rita passed away after a long battle with Parkinsons, just a few months before the submission of this thesis. She was a constant supporter of me, and even helped me move up to Dublin at the start of my undergraduate in 2015. Thank you Granny.

E finalmemente, pra meu amorzão, Aldren, obrigado por tudo. You were at my side through thick and tin, and have been an unwavering source of support. Te amo.

Thank you everyone, go n-éirí an bóthar libh,

John

October 2023

List of Publications

Listed here are the publications to which I contributed during the course of this PhD program, in reverse chronological order. Material in this thesis is based on these published papers, the relevant chapters are indicated here.

- Jing, Z., Feng, C., Ryan-Purcell, J., and Hutzler, S. (2024). *Equilibrium shape of a bubble in a liquid-filled horizontal capillary.* International Journal of Multiphase Flow, Volume 172
- Hutzler, S., Ryan-Purcell, J., Mughal, A., and Weaire, D. (2023). *A continuum description of the buckling of a line of spheres in a transverse harmonic confining potential.* Royal Society Open Science, 10(7): Chapter 3.
- Irannezhad, A., Weaire, D., Mughal, A., Ryan-Purcell, J., and Hutzler, S. (2022). *Buckling of a tilted line of confined hard spheres.* Philosophical Magazine, 102(24): Chapter 2.
- Weaire, D., Mughal, A., Ryan-Purcell, J., and Hutzler, S. (2022). *Description of the buckling of a chain of hard spheres in terms of Jacobi functions.* Physica D: Nonlinear Phenomena, 433: Chapter 4.
- Hutzler, S., Mughal, A., Ryan-Purcell, J., Irannezhad, A., and Weaire, D. (2020). *Buckling of a linear chain of hard spheres in a harmonic confining potential: Numerical and analytical results for low and high compression.* Physical Review E, 102(2): Chapters 2, 3.

Contents

List of Figures

List of Tables

1 Introduction

Chains of particles are a fascinating area of research which spans from one-dimensional (1D), two-dimensional (2D) to three-dimensional (3D) structures. These deceptively simple structures lie at the heart of many areas in physics, and offer an insight into the behaviour of matter at a variety of length-scales.

1D chains, which are simple lines of particles like beads on a string, are particularly useful in condensed matter physics, where they can be used to investigate diverse phenomena: including the behavior of electrons in quantum wires [1] and the dynamics of magnetic spins in nanowires [2].

Into 2D, the chains take on planar structures that can manifest as colloidal crystals [3] or the rearrangement of ions in laser-cooled traps [4]. These kinds of 2D structures have been used to probe the mechanical, optical and electrical properties of materials, such as graphene [5].

Extending to 3D, we find columnar structures of particles that can be used as scaffolds for microengineering applications [6] or, at the macro scale, a system of hanging bubble chains - a structure for which one could win a world record [7]! An example of some of these structures can be seen in Figure 1.1, demonstrating their many varied applications - while also showing their similarities from nano- to macro- scale.

The structure and dimensionality of these chains plays an important role in their applications. Whether it is through tuning the optical properties of an ion trap [8] to understanding the mechanical properties of micro-robots used for drug delivery [9], there is a clear need for and interest in a deeper understanding of how structures may

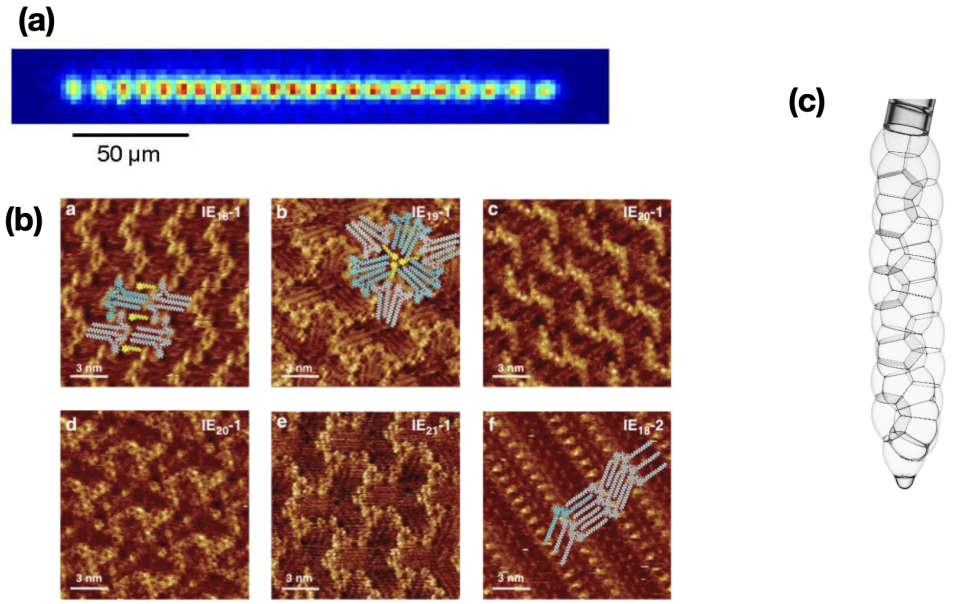

Figure 1.1: An example of chains of varying dimensionality, from nano- to macro-scale. (a) A 1D chain of 23 isotopicall pure Ytterbium ions images in an ion trap [11]. (b) Scanning Tunnelling Microscopy images of 2D chain arrangements of alkali chains, showing these chain structures on the nano-scale [12]. Also pictured are molecular models of these chains, showing clearly their zig-zag structure. (c) Image of a chain of bubbles hanging from a tube. By varying the bubble diamater relative to the nozzle diameter, the structures formed can be varied. [13]

be assembled and developed, and their relationships between each other. In this thesis we shall explore chain-like structures of varying dimensionality through the use of a simple model, closely related to work done on the columnar packings of spheres [10].

The range of experiments and systems mentioned have a large amount of variation in their methods. In some cases, the chains are formed by interactions between attractive particles [14], for others the assembly process is driven by the action of some confining potential [15]. For some systems the particles are (at least approximately) hard and resist deformation and/or compression and others are "soft", i.e. the particles themselves change shape under the action of external forces, most obviously in the systems involving bubbles.

We will now examine two examples of systems related to the work of this thesis, one at the macro-scale and one at the micro-scale. The first of these is the classical example

of a buckling beam, the Euler Elastic Buckling problem, from which we borrow much of the language of this thesis. The second example is that of Coulomb crystals, structures formed by low temperature ions in ion traps.

1.1 Buckling at various length scales

Here we will examine the idea of structures 'buckling' in a wide range of length-scales: from the macroscopic buckling of a column under load, to the deformation of a chain of atoms in a crystal. We will examine these in more detail here, to provide further context to the work done in this thesis and to introduce some of the concepts which we will make use of in later chapters.

Buckling at macro-scale: Euler buckling

Euler's Elastic Buckling Theory, established by the Swiss mathematician Leonhard Euler in the 18th century, serves as a fundamental framework for understanding the behavior of slender structural elements (beams) subjected to axial compression [16].

At its core, this theory identifies a critical compressive load (or more simply, an applied compressive force), known as the Euler buckling load ($F_{critical}$), beyond which buckling occurs (an example of a column with $F > F_{critical}$ can be seen in Figure 1.2). Buckling is a structural instability phenomenon characterized by a sudden lateral deflection or deformation of the element, usually a column or beam, under the influence of compressive forces. For the purposes of this discussion, we shall assume deformation occurs while the material remains within its elastic limit, meaning it can return to its original shape when the load is removed.

In the case of Euler buckling, the beam is an idealised construct. It is perfectly straight, homogeneous, and composed of an isotropic material. Modifications to the theory may account for realistic materials, but such considerations are beyond the scope of what is required for this thesis. We will also limit our discussion here to the case of a 'simply supported beam' (a structure whose ends are supported, but free to rotate) under

Figure 1.2: A disturbing sight at a construction site! The critical load on this steel-reinforced concrete column has been exceeded, and caused the column to buckle (the lateral displacement of the steel frame). This is unlikely to be elastic buckling, i.e. the steel will not return to its original shape when the weight is removed, but it does show the expected profile of a buckling beam. Image taken from `https://www.pinterest.com/CivilEngDis/`.

longitudinal compression, see Figure 1.3. This model Euler buckling demonstrates many of the properties that we will explore in our model system in later chapters.

This idealised problem was in fact proposed by Jacob Bernoulli, and later solved by Euler [17] . It demonstrates many interesting properties, including a linear and non-linear bifurcation, and it describes completely the pre- and post- critical behaviours of the beam.

As shown in Figure 1.3, we will consider an inextensible rod of length L that is simply supported between two supports a distance d apart. We characterise the profile of the beam by the angle of inclination of a line tangential to the beam, θ. In the case of separation between the supports $d > 0$, it can be shown that this angle of inclination as a function of position along the beam s is described by:

$$\frac{d^2\theta}{ds^2} = -\frac{F}{B}\sin\theta, \tag{1.1}$$

where s is the distance along the beam, F is the axial compression force and B is the 'bending stiffness', a measure of the beam's resistance to buckling when subjected to an external load (it is the product of the Young's modulus of the material times the

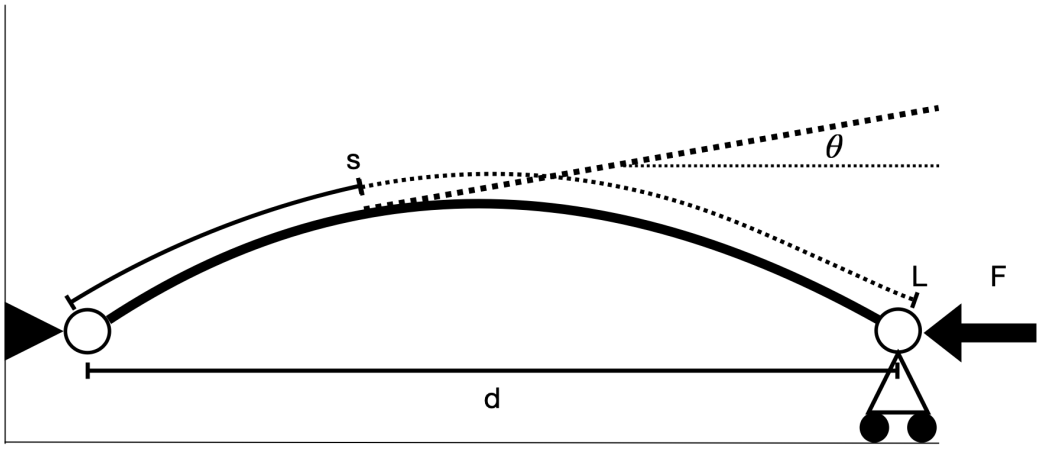

Figure 1.3: A schematic of the Euler buckling problem discussed in this section. We consider a slender, incompressible beam of length L, held by supports which allow for the rotation of the beam at the supports. The right support is free to move, and the distance between the supports is d. We characterise the deflection of the beam, under an applied compressive load F, by the angle of inclination of the tangent line θ at the point s. This function, $\theta(s)$ is a solution to Eqn (1.1).

area moment of inertia of the beam). Immediately, we may draw a comparison between this equation and that governing the oscillation of a simple pendulum [18].

We may consider a linearised version of this equation for small deflections, expanding around $\theta = 0$. This results in a linear eigenvalue problem which, for our choice of boundary conditions, produces a sinusoidal solution [19]. Although the amplitude of this solution is undetermined as a consequence of the linearisation, an infinite number of solutions are found:

$$\theta(s) = A_n \cos \frac{n\pi s}{L}, \tag{1.2}$$

where $n = 1, 2, 3...$, as well as the trivial solution $\theta = 0$. The non-trivial solutions are the 'bifurcation modes' of the Euler beam. We show the first two non-trivial modes in Figure 1.4.

It is possible to determine the amplitudes of these solutions, as well as verify the

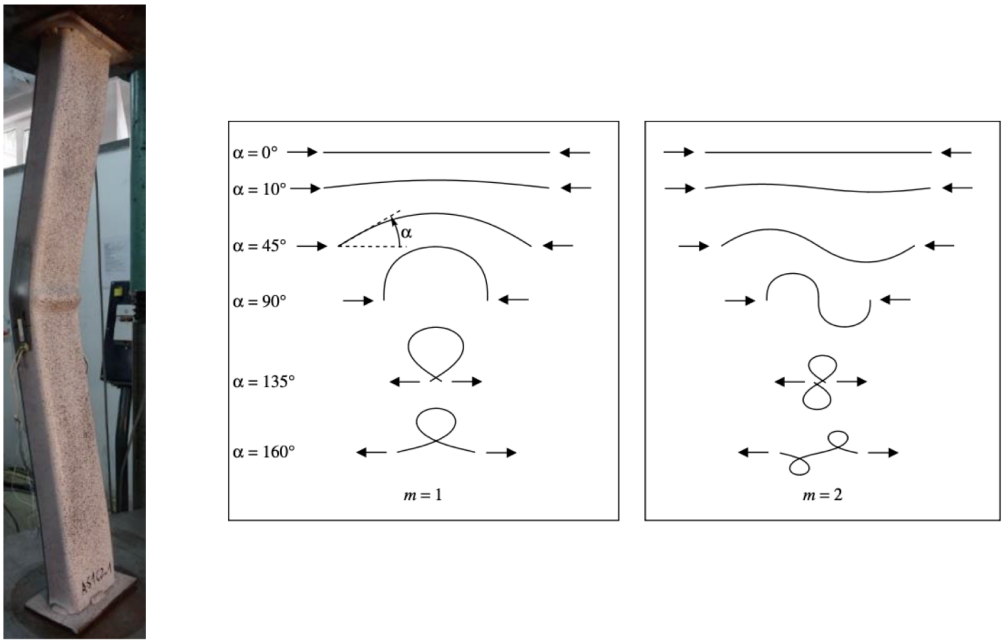

Figure 1.4: Examples are shown here of the first two modes of Euler buckling of the system shown in Figure 1.3 (reproduced from [20]), the first two solutions of Eqn (1.1). The variety of structures are characterised by the initial angle $\theta(0) = \alpha$. Note that the distance betweeen the supported ends, d, is a function of this angle. A physical example of the first mode can be seen on the left, showing the buckling of a concrete-filled steel tube under compression (image reproduced from [21]).

validity of the linearised method, by solving the original non-linear equation. We will not do so here, but we will briefly note the appearance of the Jacobi elliptic functions in the full solutions [20], analogously to the solutions of the nonlinear pendulum problem [18]. We will also encounter Jacobi elliptic in our discussions of our model system, and we will discuss them and their implications in detail in Chapter 4.

Euler's elastic buckling theory provides a foundational understanding of structural instability, guiding engineers in designing columns, beams, and other slender elements to resist buckling under compressive loads. While it simplifies complex phenomena, it remains a cornerstone in structural analysis [19] , forming the basis for more advanced buckling theories [22] and practical design guidelines [23].

Micro-scale buckling: Coulomb crystals

Physical ion traps are complex devices used in quantum computing, quantum information processing, and precision spectroscopy. They function by employing

electromagnetic fields to confine and manipulate ions in a controlled manner. These ion traps come in various forms, the main two of which are the *Paul trap* and *Penning trap*. We will focus on the linear Paul trap here, as it is the usual method of forming Coulomb crystals.

A charged particle experiences a force within an electric field. Earnshaw's theorem [24] states that a static electric field is not sufficient to completely confine a charged particle. The Paul trap circumvents this by employing a static electric field in conjunction with an oscillating electric field. The Penning trap uses a magnetic field for a similar effect.

The linear Paul trap [25] uses an oscillating quadrupole field to trap charged particles in the radial direction. A static electric field confines the particles in the axial direction (also referred to as a stopping potential). A schematic of a linear Paul trap is shown in Figure 1.5.

A Coulomb crystal of ions may be formed within a linear Paul trap if the system is sufficiently cool, approximately $T \approx 10\text{mK}$ (the Coulomb crystallisation temperatures). Thus formation of these structures was only feasible after the rise in prominence of laser cooling in the 1980s.

Although Coulumb crystals usually form in the Body Centred Cubic (BCC) structure, as is theorised in the collapse of neutron stars in astrophysics [26], the structure depends strongly on the nature of the confinement and the density of ions within the trap. It has been shown, and observed experimentally as shown in Figure 1.6, that for sufficiently low number of ions within the trap, the ions form a linear arrangement along the axis of the trap.

If the number of ions within the trap is increased, or if the strength of the oscillating quadrupole potential is decreased, the ions move into a 2D structure: a zig-zag like pattern. Furthermore, when the number of ions is increased further, the structure moves into a 3D structure, a helical pattern. A theoretical prediction of these transition points was produced by Totsuji, H., and Barrat, J.-L. in 1988 [27], and was

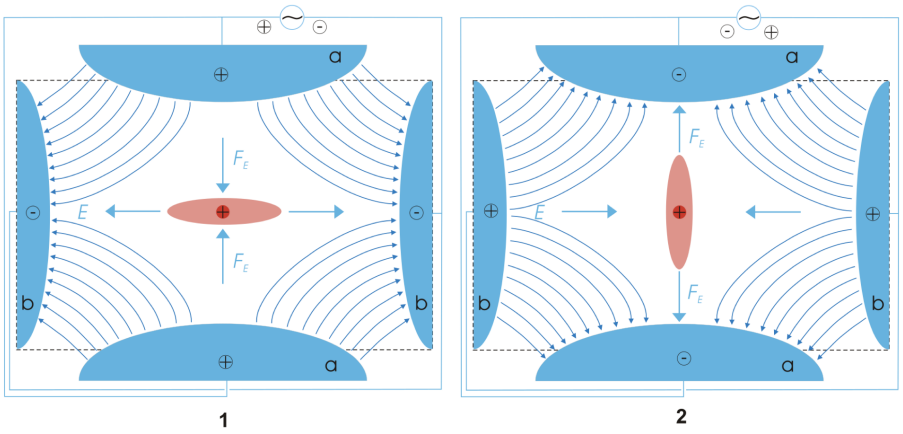

(a)

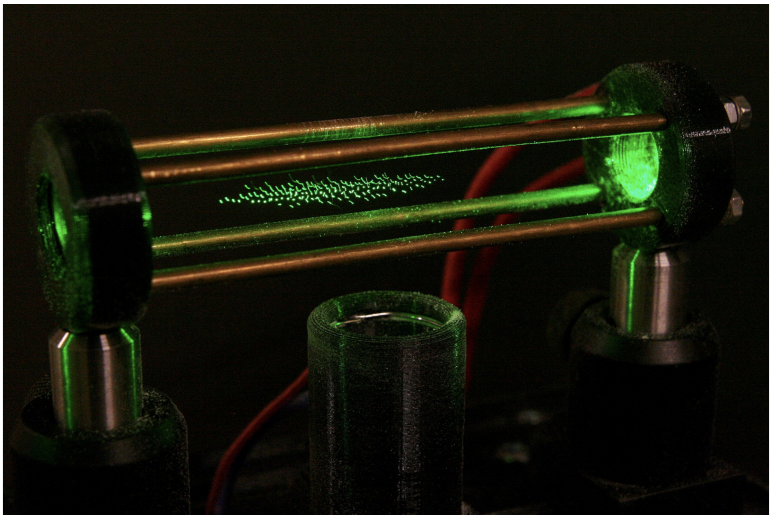

(b)

Figure 1.5: (a) shows a diagram of the two maximal states of the linear Paul trap, looking down the axis of symmetry of the system. The quadropole fields are caused by AC, and thus vary throughout cycles. The symmetry confines the ions in the radial direction. Not pictured are the two electrodes providing the stopping potential in the axial direction, these are usually static fields. (b) shows a macroscopic example of the linear Paul trap, with charged grains of flour suspended in the trap well. Both images were sourced from `https://en.wikipedia.org/wiki/Quadrupole_ion_trap`.

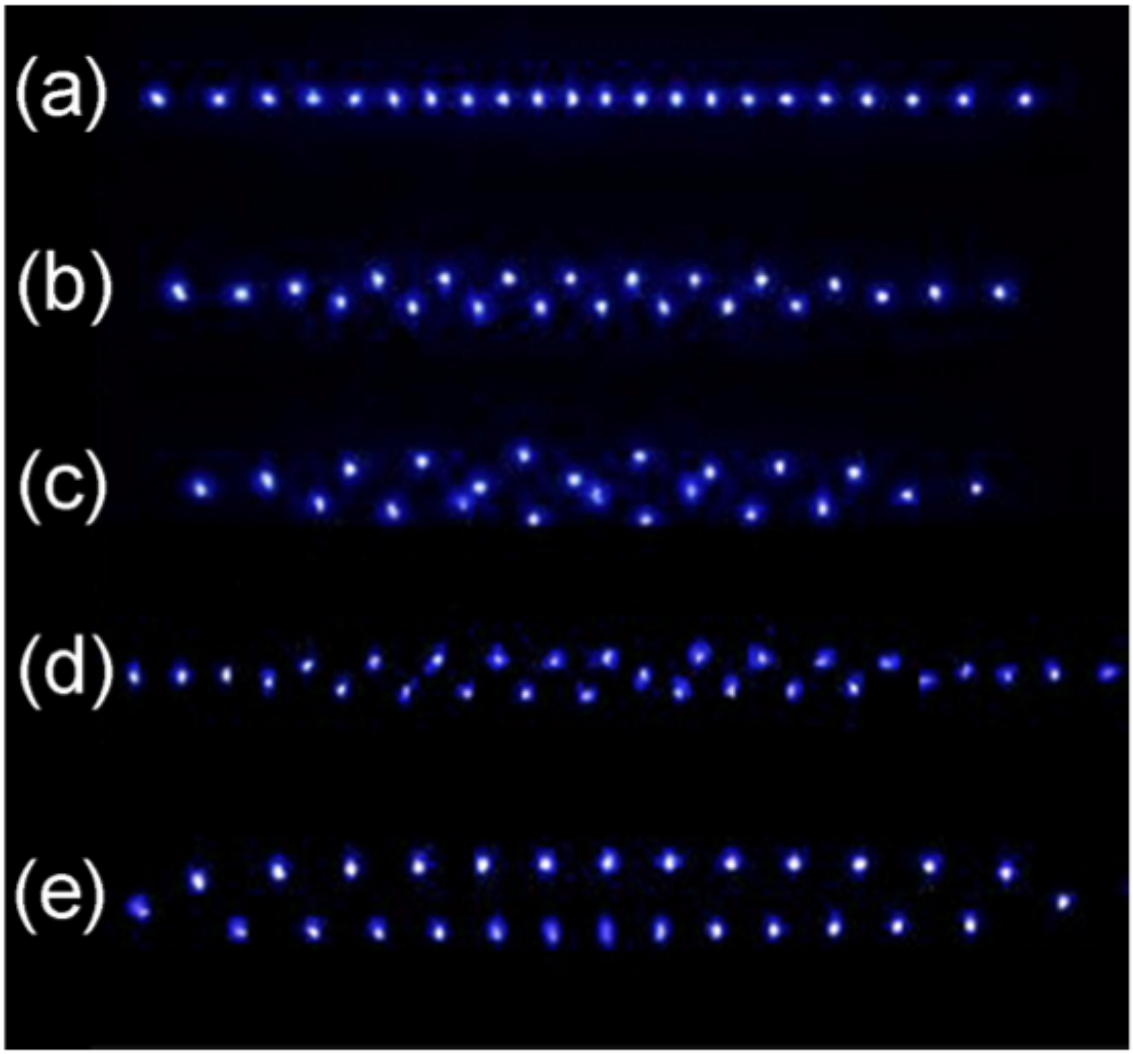

Figure 1.6: An image of 22 ytterbium ions held on the axis of a linear Paul trap, reproduced from [4]. By relaxing the radial potential, the structure moves into a zig-zag shape. We will observe similar structural transitions in our model systems in later sections.

explored experimentally in the 1990s [28, 29]. An example of the arrangements of ytterbium ions found by RC Thompson [4] are shown in Figure 1.6.

Aside from their natural occurrence in stellar collapse [26], Coulomb crystals also have applications in quantum information processing and spectroscopy [30].

1.2 A model system for a buckled line of spheres

It is an attractive idea to unite these concepts of a line of particles deforming under compression and buckling with a simple model. Can we ascribe the language of

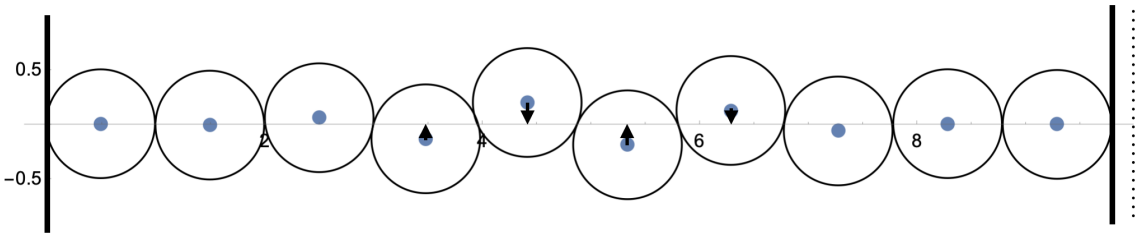

Figure 1.7: A diagram of the cross-section of 10 hard spheres of unit diameter under compression by two hard walls, and held in confinement by a harmonic potential. The x-axis represents the line of symmetry of the confining potential, and the restoring forces experienced by the spheres are indicated by black arrows. The dashed black line represents the 'natural length' of the system, and the thick black walls represent the boundary walls. Already some of the interesting properties of the system are on display, which shall be explored later: the strcture immediately buckles under slight compression due to the hardness of the spheres, the displacement of the spheres are around the midpoint of the system, and the buckling is localised (the system has fewer spheres with larger displacements). The displacements for this representative diagram were made using the continuum model for buckling profiles, which we shall discuss in Chapter 3.

buckling to structures such as Coulomb crystals? Where a beam experiences a lateral deflection due to its load, a line of ions displace themselves through a confining potential field as a result of compression. Here we endeavour to do so. Such simple models are an attractive prospect in physics, both for research and teaching purposes. The model we propose here has found success in both [31, 32].

We consider a line of N spheres, monodisperse and without attractive inter-particle forces. This line of spheres is held in a transverse, cylindrically symmetric, harmonic confining potential. Perpendicular to the axis of symmetry, at either end of the line, are two movable hard walls which may set the system length. The spheres may be hard or soft. See Figure 1.7 for a schematic diagram of the model.

For the purposes of this thesis, we will limit ourselves to static, *monodisperse* (all spheres in the system will be of equal size) arrangements of spheres with no attractive forces acting between them.

We will investigate the behaviour of the lines of spheres under compression, i.e. by varying the distance between the boundary walls, such that the length is shorter than the natural length of the straight line of spheres. In accordance with the experimental

methods which we will discuss later, we will focus on systems that are displacement controlled, meaning that the compression is driven by the movement of the boundary walls. We define this compression as:

$$\Delta = (L_0 - L)/D, \tag{1.3}$$

where $L_0 = ND$, the number of spheres in the system times their diameter: the natural, uncompressed length of the system. L is the distance between the boundary walls. We will use this quantity to characterise both experimental and theoretical structures.

Even at this early stage, the system demonstrates interesting details which are a challenge to theory. If the two boundary walls are brought closer together the results will initially differ depending on the hardness/softness of the spheres. For hard spheres, the chain will immediately move into a 2D planar structure by the virtue of the geometrical constraints. For soft spheres, there will be a region of compression where the 1D chain will be stable, until some critical value of compression where it too will move into a 2D structure.

We refer to this process of movement between the 1D and 2D phase as 'buckling'. These buckled chains may be characterised by their displacement profiles which plots the displacement of each sphere centre away from the central axis. An analysis of the sphere displacement profiles and the various 2D structures which may exist under compression will be explored in Chapter 2. These plots of the magnitude of sphere displacements bring to mind the similar profiles of the buckling Euler beam.

There exists another critical point of compression (which again varies depending on whether the spheres are hard or soft) at which point the buckled structure moves from a planar structure to a 3D structure. The 3D structures formed this way are very similar to those found for the packings of hard and soft spheres within cylindrical confinement [10, 32, 33].

One of the attractive aspects of this model is how amenable it is to experiment. We

(a)

(b)

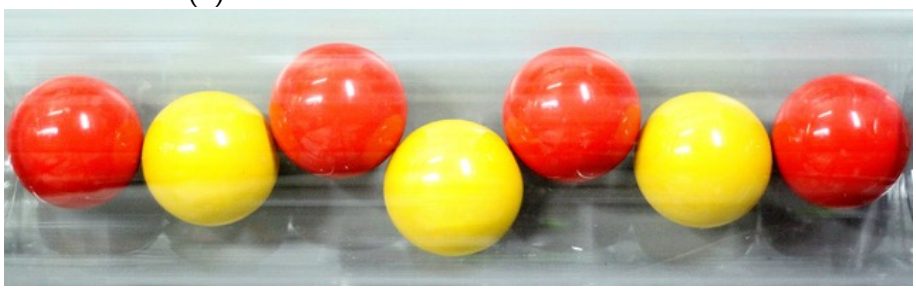

Figure 1.8: The experiment in (a) shows a simple method to explore the buckling of a line of spheres under compression. Here a line of billiard balls lie on the curved interior surface of a perspex tube. If this line of balls is compressed by applying a force at either end, the linear arrangement becomes unstable and buckles. The curvature of the surface acts as the confining potential, resulting in the 'zig-zag' arrangement we observe in (b). Image credited to Ali Irannezhad.

will now explore how the full range of structures from the 1D chain to the 3D columnar structures may be studied in experiment.

1.3 Experiment: Approximating the harmonic potential using a cylindrical surface

For the investigation of the 1D and 2D structures, a simple experimental set-up was proposed in [34]. This work was expanded upon in [35], and it is this implementation of the experiment which we shall discuss here.

For investigating the case of hard spheres, lubricated ball bearings are placed on the

Figure 1.9: Ali Irannezhad and the experimental apparatus he had comissioned to study the buckling of a line of spheres under compression and tilt. This image was featured in an article titled 'Physics in a Small Bedroom', highlighting experiments that were rich in detail and yet could be carried out outside the lab (Image reproduced from [31]).

interior curved surface of a cylindrical tube. For soft spheres, the system may be filled with water and bubbles inserted. These bubbles will then be held under the curved surface of the tube by buoyancy.

In both cases, provided that the diameter of the ball bearings/bubbles is much smaller than that of the cylindrical tube, the structures will be approximately planar. The weight of the hard sphere and the buoyancy of the bubbles moving against the curved surface of the tube gives rise to a restoring potential which is approximately quadratic (see Appendix A2 for more details on exactly how the quadratic potential may be related to the experimental parameters).

The cylindrical tube may be plugged by pistons, which play the role of our movable hard walls. This means that the compression of the system is an adjustable parameter, defined as in Eqn (1.3). One effect of this experimental set-up is that the bubbles are slightly deformed by their contact with the surface of the cylinder. We shall explore this in more detail in Chapter 5. A sequence of photographs showing the buckling of a

line of hard spheres under compression is shown in Figure 1.9. A sequence of images for bubbles under increasing compression is shown in Figure 1.10.

This experiment presents a clear image for the expected evolution of a line of spheres under compression. Under infinitesimal compression, systems with hard spheres will buckle immediately forming 2D planar structures. For soft spheres, the particles will instead deform under compression remaining in their 1D chain structure. At some critical value of compression they will then buckle.

Under low compressions, for both hard and soft spheres, these experiments display a symmetrical, localised buckling where spheres close to the midpoint of the system are displaced more than spheres near the boundaries. These symmetric structures arise as a consequence of the symmetry of the system, and we will discuss how this symmetry may be broken later. For increased compression, this buckled structure evolves into another kind of 2D structure, which can be seen in Figures 1.10 and 1.11, Image 10, an arrangement where most of the chain is in a linear arrangement, but two spheres have formed next-nearest neighbour contacts - an arrangement which we refer to as the 'doublet'. This point will be important in our theoretical description of these structures in Chapters 2 and 3.

Structures formed at compressions beyond the doublet were not discussed in [34] or [35], as the doublet was considered the limit of this experimental method. Due to the use of a curved surface as a confining potential, the structures found in this experiment must remain planar, and the prediction of the time was that beyond the doublet there was no guarantee that further buckling would remain planar; in principle any further buckling could occur out of plane with the doublet that had formed.

However, in simulation work done on this subject [36] and indeed according to results presented in this thesis, it is found that the structures *do* remain 2-dimensional after the formation of the doublet. In fact, the doublet forms part of an emerging structure which we refer to as "the zipper". This is the true termination point of this experimental method, relative to our model. In order to move past this point, we must

consider an experimental system with true cylindrical symmetry. We shall discuss such a system in the next section. Examples of the linear, buckled, doublet and zipper structures are shown in Figure 1.11.

1.4 Experiment: Chains of spheres in a rotating fluid

An experimental method which allows for the investigation into the evolution of 3D structures was proposed by Lee *et al.* [37]. In this system, spheres are contained in a cylindrical tube with hard walls, and immersed in a fluid of greater density. In their experiments this tube is attached to a lathe, capable of rotating the tube at high speeds. The less dense spheres are driven towards the central axis by centripetal force (in the experiment done by Lee *et al*, these were mainly hard spheres: polymeric beads). For a constant rotational speed, the centripetal force behaves similarly to the harmonic confining potential in our model system. A schematic of this system is shown in Figure 1.12.

Unlike the experiment described in the previous section, the tube in this experiment is of fixed length. The method of obtaining different structures was then to increase the number density of spheres within the tube, or by varying the rotational speed. Examples of the structures that can be found using this method can be seen in Figure 1.13.

The evolution of the structures under increasing number density (or equivalently compression) matches closely with simulation results obtained in [32, 38], where a complete description of the 3D structures obtained from this method was presented.

We note that in experimental work, even with systems that are level, asymmetric structures may form instead of the expected symmetric structures. We assume that these are higher energy structures, and that by perturbing the system (as done in [35])

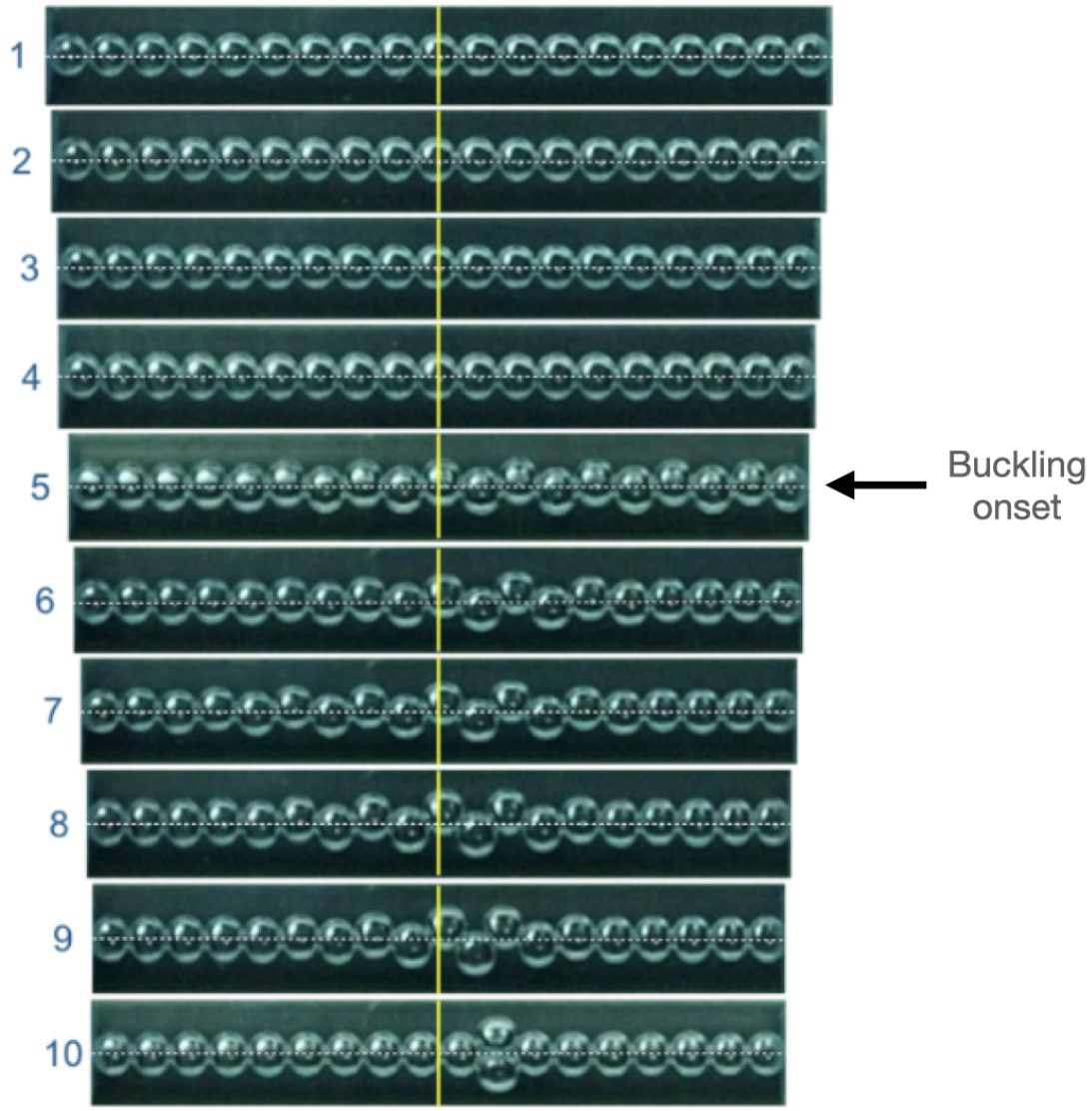

Figure 1.10: A sequence of images displaying a line of bubbles (19 bubbles, $D = 2.3mm$, inner tube diameter $D = 6.7mm$) under compressions $\Delta_i = 0.13, 0.32, 1.00, 1.56, 2.13, 2.36, 2.56, 2.62, 2.80, 2.85$ [35]. The images were taken sequentially, with compression being increased a small amount between images. Immediately obvious is the difference between these images and the hard sphere results: the bubbles do not immediately buckle, remaining in a '1D' structure until a critical value of compression is reached. We will explore theoretical models of this critical value of compression in Chapter 6.

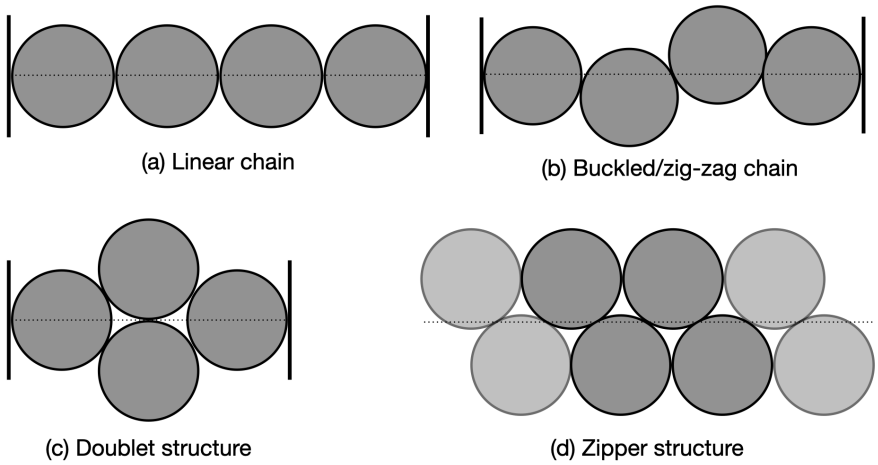

Figure 1.11: A line of hard spheres contained within a transverse harmonic confining potential displays a range of structures under compression. These structures, and the terms used to describe them, are shown here. Compression is increasing from (a) through (d). If the system is between hard walls, as shown here, the structure will first buckle locally as in (b). Eventually this becomes the 'doublet' structure, where one pair of spheres make next-nearest neighbour contacts. For longer chains this becomes the zipper structure, a structure where each sphere has formed a next-nearest neighbour contact. Beyond this point, if compression is increased again, the structure will 'twist' into a 3D structure.

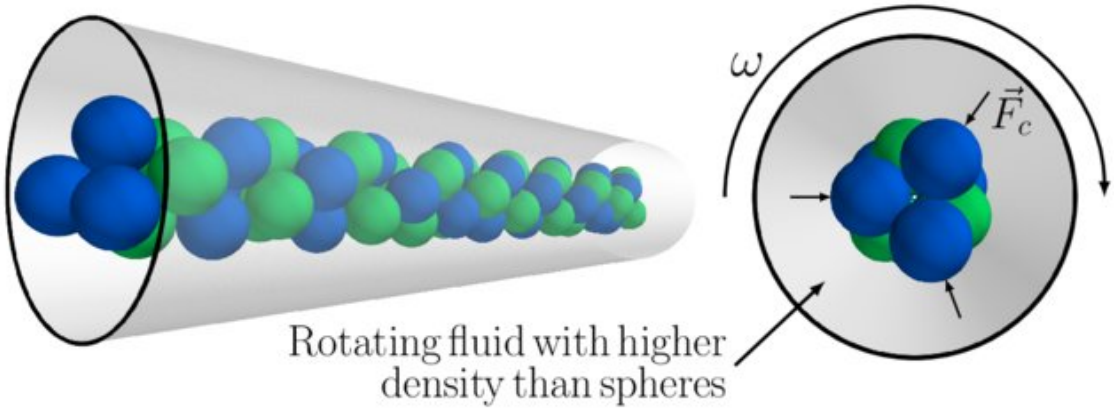

Figure 1.12: A schematic of the rotational method of assembling columnar structures of spheres explored in [32, 37] (Figure reproduced from [38]). A tube of rotating fluid containing relatively less dense spheres forms columnar structures of spheres along the axis of rotation. Varying the rotation speed varies the strength of the confining potential. This experiment generates a cylindrically symmetric confining potential, allowing for the observation of 3D columnar structures.

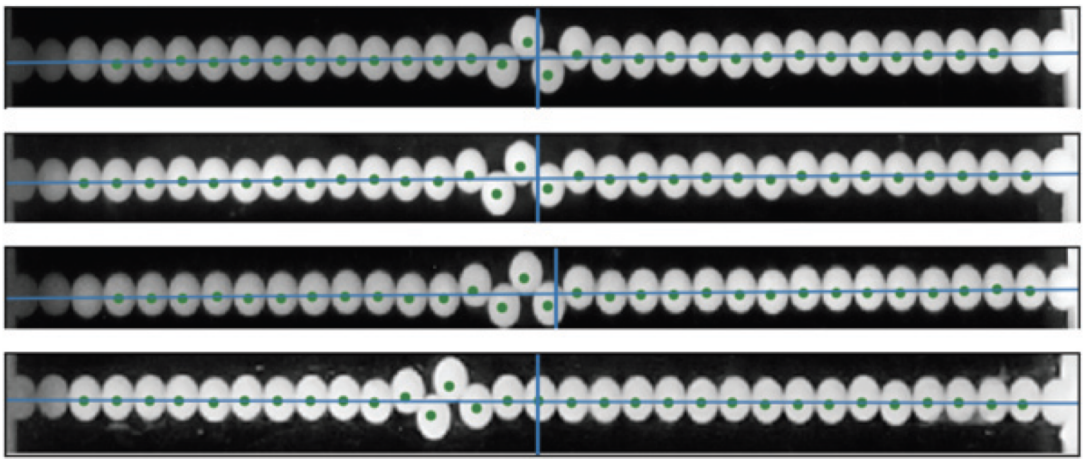

Figure 1.13: Examples of the planar buckled chain of spheres found using the rotational method (image reproduced from [32]). Here polypropylene beads are held in a tube rotating at 1800 rpm. The structures match those found by the previous experimental method, and the results of simulations which we will discuss in later chapters.

that the structures can be coaxed into their symmetric arrangement.

1.5 Manipulating buckling: Adding a longitudinal force

We can draw parallels between the buckling of a line of spheres and the study of crystalline defects [39]. The localised, buckled structure resembles topological defects found in Coulomb crystals [40]. It is then of interest to ask - can this 'defect' be manipulated? Is it possible to control the position of where these buckling defects occur?

In an effort to answer this question, we will add a new parameter to our simple model - a longitudinal force which acts on sphere centres, parallel to the axis of symmetry of the confining potential. The addition of this force breaks the symmetry of the problem; the longitudinal force results in a displacement of the peak position of the sphere displacements.

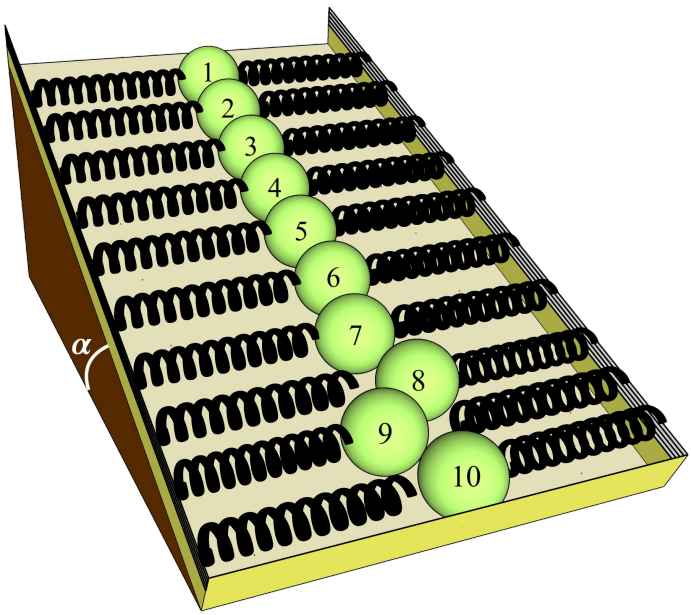

Figure 1.14: A conceptual illustration of the experimental method used to investigate the buckling of a chain of hard spheres under the action of tilt. A tilt by an angle α beyond a critical value leads to a buckling of the initially linear chain; transverse sphere displacement results in a harmonic restoring force, represented here by springs.

This force may be realised experimentally by both the methods proposed by Irannezhad *et al.* [41] and Lee *et al.* [37]. In these cases, the force is introduced by inclining the axis of symmetry of the tube relative to the horizontal. In this case, the component of the spheres' weight acting parallel to the central axis of the potential provides the symmetry breaking longitudinal force. For this reason, we shall refer to this longitudinal force as a "tilt force", or more simply, "tilt": τ.

Figure 1.14 shows the effect of this on our line of spheres. Here we represent the confining harmonic potential with springs. Each sphere now experiences a compressive force due to the component of the weights of the sphere above it. This may result in a buckled structure emerging, even without a compressive force exerted by a second wall, as shown in this figure. We will discuss both the cases of structures formed by tilt alone and the combination of tilt and compression in Chapter 3.

We may ask the question: what happens to a line of spheres held between hard walls in a transverse harmonic potential as tilt is increased? Unlike the case of compression, initially the hard sphere linear arrangement does not become unstable under the action of tilt. Only once a critical value of tilt is reached does the structure begin to buckle.

These buckled structures are no longer symmetric, and instead localise at a point closer to the lower wall of the system.

The displacement of this buckling peak can be considered similarly to the transport of a defect in a crystalline lattice, and the energies involved in this movement may be used to calculate the Peierls-Nabarro potential [42].

In the next chapter we will discuss this effect of buckling under tilt in more detail, explaining how the original theoretical models for untilted systems were generalised to account for the presence of the tilt force. We will discuss the concept of a "critical value of tilt" at which structures undergo sudden transformations. In later chapters we will also discuss structures which are both tilted and compressed.

1.6 Thesis overview

It is clear that even this simple model of a line of spheres compressed by two hard walls and confined by a transverse harmonic potential, provides a rich amount of detail to explore. It is, however, important to keep clear the subtle differences between the ideal model and the variations explored in the theoretical and experimental work. As such, a brief overview of the contents of the thesis will be provided here, as well as a "map" of the topics to be explored and the relationships between them, Figure 1.15. We hope this will be an aid to reading the thesis, and allow one to jump between chapters and sections without too much confusion.

In the first part of this thesis, we will specifically discuss systems of hard spheres under tilt and compression. In particular we will focus on systems with a low degree of buckling. We will discuss a difference relation, originally proposed in [43], which provides a method of computing structures under compression. We will extend this description to systems of spheres under tilt, as well as further the analysis on the critical value of tilt τ_c at which the linear chain of spheres becomes unstable.

On the basis of this difference relation, we shall develop a continuous theory which

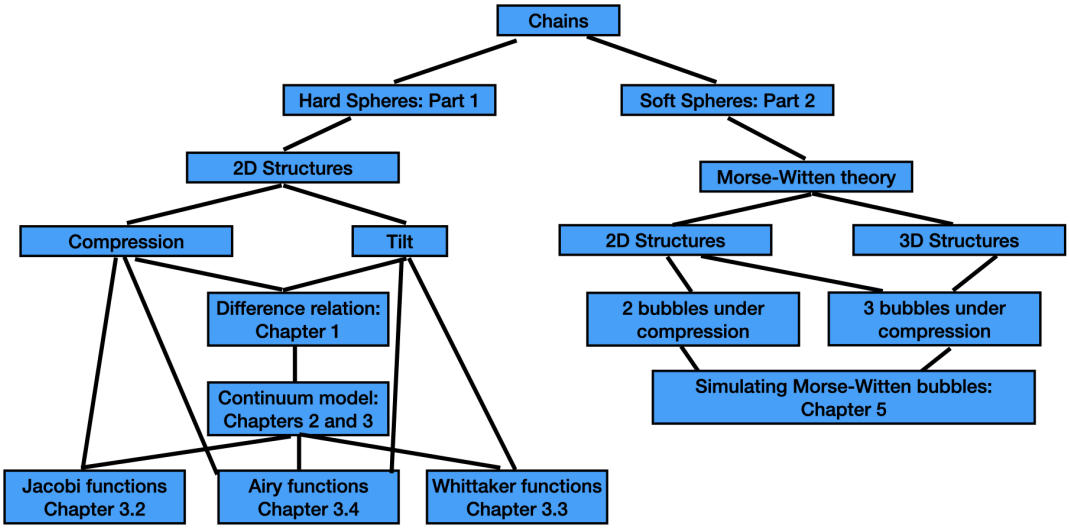

Figure 1.15: A map of the topics discussed in this thesis and their relationships to each other. Chapter/Section references are indicated for most of the topics, and the directional arrows should give some idea of the logical progression, a chronological map would have been much more complicated!

describes buckled profiles as solutions to a second order differential equation. We shall present numerical results, and discuss limits where analytical results may be obtained. This work will dive deeper into the concepts of localisation of buckling under compression, the critical value of tilt, and discuss systems subjected to both compression and tilt simultaneously.

In the second part of this thesis we will focus on chains of soft, elastic spheres, particularly bubbles. We will discuss various methods of simulating bubbles, returning to the Soft Sphere model and introducing the Surface Evolver. We will implement Morse-Witten theory [44] in a 3D system, and use it to model a chain of soft spheres under compression. These bubbles chains will serve as an excellent test-case for the Morse-Witten theory in 3D, which has only so far been applied to systems with high degrees of symmetry [45], or bubbles with only a single contact [46]. We will finally close the thesis with an outlook section.

Part I

Hard Spheres

2 Lines of hard spheres under compression and tilt

In this chapter we will discuss our model system in more explicit detail. We shall start with the case of a line of hard spheres held in the transverse harmonic potential, under compression between two hard walls. We will then extend this description to include the action of a longitudinal force acting on the spheres in the line: tilt. An example of an untilted profile as seen in experiment is shown in Figure 2.2 and a tilted profile in Figure 2.4.

2.1 Model and method

We are concerned with a system of N hard spheres of diameter D, confined between hard walls. The spheres are contained within a cylindrically symmetric harmonic potential, such that a displacement Y in this potential results in a restoring force kY, where k is a spring constant. From this point onwards we shall proceed with a dimensionless description of the system: we shall express lengths in terms of the sphere diameter $x = X/D$ and forces in terms of the restoring force of the confining potential $f = F/(kD)$ (we shall adopt lowercase lettering for dimensionless quantities).

The dimensionless compression is therefore given by the equation:

$$\Delta = N - l, \tag{2.1}$$

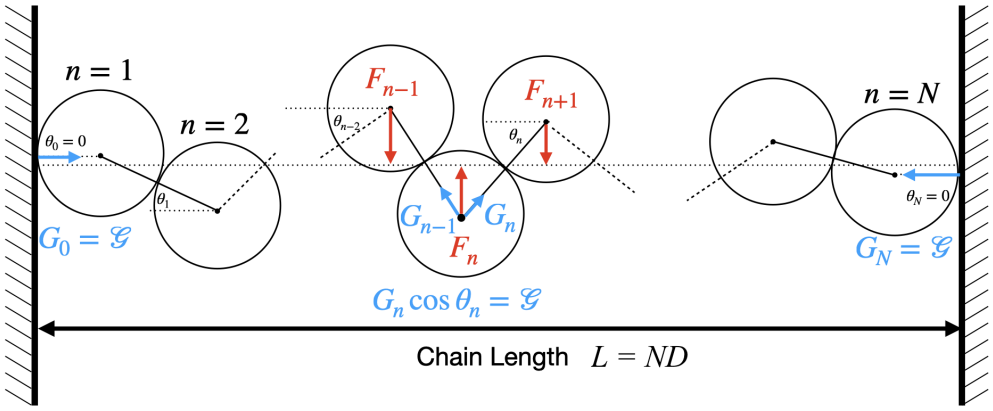

Figure 2.1: A schematic diagram of the untilted system showing the quantities of interest. The axis of symmetry of the confining potential is shown as a dotted line. Displacements of the spheres from the central axis, y_n, are subject to a restoring force F_n. The compressive force exerted at sphere contacts is given by G_n, with the condition of mechanical equilibrium giving $G_n \cos\theta_n = \mathcal{G}$, the compressive force exerted by the wall on the system.

where N is the number of spheres (equivalent to the natural length of the chain in our dimensionless notation) and l is the dimensionless compressed length of the chain, L/D. The dimensionless energy can be obtained by summing the square of the sphere displacements:

$$E = \frac{1}{2}\sum_{n=1}^{N} y_n^2. \tag{2.2}$$

In [43] an iterative stepwise method was proposed which describes arrangements of spheres in the 'zig-zag' structure (we expanded upon this method in [34]). We will describe the method here, as it forms the basis of the continuum model which we will explore in the next chapter.

Referring to Figure 2.1, we wish to calculate the dimensionless displacements from the central axis y_n and the angle of lines between sphere centres θ_n. We use the nature of the 'zigzag' arrangement to consider only the positive values of these quantities, i.e. the direction of measurement of displacement and angle alternates from one sphere to

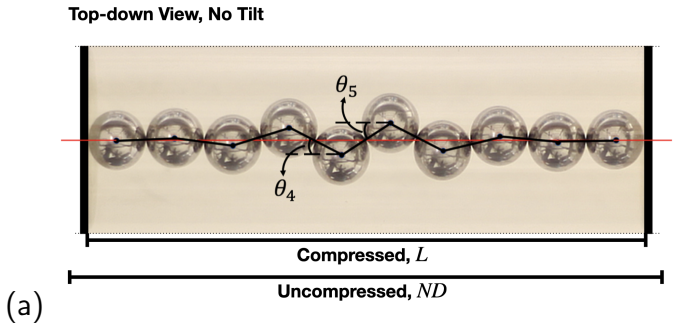

(a)

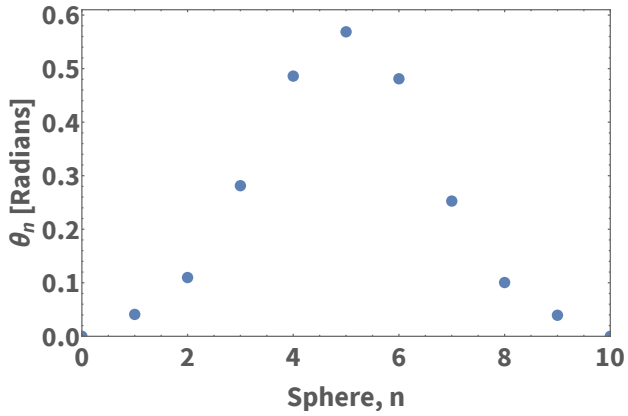

(b)

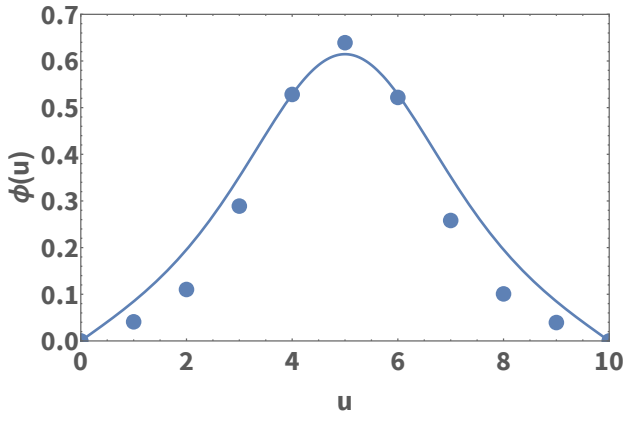

(c)

Figure 2.2: (a) Photograph of a buckled line of $N = 10$ metal spheres (ball bearings) resting in a horizontal cylinder, between two stoppers. In such an experiment, the curvature of the cylinder provides an approximately harmonic potential, that is, a restoring force acting on transversely displaced spheres [35,41]. The angles θ_n between contacting spheres and the cylinder axis vary along the line. (Inner cylinder diameter 21.05 mm, sphere diameter $D = 6.44$mm, line length $L = 61.6mm$, corresponding to a compression $\Delta = (ND - L)/D = 0.47$ (see also Eqn (2.7)). Figure (b) shows the corresponding plot of the angle profile θ_n. The continuum theory described in this paper yields a continuous profile for $\phi(u) = \tan\theta(u)$). This is shown by the continuous line in (c), together with the experimental data from (b).

the next. In the scope of this investigation, this is sufficient to describe all structures that are found. We will now consider the condition of mechanical equilibrium, and the geometrical constraints of the system of hard spheres, in order to produce a set of iterative equations.

We express the compressive force acting between sphere $n-1$ and n as G_n. Considering the condition of mechanical equilibrium, it follows that $G_n \cos\theta_n = \mathcal{G}$, the force exerted by the system on the walls (see Appendix A1).

If we consider the equilibrium of forces acting on sphere n, perpendicular to the axis of symmetry of the potential, we find that:

$$f_n = G_n \sin\theta_n + G_{n+1} \sin\theta_{n+1} = \mathcal{G}(\tan\theta_n + \tan\theta_{n+1}). \tag{2.3}$$

As the system consists of hard spheres, the centres must be separated by a sphere diameter. Therefore:

$$y_n + y_{n+1} = \sin\theta_{n+1}. \tag{2.4}$$

However, remembering our choice of dimensionless quantities relates the restoring force due to the potential to the displacement through that potential as $y_n = f_n$, we may use the previous expressions to relate $(\theta_n, y_n) \to (\theta_{n+1}, y_{n+1})$. Thus we arrive at the following iterative equations:

$$\theta_{n+1} = \arctan\left(\frac{y_n}{\mathcal{G}} - \tan\theta_n\right), \tag{2.5}$$

$$y_{n+1} = \sin(\theta_{n+1}) - y_n. \tag{2.6}$$

In [34, 43], these original difference relations were solved using a shooting method. This shooting method is done by noting that the hard wall boundary conditions demand that $\theta_0 = \theta_N = 0$, and that the initial displacement y_1 may be arbitrary. With

the left-hand boundary set, we may use Eqs (2.5), (2.6) to search for values of y_1 such that the right-hand boundary condition is satisfied. This is done by coarse-graining the initial search of y_1 over a range $0 < y_1 \leq 0.5$ in steps of 10^{-4}. These intervals are then searched for solutions using the bisection method.

We note that in many experiments, such as those discussed in the previous chapter, compression is not a control parameter. Instead, equilibrium structures are found for varying values of $\mathcal{G}$ and compression is calculated afterwards by evaluating:

$$\Delta = N - \sum_{n=1}^{N} \cos\theta_n. \tag{2.7}$$

Note the limits of summation of Equation 2.7. The angles associated with the contacts at the hard wall contribute only half a sphere diameter to the total length of the chain (see Figure 2.1), thus we discount the initial angle θ_0 from the sum to prevent the overestimation of compression (its contribution is included in the $n = N$ term).

This method finds solutions in mechanical equilibrium, but it does not make any comment on their stability. Thus the results are combined with the soft-sphere energy minimisation simulations described in Section 5.2 in order to establish whether the calculated structures are stable or unstable.

2.1.1 Results of the iterative method

At low compression, the equilibrium structures found are symmetric between the two walls. The basic symmetry of the system means that this must be the case, and that asymmetric structures occur as equivalent pairs, related by reflection through the midpoint of the system. Such asymmetric structures emerge at higher compressions. For low values of compression the only solution found is symmetric, with buckling localised around the midpoint of the chain.

A sample of equilibrium structures found is shown in Figure 2.3 for $N = 7, 8$. There is no difficulty in applying this method to systems of higher N, but these values are

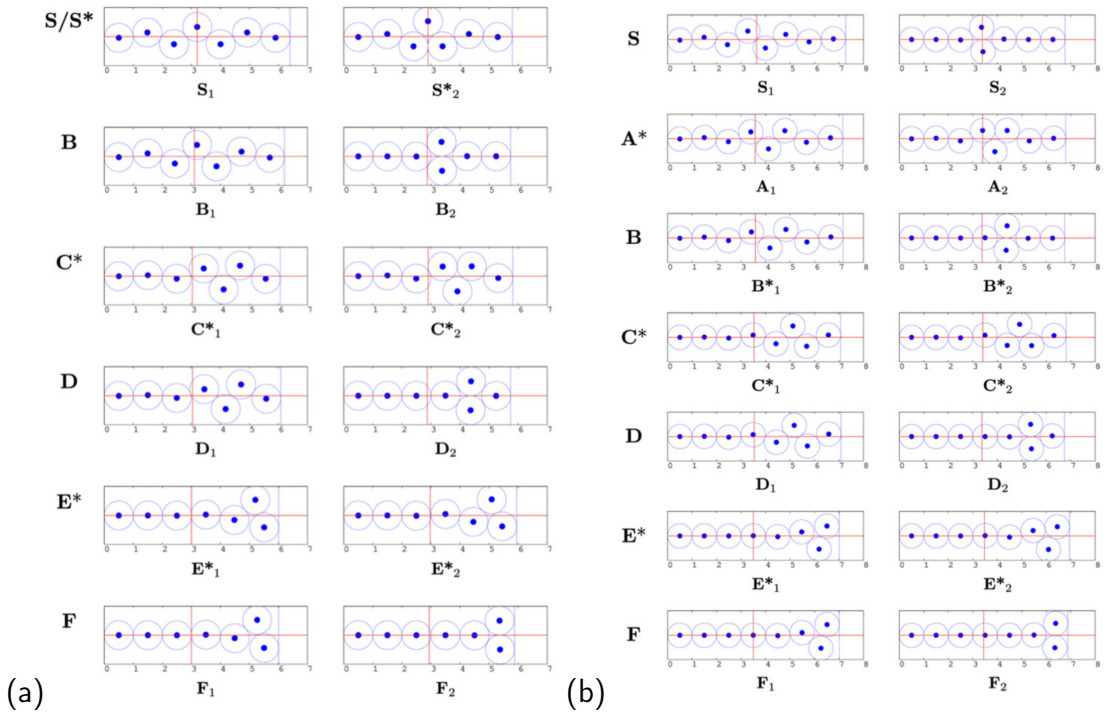

Figure 2.3: Examples of the structures found from the iterative equations using the shooting method, generated by Adil Mughal, for (a) $N = 7$ and (b) $N = 8$. The labelling of these structures is discussed in [34], for our purposes we just note that the structures are named alphabetically in order of increasing displacement of the localised buckling from the midpoint. The stability of the structures is calculated using the soft sphere simulations (see Section 5.2), and here we label unstable structures with an asterisk. Note the difference in stability of the symmetric structure S for odd and even N. Each of the asymmetric structures also forms part of a pair, with an equivalent structure formed by reflection through the midpoint (represented in these diagrams by the vertical red line).

sufficient to demonstrate the localisation properties. We also show the stability of these structures, derived from the soft-sphere simulations. We note that there is a distinct difference between odd and even value of N regarding the stability of symmetric states.

We note that the termination point of this method is the doublet structure (Figure 1.11), where one sphere forms an additional contact. This doublet may be constructed at any point in the chain, but always has the same compression $\Delta_{\text{doublet}} = 3 - \sqrt{3} \approx 1.2679$, and the same energy $E_{\text{doublet}} = 1/4$. We also note that the compressive force exerted by the system on the wall drops to $\mathcal{G} = 0$ here.

Thus, we will characterise the localised buckling that occurs between compression

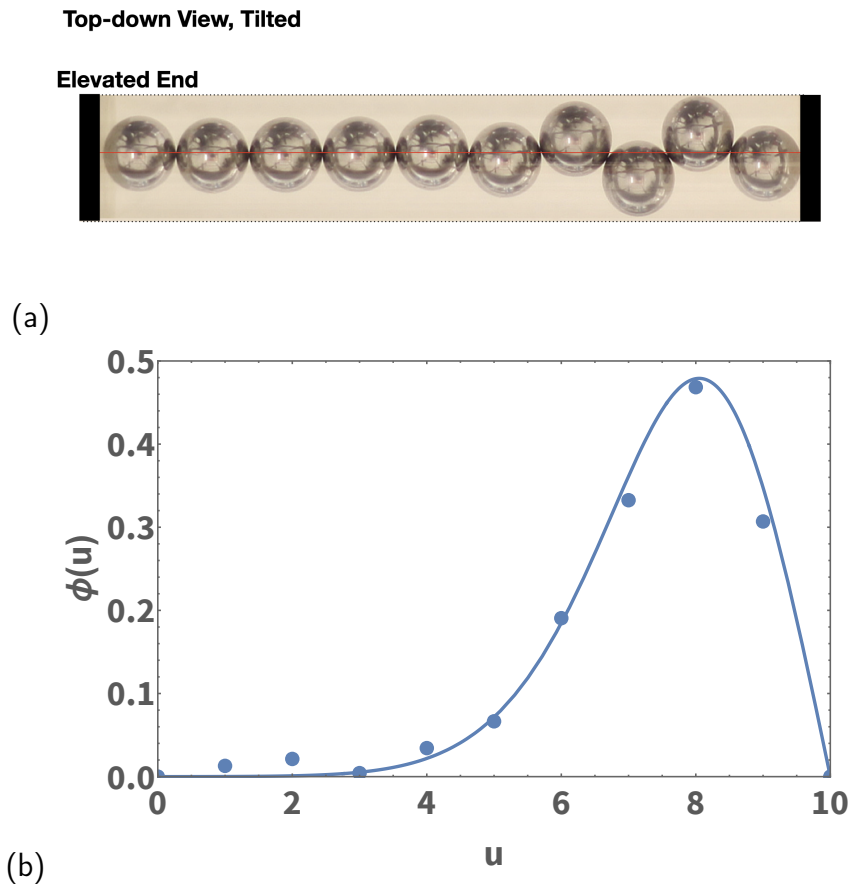

Figure 2.4: (a) View of a compressed and tilted linear line of spheres; the maximum of sphere displacement has moved towards the lower end of the cylinder. (Cylinder and sphere dimensions as in Figure 2.2, chain length 61.56mm, tilt angle $\alpha \simeq 7$ degrees.) (b) Theoretical results from the continuum model, compared with the measured profile, in terms of $\phi(u) = \tan\theta(u)$ (cf. Fig 2.2).

$\Delta = 0$ and the termination point associated with the doublet using the angle profile θ_n (see Figure 2.2), in particular the maximum value of the angle profile θ_{max}. This may take any value in the interval $0 \leq \theta_{max} \leq \pi/2$. For this analysis we developed a continuum description, where these angle profiles are approximated by functions of a continuous variable. We will discuss this method in the next chapter.

2.2 Adding a longitudinal force: Tilt

If we consider our previous system, except now the axis of symmetry of the cylindrical potential lies at an angle α to the horizontal, each sphere will experience a force due to the component of its weight acting along the axial direction. Writing this in our

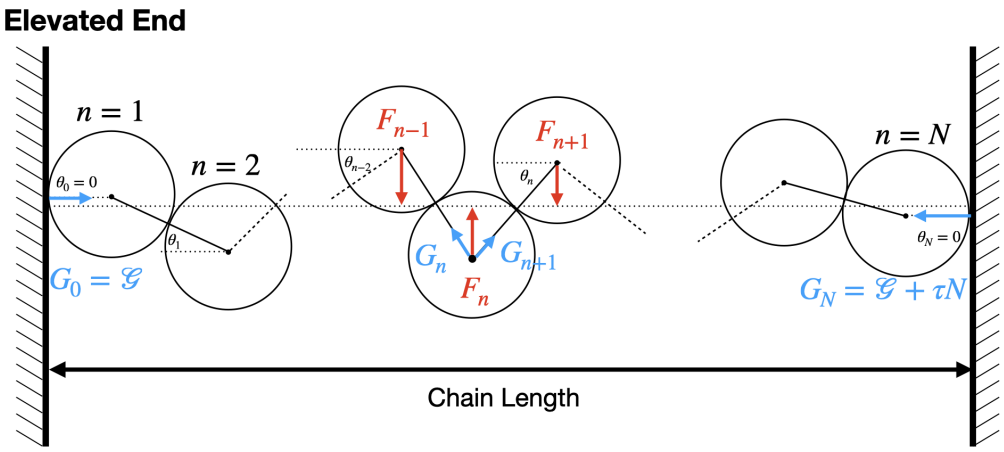

Figure 2.5: A modified version of Figure 2.1 showing the effect of the tilt force, τ.

dimensionless notation, we define the tilt variable τ as:

$$\tau = mg\sin(\alpha)/(kD), \tag{2.8}$$

where mg is the weight of a sphere, and kD is our force-scale as defined in the previous section. Here we will consider only the action of this longitudinal compressive force, where the chain is uncompressed by the boundary walls. In Chapter A3.3 we will discuss the combined action of tilt and compression by the boundary walls.

The addition of this tilt force modifies the iterative equations presented in the previous section, see Figure 2.5. Equation 2.6 remains unchanged, however Equation 2.5 becomes:

$$\theta_n = \arctan\left(\frac{y_n(\tau(n-1))\tan\theta_{n-1}}{\tau n}\right). \tag{2.9}$$

Again, equilibrium solutions may be found using the same shooting method described in the previous section. Compression of an equilibrium structure may still be calculated using Eqn (2.7).

The energy of the system, Eq (2.2), is modified by the addition of a term due to the

tilt: $\tau \sum_{n=1}^{N} x_n$, where x_n is the displacement of sphere n along the central axis of the system. It may be calculated from the angle profile using $x_n = 1/2 + \sum_{i=1}^{N-n} \cos\theta_{N-i}$. This results in the modified version of Eqn (2.2):

$$E = \frac{1}{2}\sum_{n=1}^{N} y_n^2 + \tau\left(\sum_{n=0}^{N}(n\cos\theta_n) - \frac{N}{2}\right). \tag{2.10}$$

2.2.1 Results of simulations with tilt

We first address the question: *what happens if the tilt is gradually increased from zero?*

It may be obvious that a *small* tilt will not render the chain unstable. We expect it to become unstable with respect to buckling at some critical value of tilt, $\tau = \tau_c$. We wish to determine τ_c (for specified N, the number of spheres) and describe what happens around the critical point. As an example, we choose $N = 10$, for which results are shown in Figure 2.6.

It is trivial to derive the energy of a straight chain (whether stable or not), $E_s = \tau N^2/2$, and we subtract this from calculated energies E (Eqn (2.10)), for simplicity of presentation,

$$\Delta E = E - E_s. \tag{2.11}$$

Hence the horizontal axis in Figure 2.6 represents the straight chain solution, which is stable in the range $0 < \tau < \tau_c$, where $\tau_c = 0.03557$ (as determined by using the stepwise method of Section 2.2), and unstable for higher values of τ.

One might have expected a bifurcation at the critical point τ_c such that a branch emerges that corresponds to a buckled solution, developing as τ is further increased, as in the classic description of Euler buckling of a beam [22], see Section 1.1. This is not the case here; there is no such "forward branch", but rather a "backward" one, which one may readily identify as *unstable*. In later sections, we will explore its nature. For now, let us ask: what happens to the stable system when τ reaches τ_c?

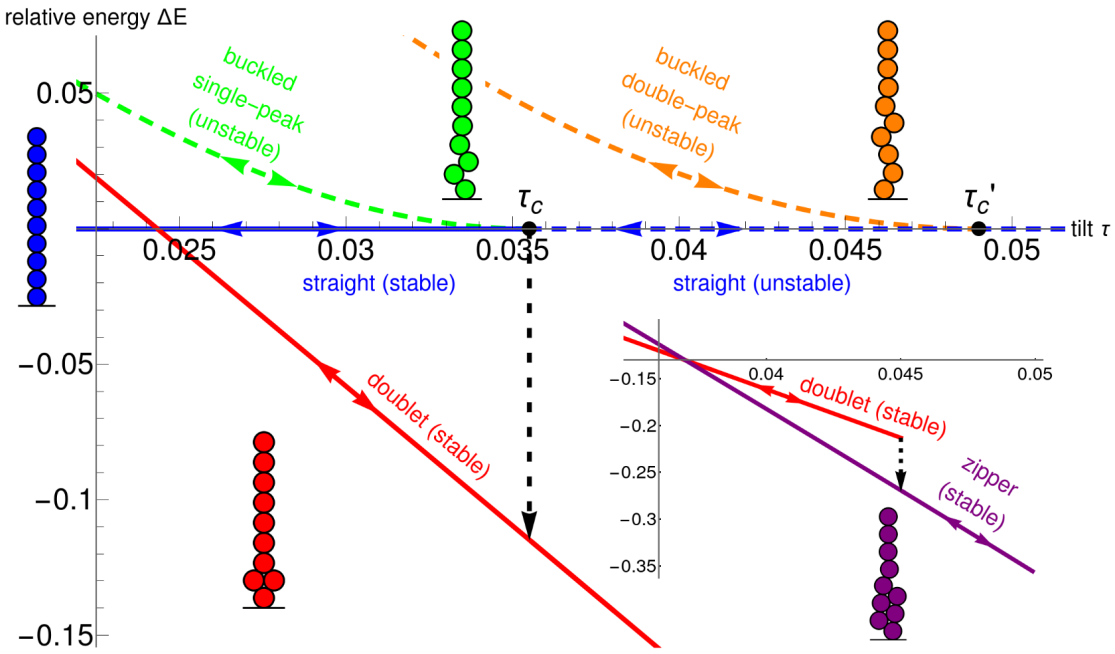

Figure 2.6: Bifurcation diagram for a system with $N = 10$, obtained from a combination of the soft sphere simulations (Section 5.2) and iterative method (Section 2.2) Shown is the variation of the energy difference $\Delta E = E - E_s$ of total energy E (Eqn (2.10)) and energy of the straight chain, E_s, as a function of tilt τ. Examples of the various structures described in the text are shown, with arrows indicating allowed directions of change of stable solutions. The transition from the doublet to the zipper structure is shown in close-up in an inset.

To answer this question we have had recourse to the deformable sphere model of Section 5.2. We equilibrate a linear chain of such spheres using gradient descent methods for energy minimisation and find that it is stable for $\tau < \tau_c$. Beyond this point, it falls into a doublet, if energy is minimised (see dashed black arrow in Figure 2.6). This type of state was encountered in our earlier study of buckling under compression [34]. The energy difference between the doublet structure and the linear chain is given analytically by

$$\Delta E_{doublet} = 1/4 - (3 - \sqrt{3})(N - 2)\tau. \tag{2.12}$$

If τ is now reduced, the system remains in the doublet state for $\tau < \tau_c$ and transitions to the linear chain only at $\tau = 0$. The stable straight chain with which we began this description is the state of lowest energy *only* for $\tau < 0.0246$ (from Eqn (2.12)). On the other hand, if τ is increased, the doublet structure develops into an extended double chain (similar to the zipper described in Figure 1.11).

For $\tau < \tau_c$ the bifurcation diagram includes the "backward branch" corresponding to an unstable state. The variation of energy close to τ_c is quadratic for this state, as Figure 2.7 shows. The critical value of tilt (for $N = 10$) is $\tau_c = 0.03557$.

Figure 2.8(a) shows examples of profiles of displacements f_n for the unstable state, obtained from simulations of the discrete $N = 10$ chain, for values of tilt just below τ_c. The profiles are characterized by a long tail of near zero displacements, with a peak below the ninth sphere and a substantial displacement also for the tenth sphere, which is in contact with the wall. We will return to the interpretation of these profiles and their scaling in the next chapter.

Our bifurcation diagram, Figure 2.6, shows also the variation of energy of an unstable higher energy double-peak structure, but we have not yet further analysed this state.

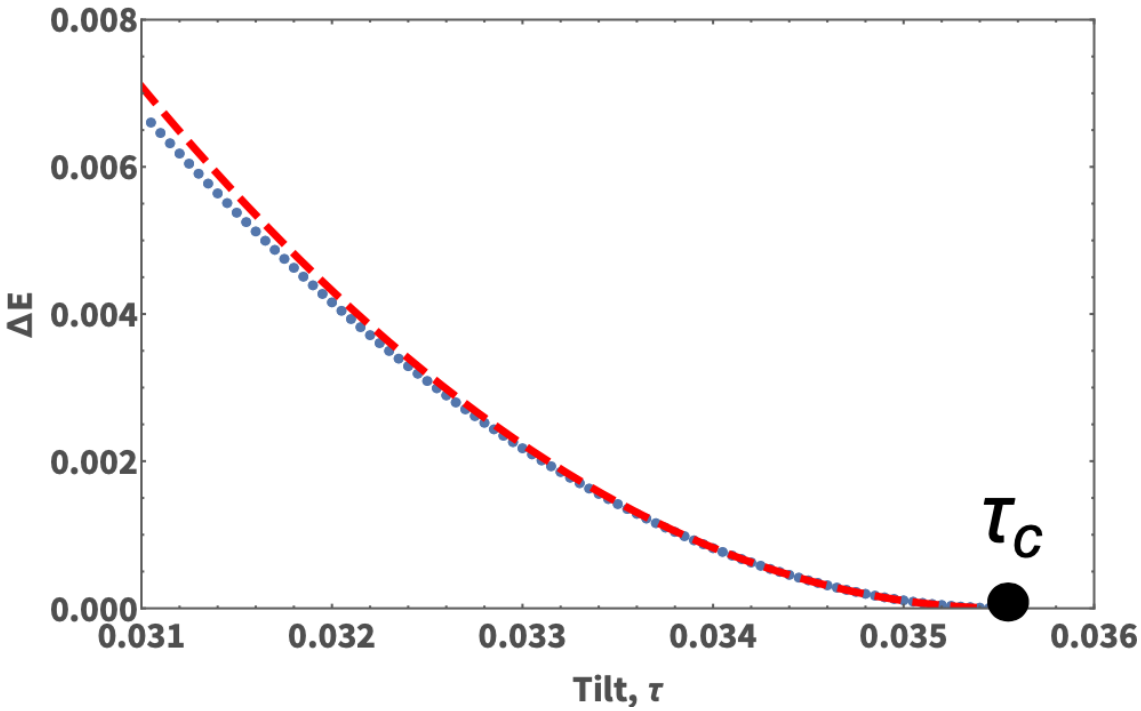

Figure 2.7: Close to the critical value of tilt, τ_c, the variation of the computed energy ΔE (Eqn (2.11)) (blue data points) for the unstable buckled structure indicated in Figure 2.6 is well fitted by a quadratic form (dashed red line). (Data shown is for N=10.)

2.2.2 Simple models for tilted systems

We can shed further light on the results with simple heuristic models as follows. The instability occurs where the local compressive force is largest, i.e. towards the bottom of the chain. Suppose we allow displacement of only the penultimate sphere, so that there is only a single variable (f, the displacement of the sphere, or θ, the angle associated with the line connecting the centres of the penultimate and the final sphere, which is in contact with the wall) describing the buckled state. The compressive force acting on sphere $N-1$ is due to the weight of the linear chain. At the onset of buckling its transverse component, $(\tau(N-2)+\tau(N-1))\sin\theta$ (the sum of the forces due to the contacts with spheres $N-2$ and N, respectively), overcomes the restoring force $f=\sin\theta$. It results in the estimate $\tau > (2N-3)^{-1}$ for buckling. It provides a crude, but fairly successful, estimate of τ_c.

A variation of this model allows equal and opposite displacement of the two spheres $N-1$ and $N-2$ (where sphere N is in contact with the wall). This more accurately

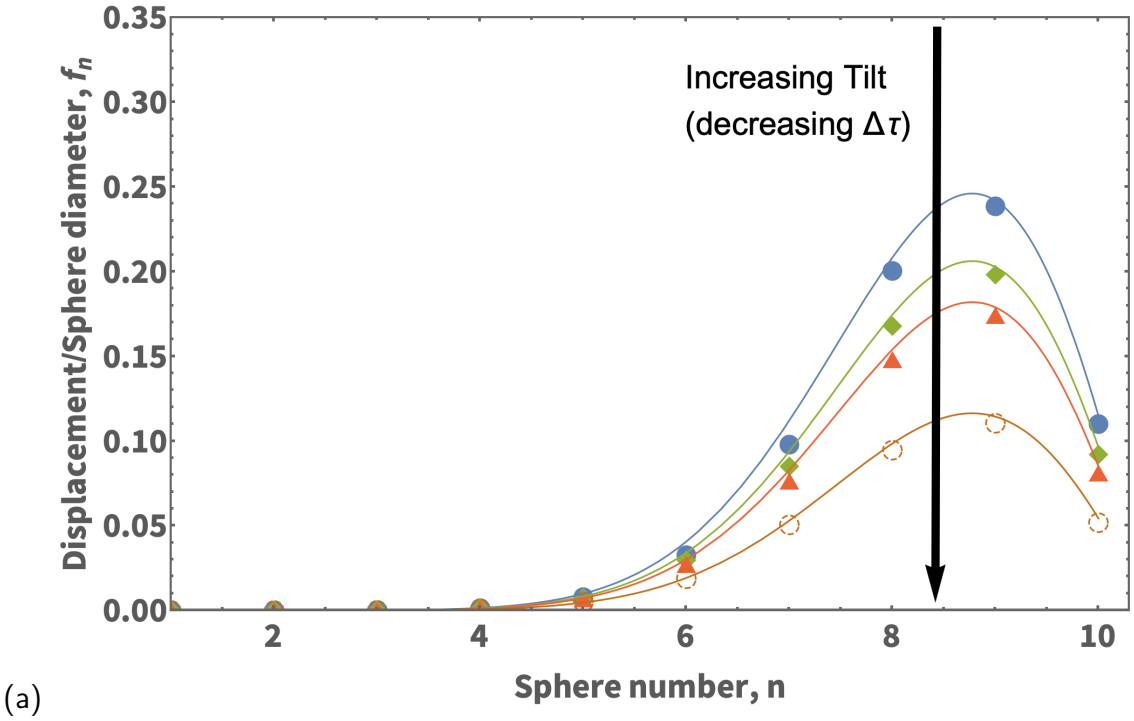

(a)

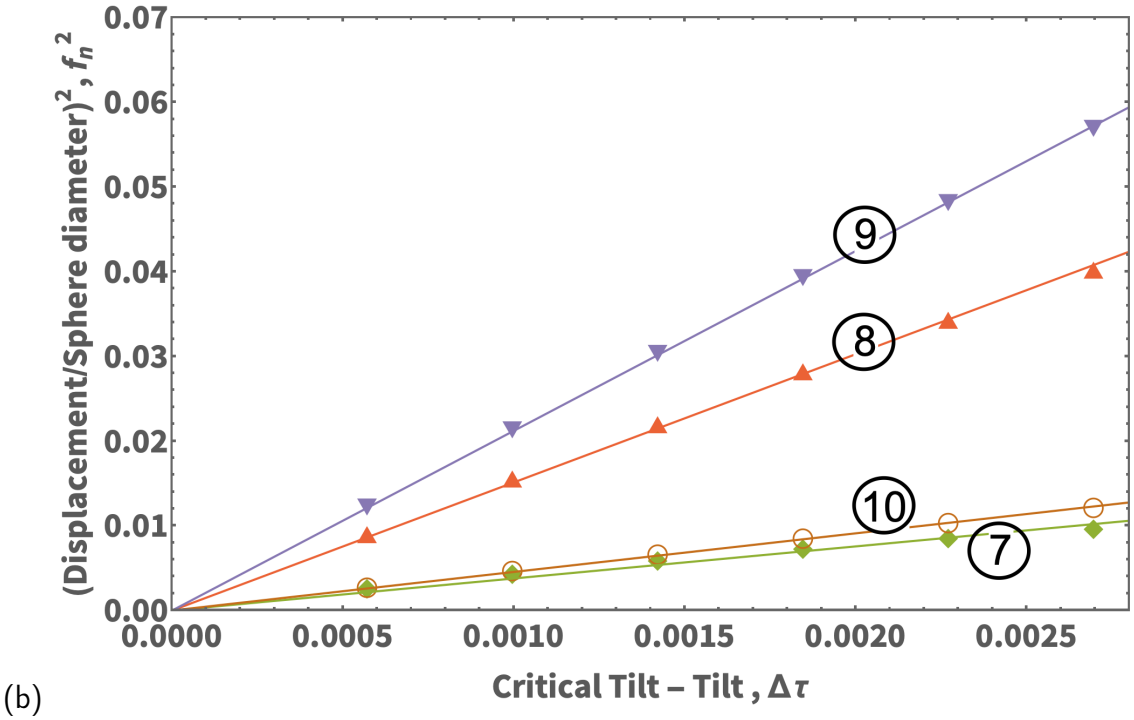

(b)

Figure 2.8: Simulation results for the (unstable) single peak solution shown in Figure 2.6. (a) Displacement profiles for values $\Delta\tau = \tau_c - \tau$ close to τ_c ($\Delta\tau = 0.0055, 0.0030, 0.0017, 0.0005$). The data points result from the discrete calculations (using the stepwise method), the solid lines are analytic solutions obtained from the continuum model, involving the Whittaker function; Chapter 3. (b) Square of the displacement, taken at spheres 7, 8, 9, 10, respectively, as a function of $\Delta\tau$. The linear scaling of the *square* of the displacement with $\Delta\tau$ is also reproduced in the simple heuristic model of Section 2.2.2 and the continuum model.

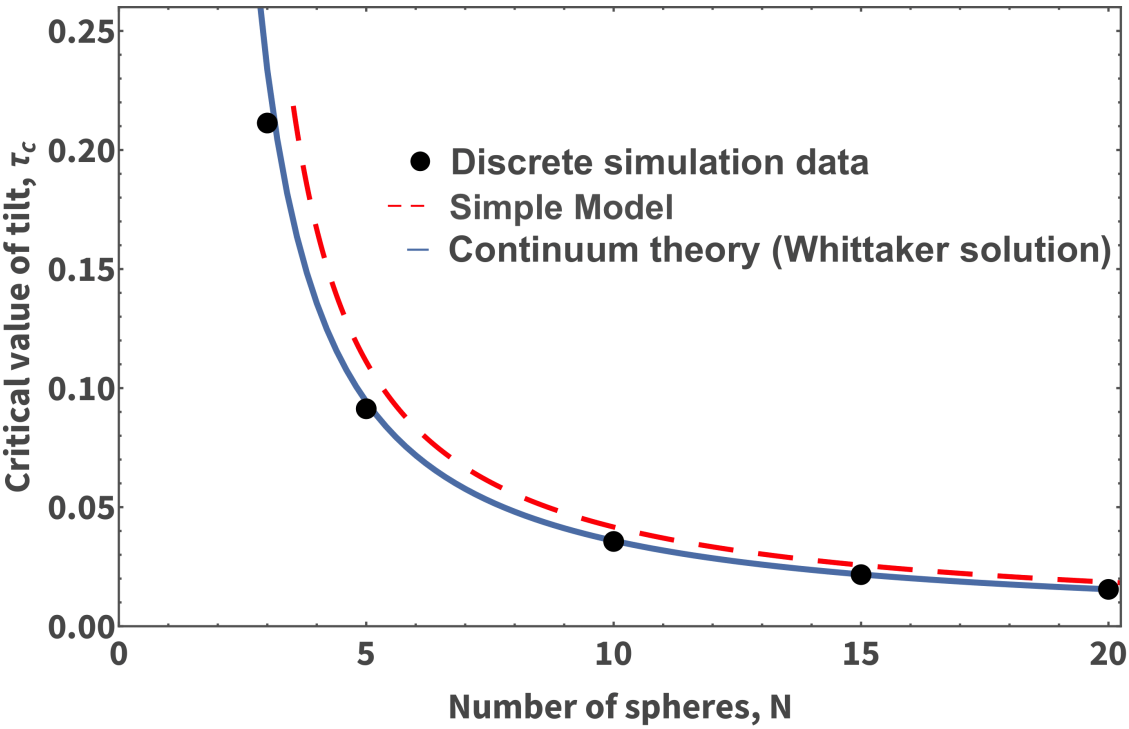

Figure 2.9: Variation of the critical value of tilt τ_c as a function of the number of spheres, N. The data points are from discrete simulations (iterative method), the solid line is obtained from numerical solutions for the roots of the Whittaker function (a prediction of the continuum model, see Chapter 3). Also shown is an estimate obtained from a simple ansatz for a displacement profile, Eqn(2.13) (dashed line).

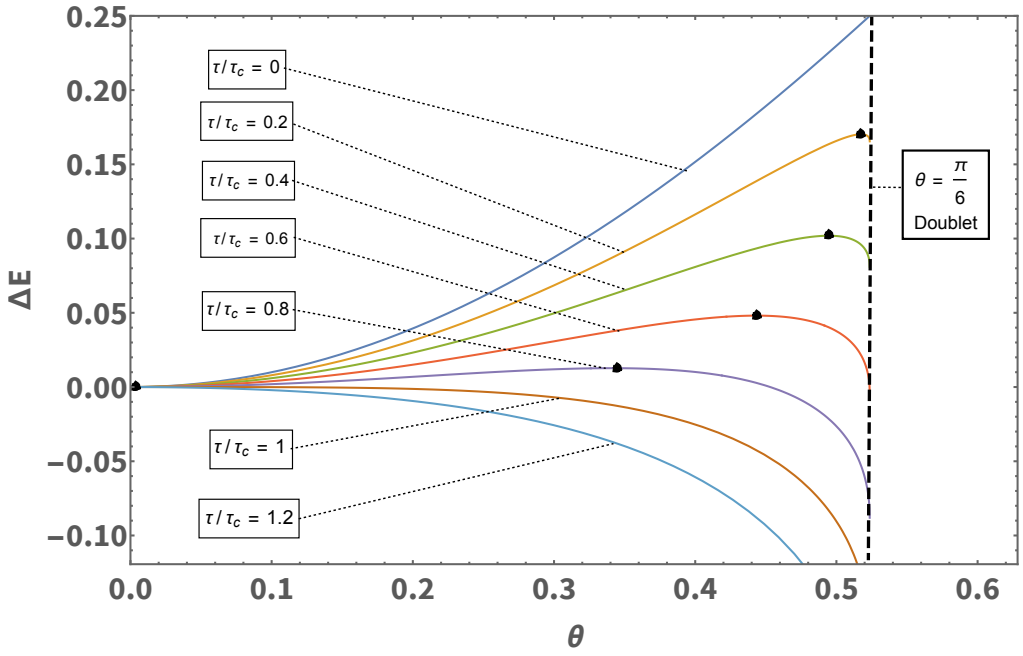

Figure 2.10: Variation of energy, Eqn (2.14), with angle θ and different ratios τ/τ_c for the simple model, in which only the two penultimate spheres are displaced by $f = \sin\theta$. For values of tilt in the range $0 < \tau/\tau_c < 1$ there are unstable solutions at finite value of θ, marked as black dots. For $\tau_c \geq 1$ the unstable solution has moved to zero, showing how unstable branch decays as $\tau \to \tau_c$.

describes the effect of localised buckling, and captures some of the behaviour of the structure as it approaches the doublet. It leads to an even better estimate for the value of tilt τ_c, at which the unstable solution vanishes,

$$\tau_c = [3(N-2)]^{-1}, \tag{2.13}$$

see Figure 2.9.

This trial set of displacements for two spheres involves a single parameter, displacement f, or angle θ, the latter being $\theta = \arcsin f$. The relative energy, Eqns (2.11) and (2.10), is given by

$$\Delta E(\theta) = \sin^2\theta + \frac{\tau}{3\tau_c}(2\cos\theta + \sqrt{1-4\sin^2\theta} - 3). \tag{2.14}$$

The maximum value of θ is $\pi/6$, which corresponds to the doublet structure. The model is terminated here since it does not have allowance for the additional contacts which arise at that point.

Figure 2.10 illustrates the form of this function for different values of τ. For $\tau < \tau_c$, the minimum at $\theta = 0$ corresponds to the stable straight chain solution indicated in Figure 2.6. The maximum corresponds to the unstable solution, represented in Figure 2.6. For $\tau = \tau_c$ there is only one stationary state, $\theta = 0$ (straight chain), and for $\tau > \tau_c$ it is unstable. We will return to this heuristic model when interpreting experimental work described in the next section.

2.3 Comparison with experiments: Systems with tilt

In [35] and as discussed in Section 1.3, it is possible to examine structures formed by chains of hard spheres under compression and tilt. Unfortunately, the results for hard spheres do not satisfactorily match the predictions made by the simulation methods

presented above, however we will provide explanations here as to why we believe this to be the case.

The experiments were carried out (by Ali Irannezhad, using the experimental apparatus discussed in 1.3) with metal spheres (sets of ball bearings with diameter $D = 9.5mm$ and mass $m = 3.52g$), confined in a cylindrical perspex tube (diameter $D_T = 34mm$) which was filled with vegetable oil to reduce friction (see Figure 2.11). The angle of tilt of the cylinder against the horizontal was determined using a digital spirit level (Neoteck NTK034). The cylinder was sealed with rubber stoppers at both ends; the surface of the stopper in contact with the spheres was covered with a circular plastic sheet to further reduce friction at the contact point.

In these experiments the restoring transverse force is provided by the curvature of the cylinder. The dimensionless tilt variable τ of Eqn (2.8) is then given by

$$\tau = \frac{1}{2}\left(\frac{D_T}{D} - 1\right)\sin\alpha, \tag{2.15}$$

as shown in Appendix A2.

If one simply tilts such a system, no instability is found until τ is much greater (e.g. by a factor 3 greater) than the τ_c that we have computed for ideal hard spheres. Hence friction is sufficient to hold the system in the unstable straight-chain arrangement of hard spheres, up to a point.

We rule out the use of large perturbations since these tend to force the system into the doublet arrangement over a very wide range of tilts. Instead we have tried to overcome the effects of friction by rolling the tube gently back and forth, thus providing a perturbation of the linear chain.

The experimental procedure was thus as follows. Starting from an initially linear arrangement of spheres the tube was tilted away from the horizontal by a tilt angle α. This was followed by ten cycles of manually rolling the tube back and forth with a fixed period of 10 seconds and a specified amplitude. An image is taken after the rolling is

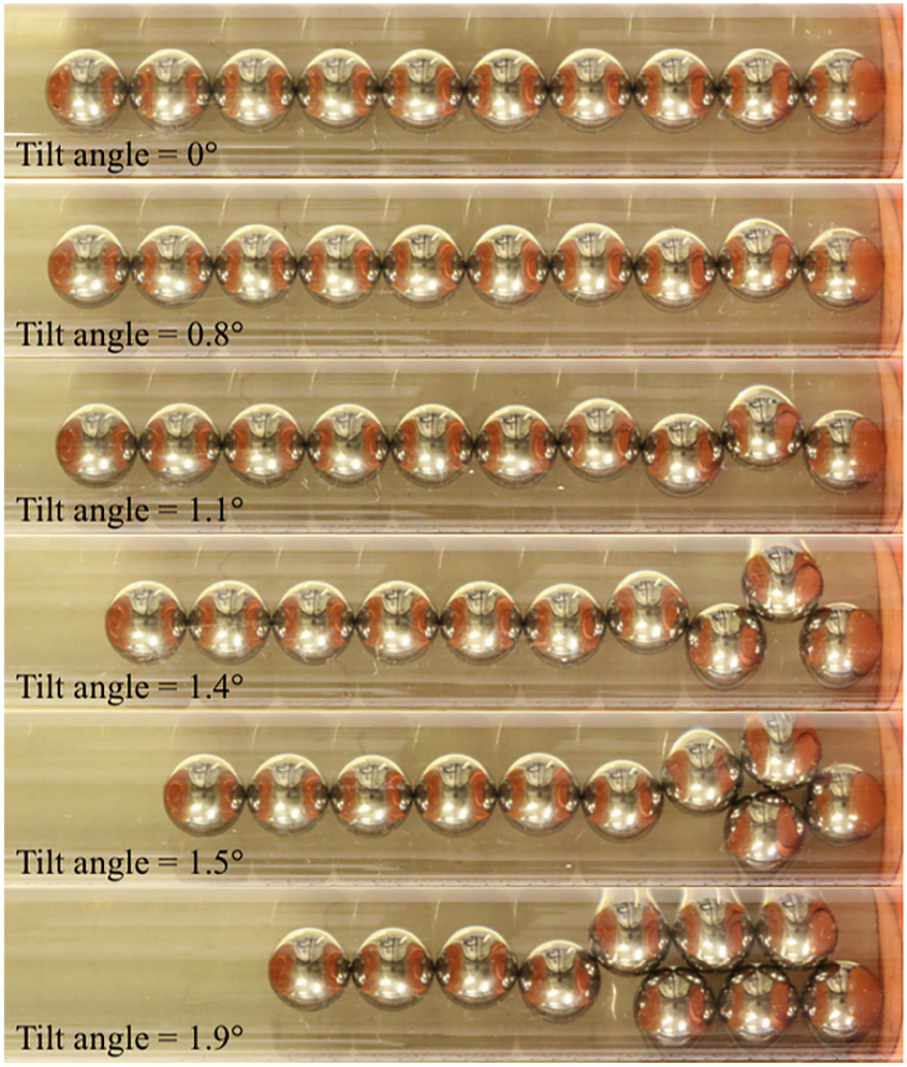

Figure 2.11: Sphere arrangements obtained using the rolling procedure described in the text. The examples shown are the straight chain (no tilt), buckled single peak structures for tilt angles 0.8, 1.1 and 1.4 degrees, respectively, a "skewed doublet" structure for 1.5 degrees, and a 'zipper' structure for 1.9 degrees. (The presence of oil in the tubes results in optical distortion. We have corrected for this in these images by re-scaling the photographs by a factor of 2.04 to result in circular shapes for the sphere. Sphere diameter 9.50mm, inner tube diameter 34mm, uncertainty in angle measurements, 0.03 degrees. Rolling amplitude, 30mm.)

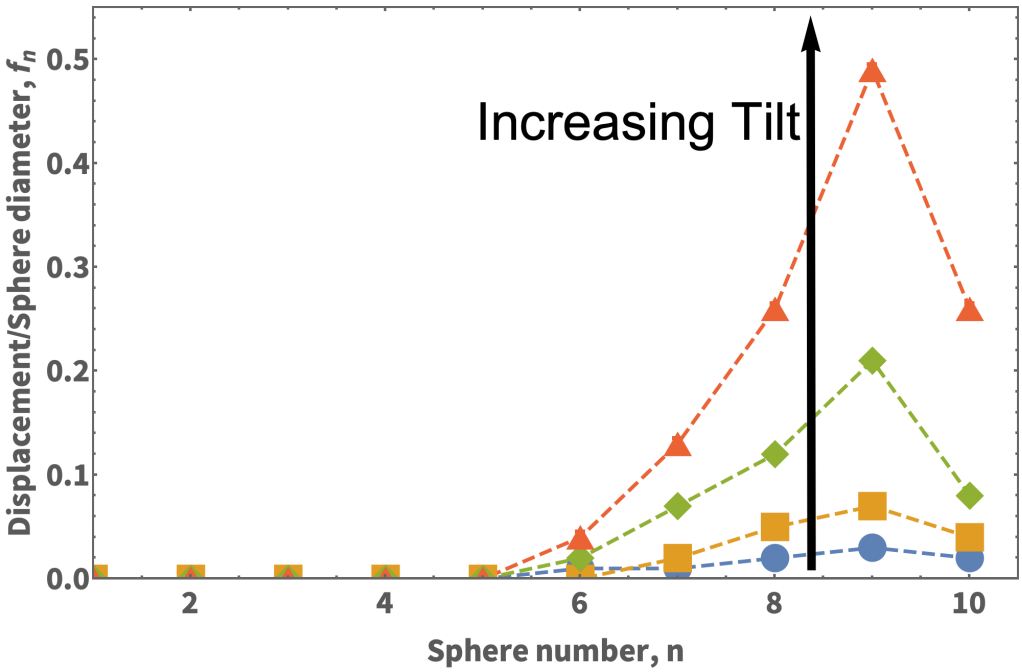

Figure 2.12: Experimental displacement profiles for (from bottom to top) tilt angles 0.40, 0.80, 1.10 and 1.40 $\pm$0.03 degrees, corresponding to $\tau = 0.009$, 0.018, 0.024 and 0.0315 (using Eqn (2.15) for conversion).

stopped; Figure 2.11 shows examples of sphere arrangements for six different values of tilt.

Image analysis using ImageJ [47] results in profiles of sphere displacement from the tube axis. Experiments were repeated three times for each angle; in each of these runs we started from an initially linear chain.

We find that once the rolling is stopped, even for values of tilt well below τ_c, the system does *not* return to the linear configuration. The experiments consistently resulted in the formation of a single peak zig-zag configuration, similar in form to the unstable equilibrium state discussed above. All profiles are asymmetric, with a maximum displacement at sphere 9, and a substantial displacement also for sphere 10, which is in contact with the flat stopper at the end of the cylinder.

However, while in the frictionless case the displacement amplitude decreases as the critical value of tilt is approached (Figure 2.8), friction causes the observed displacement to *increase* with tilt, as shown in Figure 2.12. In Figure 2.13 we show the maximum displacement (i.e. the displacement of sphere nine) as a function of tilt τ for

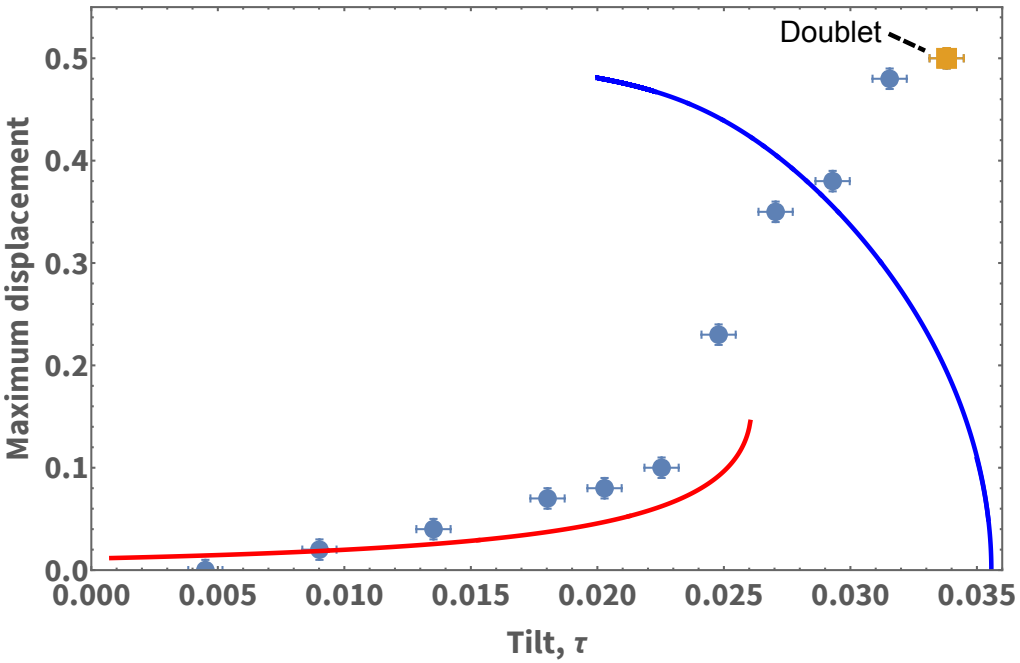

Figure 2.13: Contrasting experimental and simulated results for maximum displacement (i.e. corresponding to displacement of sphere 9) as a function of tilt τ. In the simulation (solid blue line) the amplitude of the *unstable* buckled state decreases to zero at the critical value τ_c, where the spheres rearrange to form a doublet structure. In the experiment (data points) the buckled state is friction-arrested, with an increasing amplitude as the doublet is approached. The solid red line is the result of a simple heuristic model, as discussed in Section 2.2.2.

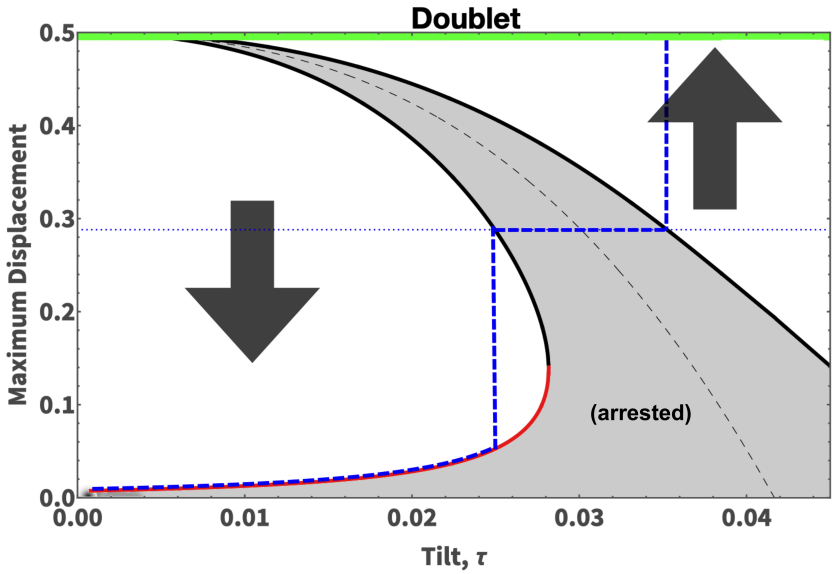

Figure 2.14: In a simple heuristic model, as discussed in Sections 2.2.2 and , an initial configuration, displaced from a straight line, is arrested by friction if it lies in the shaded region. This figure shows the region for a sample value of $\mu = 0.12$. In other regions of the diagram, friction is overcome; the system moves as indicated by the arrows, until arrested. This figure shows how the combination of friction and tilt affect a chain with a given initial displacement. The dotted blue line represents the initial maximum displacement of that state, while the dashed blue line shows the observed state. The red line corresponds to that in Figure 2.13. (The black dashed line is the unstable branch)

both our numerical and experimental data. This highlights the different behaviour as the critical point is approached.

We will address this discrepancy between theory and experiment through the addition of friction to the simple heuristic model. We will do this by noting that the derivative of the energy of the system with respect to the characteristic angle of the model, $dE/d\theta$, may be equated to the restoring force acting on the displaced spheres. We claim that for restoring forces below some threshold value, the structures are arrested and will not move to the lower energy structures predicted by the original theory. This is an approximation, as there are multiple contributions to the friction in the experimental system - the friction between contacting spheres and the friction between the spheres and the surface of the confining cylinder. Our model combines these.

Given our choice of dimensionless quantities, with forces made dimensionless through division by kD, we will equate this threshold value with the coefficient of friction, μ. Therefore, for a given value of μ, we can define a region where the structures are

"arrested", i.e. their displacement will remain fixed in this region regardless of tilt. For a sample value of $\mu = 0.12$, this is given by the grey region in Figure 2.14. Outside this region, the behaviour depends on the value of tilt. For lower values of tilt, the displacement of the structures falls to the arrested region. This is demonstrated by the large grey arrows in Figure 2.14. For larger values of tilt, or initial displacement of the spheres, the displacement increases until the doublet structure is reached. Note that the red curve in Figure 2.14 corresponds to what is shown in Figure 2.13.

In both experiment and this crude theory, upon increase in tilt the single-peak buckled structure eventually becomes unstable and the doublet structure emerges. A further increase in tilt renders also the latter unstable, resulting in what we called the 'zipper structure", see bottom photograph in Figure 2.11.

2.4 Conclusions

In this chapter we examined the original iterative relationship described in [43], and showed how it may be extended to the case of a line of tilted spheres.

In vague terms, the system presents a type of buckling under tilt which, in one form or another, is quite general. Structures that fail under load may do so continuously (although possibly with discontinuous secondary consequences) or *catastrophically*. The latter word has a modern mathematical meaning which may well apply to our case.

The stability of the linear chain and the presence of the buckled structure in our experimental results, serve to highlight the role of friction in arresting structures that would otherwise be unstable. In this regard, these findings are reminiscent of various columnar structures, composed of tennis balls, that are stable only due to the presence of friction between contacting balls [48]. While the incorporation of the simple theory of states arrested by friction brings the experimental results broadly in line with the theoretical predictions, a detailed comparison is impossible. We will propose a comparison with systems of bubbles in Part II of this thesis, where the assumptions of

our theory match the experimental conditions more precisely.

In many cases in this chapter we have had reason to refer forward to the results of the next chapter, the continuum model: to describe parameters such as the critical tilt τ_c and the prediction for variation of parameters such as maximum angle θ_{max} as a function of the compression and/or tilt of the system. In the next chapter we will develop this continuum theory fully, showing how it arises from the original iterative description of these structures. We will show how analytic approximations can provide an insight into the behaviour of this system in various limits.

3 The continuum model for buckled chains

In this chapter we will make a curious proposition. What if the buckling profiles we observed in Chapter 2 were discrete samples of some underlying continuous curve? Turning continuous systems into discrete ones is commmonplace, such as in digital signal processing [49] and numerical analysis [50]. Here, however, we argue that the reverse is both useful and interesting when applied to the buckled chain of spheres confined in the harmonic potential. We consider our discrete *difference equations* and we ask, is it possible to find the underlying *differential equation*, whose solutions are our familiar buckling profiles? In this chapter we shall discuss this, transforming our discrete system into a continuous one, and using the methods of solving ODEs to further probe the behaviour of the buckled chain.

The structure of this chapter is as follows. In section 3.1 we introduce the nonlinear differential equation of the continuum model, Eqn (3.2), and show some sample solutions for specific values of compression and tilt. In Section 3.2 we present several approximations to the equation which allow for *analytical* solutions in terms of scaled Jacobi, Airy, and Whittaker functions, respectively. The properties of these solutions are discussed in Section 3.3 (a more detailed exploration of the Jacobi solutions is reserved for the next chapter), examples are shown in Figure 3.2. In Section 3.4 we present our results in the form of a phase diagram. Mathematical details are mostly confined to the Appendices.

The progression of successive approximations in our mathematical description is outlined in Table 3.1, as a guide to the sections that follow, and relevant publications. For now, we will limit the experimental and numerical data shown in the following to $N = 10$ spheres; in our analytical expressions N enters simply as a parameter. We will investigate the N-dependence of properties of the system in a later section.

It is important to note that this is not a true continuum limit in the mathematical sense, as we neither explore the limit of $N \to \infty$ or $D \to 0$, but rather our description of the problem in terms of continuous profiles provide curves from which the discrete profiles can be sampled.

3.1 The continuous formulation

3.1.1 Differential equation

Equilibrium configurations of contacting hard spheres in a harmonic confining potential (with tilt), as shown in the previous chapter, result from a balance of forces. In the previous chapter, we showed how the force balance leads to a set of iterative equations (Eqns (2.6), (2.5)) for the transverse forces acting on the spheres, and the angles θ_n (see Figure 2.5 for notation) between successive lines of contact and the longitudinal direction. These discrete equations have been solved numerically using the shooting method, as discussed in the previous chapter, and the solutions produce the angle profiles, θ_n.

In the absence of tilt we reformulated the discrete equations as a second order differential equation for which it is convenient to use as a dependent variable $\phi(u)$, where

$$\phi(u) = \tan\theta(u). \tag{3.1}$$

The variable u replaces the index n in the discrete formulation. In Appendix A3.1 we

Scenario	Equation	References
Discrete system with *tilt* τ *compressive force* $\mathcal{G}+\tau(n-1)$ resulting in *compression* Δ	Difference equations, Iterative numerical solutions for forces and displacements	Ch. 2 Ref. [34, 41]
Continuous approximation compressive force $G(u)=\mathcal{G}+\tau u$	Differential equation $\phi''(u)=-4\phi(u)+\frac{\phi(u)}{G(u)\sqrt{1+\phi^2(u)}}$ numerical solutions	Ch. 3 Eqn (3.2) Ref. [34]
For $\tau=0$, $\phi<1$ Approximation as reduced equation	Differential equation $\phi''=\kappa^2\phi-2\left(1+\frac{\kappa^2}{4}\right)\phi^3$ Jacobi function solutions	Chapter 4 Eqn (3.4) Ref. [51]
Linear approximation For $0<\tau\ll 1$ Approximation by Whittaker equation	Linear differential equation $\phi''=\left[-4+\frac{1}{\mathcal{G}+\tau u}\right]\phi$ Whittaker function solutions	Sect. 3.3.2 Eqn (3.7) Ref. [35]
For $0<\tau\ll 1$, $\tau/\mathcal{G}\ll 1$ Approximation by Airy equation	Linear differential equation $\phi''=\left[\frac{1}{\mathcal{G}}\left(1-\frac{\tau u}{\mathcal{G}}\right)-4\right]\phi$ Airy function solutions	Sect. 3.3.3 Eqn (3.9)

Table 3.1: Outline of the different scenarios, successive approximations, and differential equations discussed in the text (see in particular Section 3.2), together with some relevant references. Examples of profiles for Jacobi, Airy and Whittaker solutions are shown in Fig 3.2.

derive the differential equation in the presence of tilt as

$$\boxed{\phi''(u) = -4\phi(u) + \frac{\phi(u)}{G(u)\sqrt{1+\phi^2(u)}}.} \tag{3.2}$$

In this "full continuum equation with tilt" the axial component of the (dimensionless) compressive force $G(u)$ varies linearly with position u, $G(u) = \mathcal{G} + \tau u$. Here $\mathcal{G}$ is the magnitude of the compressive force (in the axial direction) at the (possibly elevated) end ($u = 0$) of the chain of N spheres and τ is the dimensionless *tilt* parameter. (In the experiments, τ is proportional to the sine of the angle of tilt; see Eqn (2.8).) We note that for the case considered here there are only repulsive forces, so $G(u)$, and in particular $\mathcal{G}$ is never negative.

Eqn (3.2) is the central equation of the continuum model. We will examine its solutions for the hard-wall boundary conditions $\phi(0) = \phi(N) = 0$ (which corresponds to hard walls that are perpendicular to the cylindrical axis, see Figure 2.2) and given values for compressive force at the upper (elevated) end, $\mathcal{G}$, and tilt τ.

Eqn (3.2) was previously only presented and analysed in this form for the case $\tau = 0$, where Jacobi functions provide approximate solutions [51]. The presence of tilt (i.e. a finite value for τ) leads to further (approximate) analytical solutions, now in terms of Airy and Whittaker functions.

3.1.2 Compression

In contrast to our experimental set-up, where we fix compression by choosing the distance between the two stoppers at the ends of the chain, here we *compute* profiles for given tilt τ and various values $\mathcal{G}$, evaluating compression Δ from the profile $\phi(u)$ via a continuum formulation of Eqn (1.3):

$$\Delta = N - \int_0^N \frac{du}{\sqrt{1+\phi^2(u)}}; \tag{3.3}$$

see also Appendix A3.2.

As with experimental data we can thus plot quantities of interest such as peak position or peak height as a function of compression.

3.1.3 Numerical results

Before proceeding to analytic approximations, it is instructive to discuss numerical results for solutions of the full equation, Eqn (3.2). The equation is solved numerically, using Mathematica's in-built shooting method, for the required boundary conditions $\phi(0) = \phi(N) = 0$.

Numerical results for compression only

Figure 3.1(a) shows examples of profiles of $\phi(u)$ for $N = 10$ in the absence of tilt ($\tau = 0$), computed for several values of the compressive force $\mathcal{G}$. The profiles are symmetric around the centre of the chain.

In the limit in which compression $\Delta \to 0$ the peak height varies as $\phi_{max} \sim \Delta^{1/2}$, with a linear variation for higher values of compression (see Figure 3.9). The square-root scaling may be understood as follows. For small $\phi(u)$ we have $\Delta \simeq \frac{1}{2}\int_0^N \phi^2(u)du$ (see Eqn 4.5). Approximating $\phi(u)$ as a triangular profile of peak height ϕ_{max} gives the above scaling. We will return to this in the next chapter, when discussing analytical solutions of a reduced equation in terms of scaled Jacobi functions.

Numerical results for compression and tilt

In Figure 3.1(b) we show that the presence of a finite tilt results in a shift of the peak away from the centre of the chain (as seen in Figure 2.4). Starting at $\tau > 0$ and increasing $\Delta > 0$ results in the localised buckling peak forming away from the centre of the system. The position of this buckling peak will shift slightly as Δ is increased, until a critical value of Δ_c is reached. Beyond this point, the single-peak structure requires an extensive force $\mathcal{G} < 0$ to be maintained, and instead collapses.

A similar outcome is reached if a structure of a given compression at $\tau = 0$ is tilted,

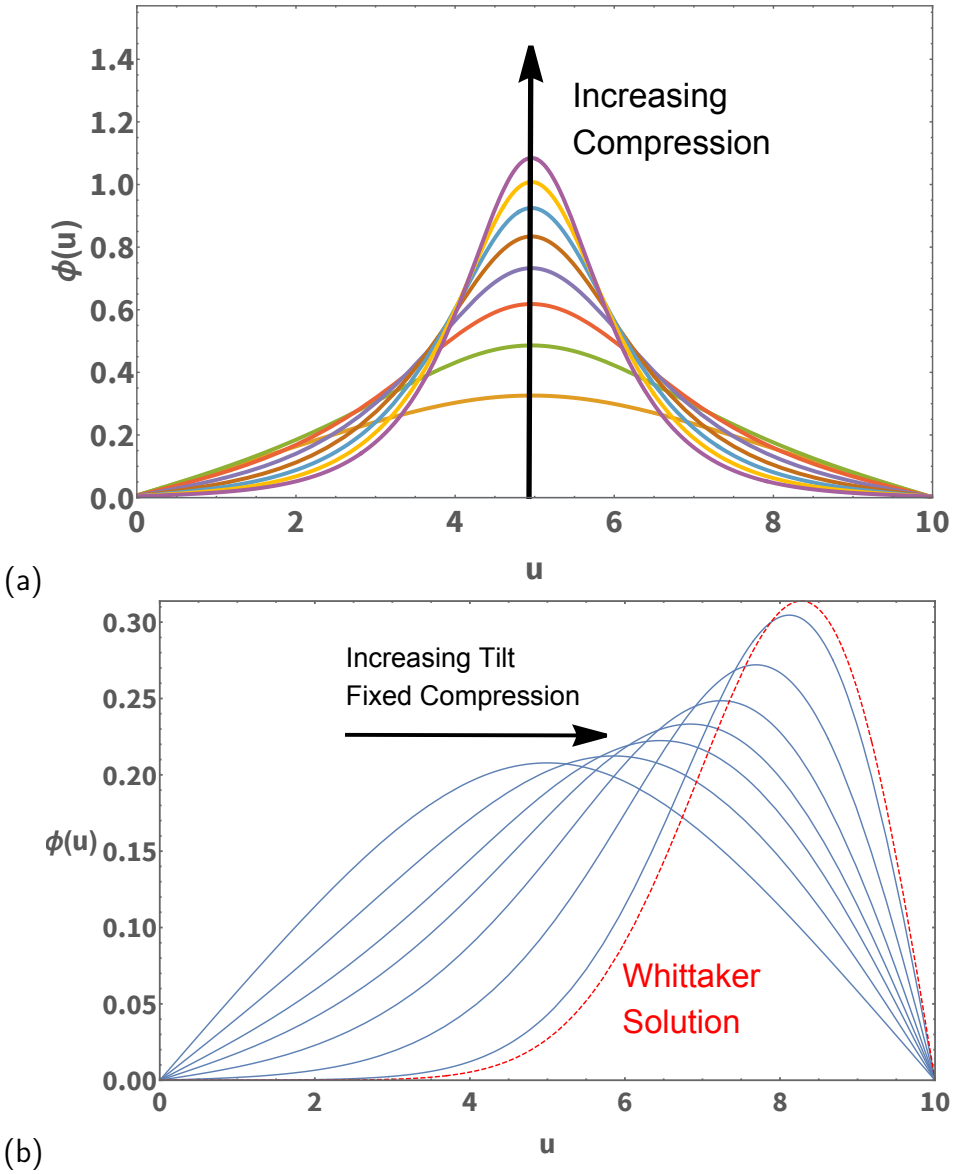

Figure 3.1: Results from numerical solutions of the full equation, Eqn (3.2), for a chain of $N = 10$ spheres under compression. (a) Examples of profiles of $\phi(u)$ in the absence of tilt ($\tau = 0$) for compressive forces in the range $\mathcal{G} = [0.185, 0.257]$, resulting in compression Δ in the range from 0.1 to 0.6. (b) For fixed compression (here $\Delta = 0.1$) the introduction of a finite value of tilt leads to a shift of the peak away from the centre. Shown as a red dashed line is the limiting case for the absence of a compressive force at the top end, i.e. $\mathcal{G} = 0$; this is the Whittaker solution, Eqn (3.12), which we will discuss in Section 3.3.2.

while adjusting the position of the top wall to maintain that compression. At a given value of $\tau = \tau_c(\Delta)$, the structure will also require that $\mathcal{G} < 0$, resulting in collapse of the system to a doublet or zipper state. This $\Delta - \tau$ boundary is shown in Figure 3.7.

A detailed discussion of these cases will also be provided in Section 3.3, where we will discuss them through the lens of the Airy and Whittaker functions.

3.2 Approximations of the full equation

The differential equation, Eqn (3.2), may be reduced by various reasonable approximations, resulting in forms which have analytic solutions, as summarised in Table 3.1. These provide insight into the properties of (numerical) solutions of Eqn (3.2) for different ranges of compression and tilt (Section 3.4).

3.2.1 The case of small compression in the absence of tilt

We first consider the absence of tilt, $\tau = 0$, for which there is a constant compressive force $G(u) = \mathcal{G}$. Taylor expanding the square root in the denominator of the right hand side of Eqn (3.2) to order ϕ^2, one obtains the *reduced* equation,

$$\phi'' = (\mathcal{G}^{-1} - 4)\phi - \frac{\phi^3}{2\mathcal{G}}. \tag{3.4}$$

By making an appropriate change of variables, $\phi = 2\sqrt{\frac{m}{2m-1}(1-4\mathcal{G})}y$, and $u = \sqrt{(2m-1)\frac{\mathcal{G}}{1-4\mathcal{G}}}x$ this can be re-written in the form of the *Jacobi differential equation*

$$y'' = -(1-2m)y - 2my^3, \tag{3.5}$$

with $0 < m < 1$. Its analytical solution $y(x) = cn(x|m)$ is the Jacobi *cn* function [50], $\sqrt{m}$ is called the (elliptic) modulus. We will discuss the details of the Jacobi solutions in the next chapter, and explore how they describe the localisation effects and N dependence of profiles under compression.

3.2.2 Compression and tilt

In the case of finite tilt, $\tau > 0$, analytical solutions in terms of Whittaker or Airy functions are available if one neglects the ϕ^2 term in the denominator of the square root in the full equation, Eqn (3.2), and thus considers the *linear* equation

$$\phi'' = \left[-4 + \frac{1}{\mathcal{G} + \tau u}\right] \phi. \tag{3.6}$$

Whittaker equation

By introducing $\tilde{u} = u + \mathcal{G}/\tau$ we put this in the form of

$$\phi'' = \left[-4 + \frac{1}{\tau \tilde{u}}\right] \phi. \tag{3.7}$$

Equation (3.7) is a special case of the *Whittaker Equation*

$$\frac{d^2 w}{dz^2} = \left[\frac{1}{4} - \frac{k}{z} + \frac{(\frac{1}{4} - \mu^2)}{z^2}\right] w, \tag{3.8}$$

for $z = 4i\tilde{u}$, $\mu = 1/2$, $k = 1/(4\tau)$, and renaming w as ϕ.

Here we concentrate on the case $\mathcal{G} = 0$ (i.e. $\tilde{u} = u$), corresponding to experiments in which the upper end of the chain is not in contact with the wall. The exact solutions of Eqn (3.7) for our boundary conditions can then be written in terms of Whittaker functions, $M_{k,\mu}(z)$; see Section 3.3.2.

The Whittaker solution defines only a single solution for a given value of N (this gives a prediction for the critical value of tilt, where $\mathcal{G} = 0$, for that given N). In order to explore the effect of tilt *and* compression on the system, we make a different approximation which leads to the Airy equation, as discussed in the next section.

Small tilt and a finite compressive force: Airy equation

For finite $\mathcal{G}$ and $\tau N/\mathcal{G} \ll 1$, we we may retain only the lowest order term in $\tau u/\mathcal{G}$ in Eqn (3.6), resulting in:

$$\phi'' = \left[\frac{1}{\mathcal{G}}\left(1 - \frac{\tau u}{\mathcal{G}}\right) - 4\right]\phi. \tag{3.9}$$

By making a change of variable from u to an appropriately defined x (see Appendix A3.3) and renaming ϕ as y we obtain the familiar *Airy equation*,

$$y''(x) = xy(x), \tag{3.10}$$

which has analytical solutions in terms of the Airy *Ai* and *Bi* functions. In Appendix A3.3 we derive the exact solutions of Eqn (3.9) in terms of these Airy functions; we will discuss the properties of these solutions in Section 3.3.3.

3.2.3 The form of the analytical solutions

Figure 3.2 shows examples of the special functions used here, over an extended range. One may choose as a solution (with hard wall boundary conditions) any range between two zeroes (corresponding to the boundary conditions $\phi = 0$ at each end). These are the 'higher modes of buckling', analogous to those we discussed for Euler buckling in Section 1.1. We will not address those higher modes here, in general they form for much higher compressive forces and thus energies.

In the next section we explore the properties of the analytic solutions in terms of Jacobi, Airy and Whittaker functions.

3.3 Properties of analytical solutions

Analytical solutions result in relationships between the experimental parameters compression, tilt and the number of spheres, and the observed quantities peak position and peak height. They also enable us to predict the critical value of tilt for sphere

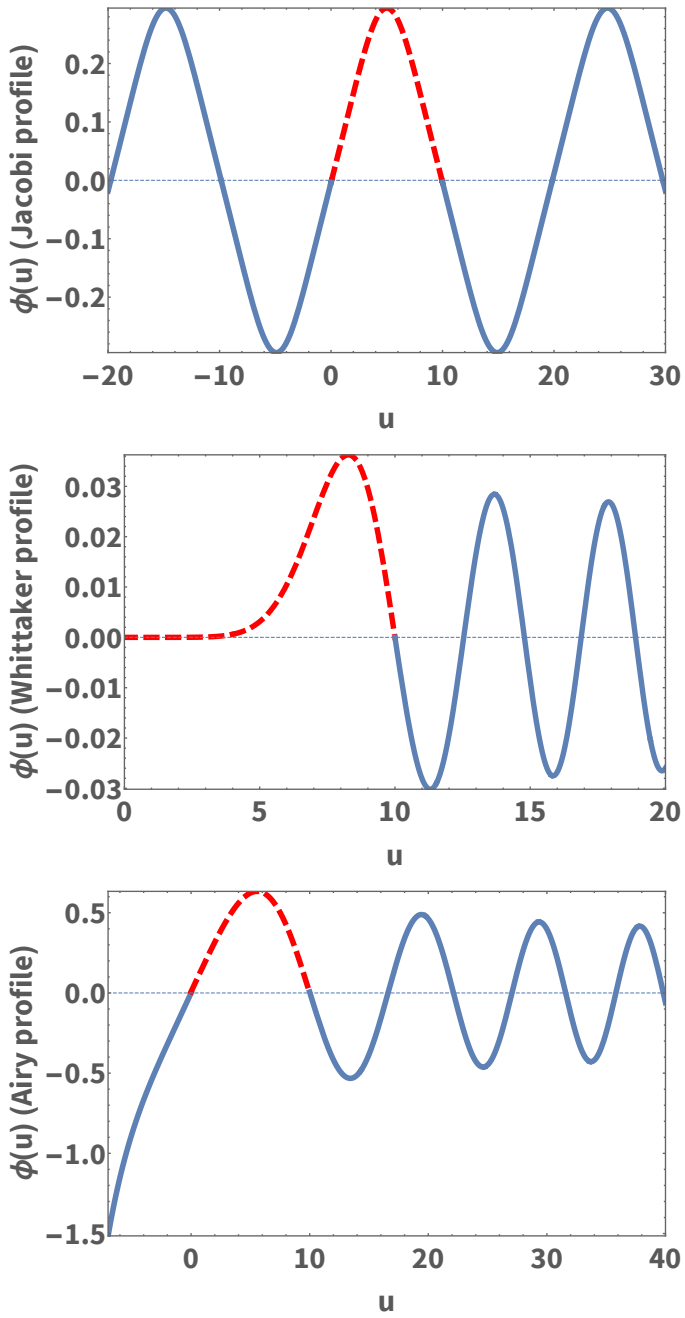

Figure 3.2: Examples of the analytic functions used in this work, shown over a wide range. Only sections such as those displayed as red-dashed lines are of relevance here; they fulfil the required boundary conditions, $\phi(0) = 0$ and $\phi(N = 10) = 0$.

detachment (where $G(0) = \mathcal{G} = 0$). Each of the analytical results offers a different, limited perspective on experimental features.

Using Jacobi functions one arrives at the relation between peak height and compression in terms of elliptic integrals. Using Airy functions establishes a relation between the position of the profile maximum and tilt. Whittaker functions enable a prediction of the critical value of tilt at which detachment of the spheres from the top wall occurs for (low values of) fixed compression.

3.3.1 Compression only: Jacobi functions

For values of compression $\Delta \leq 0.3$, and in the absence of a longitudinal tilt force, solutions of the full continuum equation are well approximated by scaled Jacobi functions. An example of such a profile was already shown in Fig 3.2(a).

For the case of the hard wall boundary conditions considered here, i.e. $\phi(0) = \phi(N) = 0$, the solution of the reduced equation in the absence of tilt ($\tau = 0$), Eqn (3.4), is given in terms of the scaled Jacobi *cn* function as

$$\phi(u) = \phi_{max} cn\left(\sqrt{(\mathcal{G}^{-1} - 4)/(2m - 1)}(u - N/2)|m\right), \tag{3.11}$$

where the so-called modulus, $\sqrt{m}$, is related to the period of the Jacobi functions, and thus N. The derivation of this solution, and a discussion of its properties, will be discussed in the next chapter.

3.3.2 Whittaker functions and the critical tilt for detachment

From experiments and numerical solutions for both the discrete system and the full continuum equation (see Figure 3.1(b)) one finds that (for given compression Δ) there is a critical value of tilt, $\tau_c(\Delta)$, beyond which the spheres detach from the upper boundary, so that the compressive force there goes to zero, i.e.

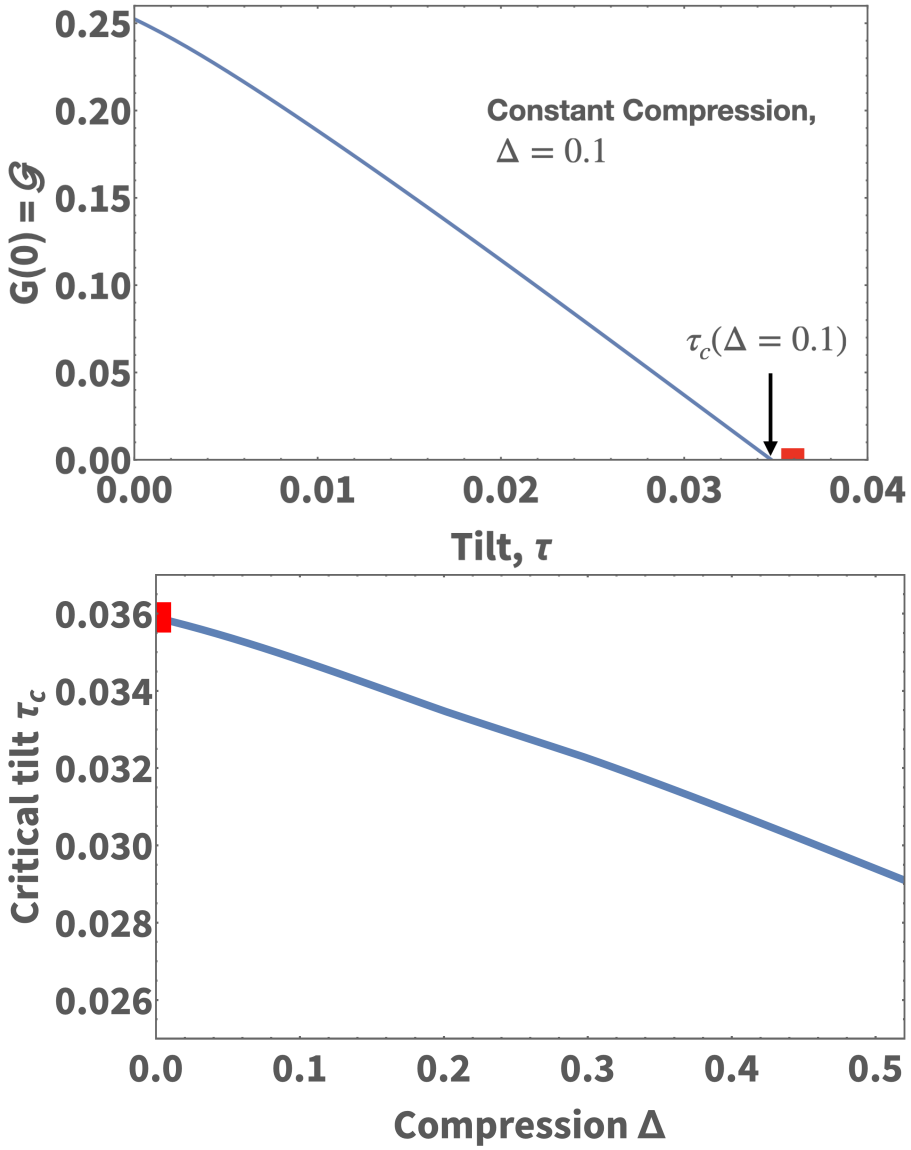

Figure 3.3: (a) Variation with tilt of the compressive force $\mathcal{G} = G(u = 0)$ at the "top end" of the chain, for compression $\Delta = 0.1$. Detachment of the chain corresponds to $\mathcal{G} = 0$, calculated numerically. (b) The variation of the critical value of tilt (where $\mathcal{G} = 0$) as a function of compression for the full numerical solutions of the continuum equation with $N = 10$. The red square point at $\Delta = 0$ corresponds to the analytic prediction made for the Whittaker equation.

$G(u=0) = \mathcal{G} = 0$.

As an example we show in Figure 3.3(a) the decrease of $G(0) = \mathcal{G}$ with tilt for constant compression $\Delta = 0.10$, as obtained from numerical solution of the full equation, Eqn (3.2) for $N = 10$. The critical tilt for detachment is determined as $\tau_c(0.1) = 0.0345$. Its variation with compression is shown in Figure 3.3(b); we will show below how the value of the critical tilt for the uncompressed system, $\Delta = 0$, is determined analytically using Whittaker functions.

We saw in Section 3.2.2 that for small ϕ the full equation can be approximated by a special case of the Whittaker equation, Eqn (3.7). For $\mathcal{G} = 0$ and the boundary condition $\phi(u=0) = 0$ and a given value of $\phi'(0)$ (which is chosen so to obtain a specified compression) its solution is given by

$$\phi(u) = \frac{\phi'(0)}{4i} M_{\frac{i}{4\tau},\frac{1}{2}}(4iu), \tag{3.12}$$

where M is the Whittaker function [52] and i is the unit imaginary number. (Here we have used the property of the Whittaker function, $\frac{d}{du} M_{\frac{i}{4\tau},\frac{1}{2}}(4iu)|_{u=0} = 4i$.) An example of this solution was shown in Fig 3.2(b).

The chosen value of tilt τ in Eqn(3.12) uniquely determines the distance between the zero of $\phi(u)$ at $u = 0$ and its first zero at a positive value of u. Rephrased in the context of this problem: for a given number N of spheres (requiring $\phi(N) = 0$ for our boundary conditions) there is a well-defined critical value of tilt, τ_c, for detachment (i.e. $G(u=0) = \mathcal{G} = 0$ at τ_c). This value can be determined (numerically) from Eqn (3.12); an upper bound estimate is given by $\tau_c < [3(N-2)]^{-1}$ (as shown in section 2.2.2).

For the case $N = 10$ the boundary conditions $\phi(0) = \phi(10) = 0$ are fulfilled for $\tau_c = 0.0359$. From Figure 3.3(b) we see that this is the critical value of tilt for detachment at compression $\Delta = 0$, i.e. $\tau_c(\Delta = 0) = 0.0359$. For higher values of compression, the value of tilt τ_c is reduced; see Figure 3.3.

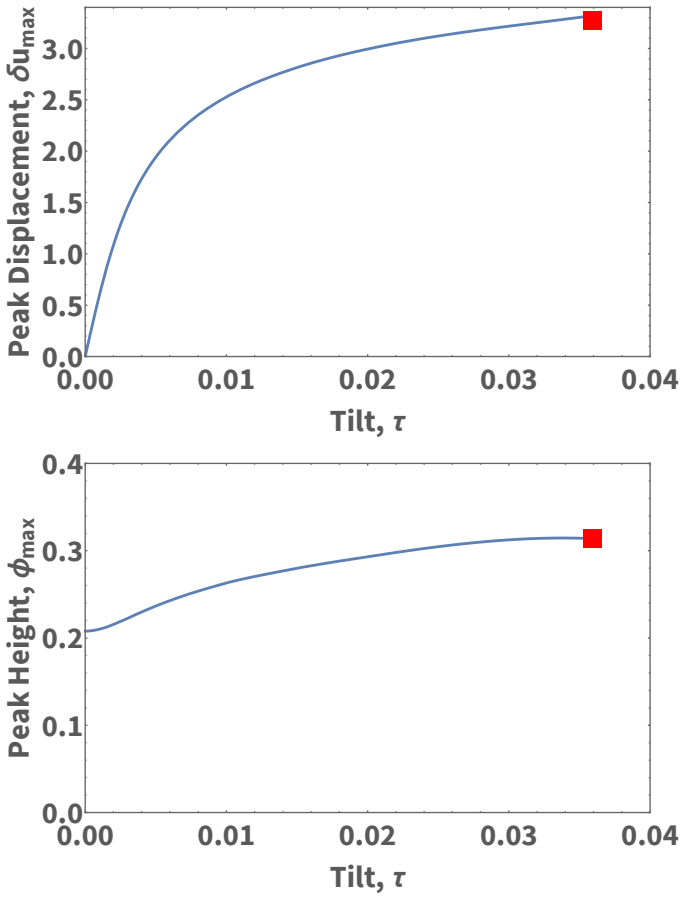

Figure 3.4: Results from numerical solutions of the full equation, Eqn (3.2), for the tilting of a chain under constant compression ($\Delta = 0.10$). (a) The introduction of tilt leads to a displacement, δu_{max}, of the peak position away from the centre. (For $N = 10$ as shown here: $\delta u_{max} = u_{max} - 5$.) (b) Variation of peak height with tilt. In each case the corresponding result of Whittaker theory is shown by a red square.

For values of tilt close to detachment, and for small values of compression, the Whittaker solution serves as an analytic approximation of the numerical solutions of the full equation. Figure 3.1(b) demonstrates this for the case of compression $\Delta = 0.1$.

The Whittaker solution also provides an estimate of both peak position and peak height at the point of detachment. Figure 3.4(a) shows numerical results for the displacement of the peak away from the centre as a function of tilt, at fixed compression $\Delta = 0.1$, as obtained from numerical solutions of the full equation, Eqn. 3.2. For small values of τ this is linear in τ. At the point of detachment the peak remains a finite distance away from the bottom wall. Shown as a red square in Figure 3.4(a) is the peak displacement of the Whittaker solution, Eqn (3.12), corresponding to the point of detachment.

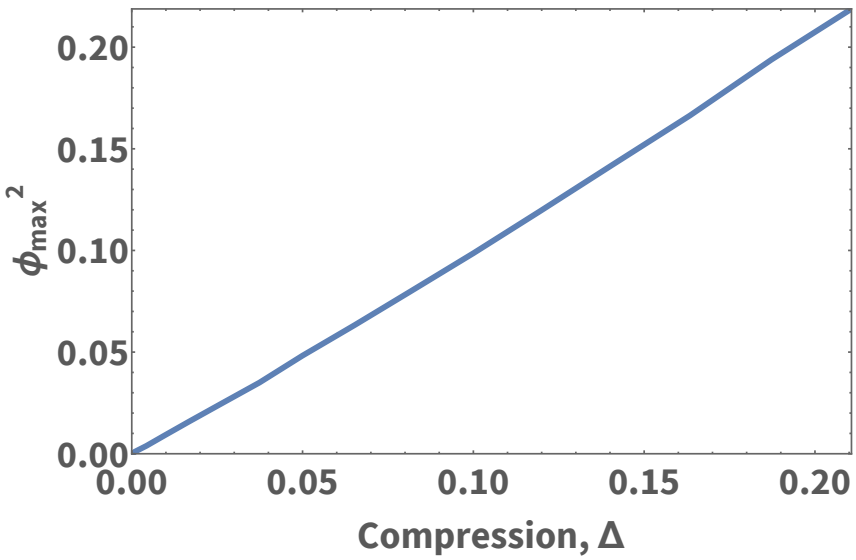

Figure 3.5: The peak height ϕ_{max} of the scaled Whittaker solutions, Eqn (3.12), varies approximately as $\phi_{max}^2 \simeq \Delta$. For small compression, Δ, this approximates the behaviour of the full solution near detachment.

The variation of peak height, ϕ_{max}, as a function of tilt for fixed compression is shown in Figure 3.4(b). This too converges to a finite value at the point of detachment, which is well approximated by the Whittaker solution for this compression. The peak height of a Whittaker profile scales as the square root of compression Δ, as shown in Figure 3.5.

3.3.3 Compression and tilt: Airy functions

The Airy function formulation is a generalisation of our previous approximations. We now no longer assume that tilt $\tau = 0$, instead we assume that the quantity $N\tau/\mathcal{G} \ll 1$. It provides the following approximate solution of the full equation, for a given value of τ:

$$\phi(x) = c_1 Ai(x) + c_2 Bi(x). \tag{3.13}$$

Here the variable x is given by

$$x = \left(\frac{\tau}{\mathcal{G}^2}\right)^{-2/3} \left[\frac{1}{\mathcal{G}}\left(1 - \frac{\tau u}{\mathcal{G}}\right) - 4\right], \tag{3.14}$$

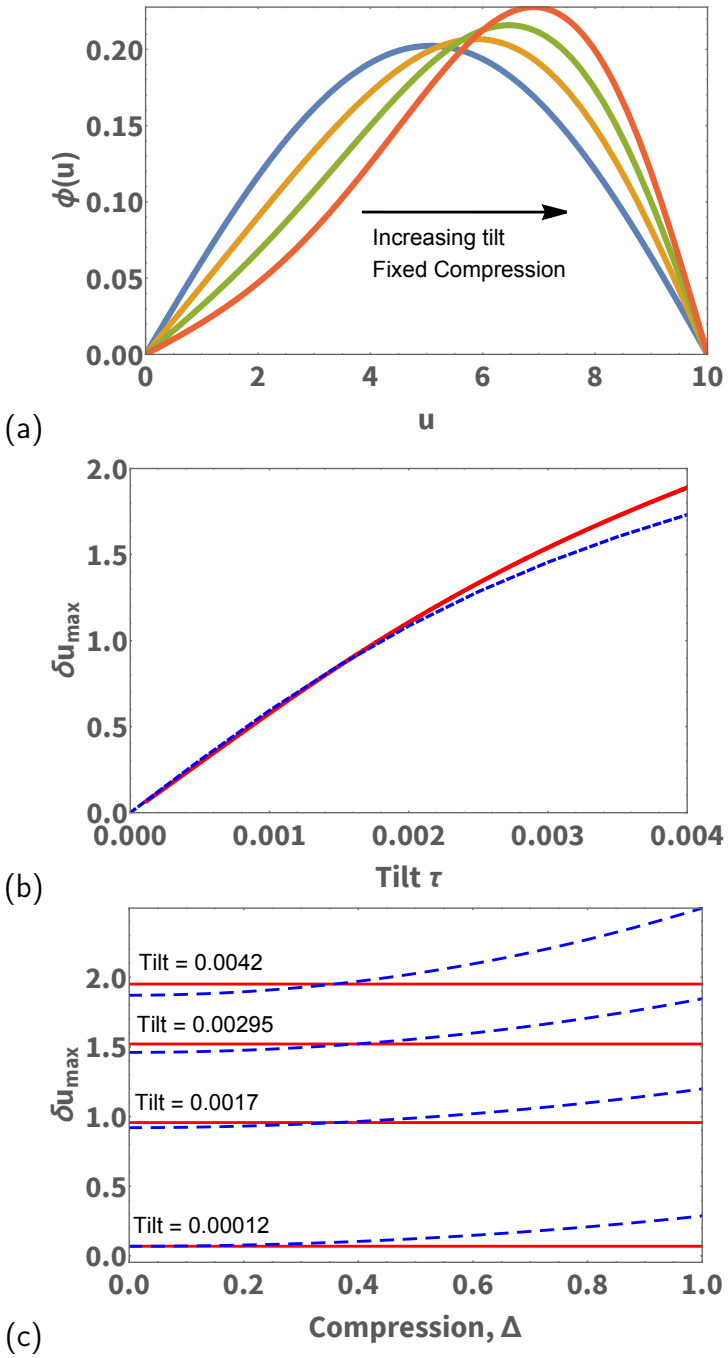

Figure 3.6: For small values of both tilt τ, and compression Δ, combinations of Airy *Ai* and *Bi* functions reproduce the key feature of solutions of the full continuum equation, namely displacement of the profile peak away from the centre, in response to the application of tilt. (a) Profiles for $\phi(u)$ in terms of Airy functions for fixed compression $\Delta = 0.1$ and varying tilt τ in the range $(0, 0.0045)$ (for $N = 10$). (b) Peak displacement δu_{max} (as in Figure 3.4(a)), as a function of tilt for $\Delta = 0.1$. Blue dashed line: result from the full equation, Eqn (3.2). Red solid line: Analytical result involving Airy functions. (c) Peak displacement as a function of compression for various values of tilt. Blue dashed line from full equation, red solid line: Airy solution.

and the constants c_1 and c_2 are determined from the boundary condition $\phi(0) = \phi(N) = 0$, see Appendix A3.3.

Figure 3.6(a) shows examples of profiles $\phi(u)$, obtained for a fixed values of compression, and several values of tilt. For small values of tilt τ the position of the maximum varies linearly with τ; see Figure 3.6(b). (The linear variation for small τ was already seen in the numerical solutions of the full equation; see Figure 3.4(a)).

Eqn (3.9) (of which Eqn (3.13) is an exact solution) is linear in ϕ, allowing for a simple scaling of its solutions to obtain profiles corresponding to different values of compression, Δ. The peak position is thus only dependent on tilt, but independent of compression. This is shown in Figure 3.6(c) where we contrast this behaviour with that of solutions of the full equation.

3.4 Phase diagram and energy

The results of our investigation can be presented in the form of a 'phase diagram' with axes tilt τ and compression Δ (here we borrow the thermodynamic term, characterising the regions in $\tau - \Delta$ space by the kind of structures that may be found there). The phases that we identified are the straight chain ($\tau_c(\Delta = 0)$), the buckled attached chain ($\mathcal{G} > 0$), and detached states. All these are marked up in Figure 3.7 for the case $N = 10$, together with an indication of the validity ranges of the various analytical solutions for the profiles $\phi(u)$.

Also indicated in the phase diagram is a straight line (corresponding to constant tilt, $\tau = 0.25$) leading from the point *a* (unbuckled tilted chain) to *b* (buckled chain, at the point of detachment). Knowledge of the compressive force $\mathcal{G}(\Delta)$ at the elevated end of the chain as a function of compression, Δ, allows for the computation of the energy difference between two states along that line using the work energy theorem,

$$E - E_S = \int_0^\Delta \mathcal{G}(\Delta) d\Delta. \tag{3.15}$$

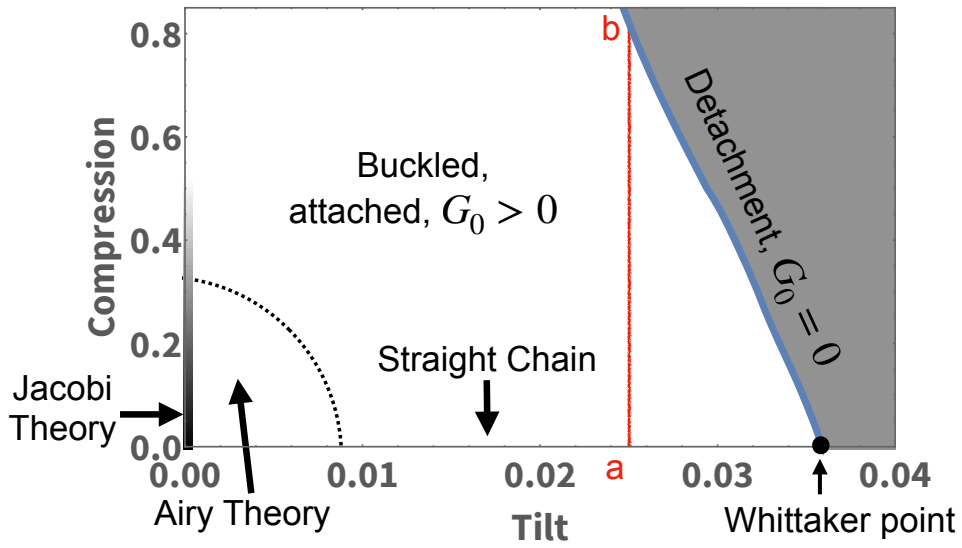

Figure 3.7: Phase diagram representing the results of the continuum model (for $N = 10$) in the plane of tilt τ and compression Δ. The solid blue line demarcates a phase boundary and is defined by $G(0) = \mathcal{G} = 0$, i.e. detachment at the elevated end of the chain of spheres. The area to the left of it corresponds to buckled structures, the area to its right to collapsed structures. In the case of compression $\Delta = 0$ (horizontal axis) the chain remains unbuckled up to the value of critical tilt $\tau(\Delta = 0) = 0.0359$ which is given by the Whittaker solution. Knowledge of $\mathcal{G}(\Delta)$ along a vertical line enables the calculation of the energy difference between any two states using the work energy theorem (for example between the points *a* and *b* indicated on the diagram).

Figure 3.8(a) shows that $\mathcal{G}$ decreases with compression and vanishes at $\Delta \simeq 0.795$ (for tilt $\tau = 0.025$), corresponding to detachment. Numerical integration of $\mathcal{G}(\Delta)$ using the work-energy theorem, Eqn (3.15) results in the energy difference $E - E_S$, as shown in Figure 3.8(b).

An alternative route to evaluate this energy difference is as follows. The total energy of a line of spheres has two contributions. Tilting the line away from the horizontal leads to a gravitational energy; it is given by $E_S = \tau N^2/2$, if the chain is straight. Buckling, i.e. sphere displacement in the transverse direction results in a second contribution, associated with the harmonic confining potential. This is analogous to the method used to calculate energy in the discrete system, Eqn (2.10).

An equivalent formulation for total energy can also be derived for the continuous

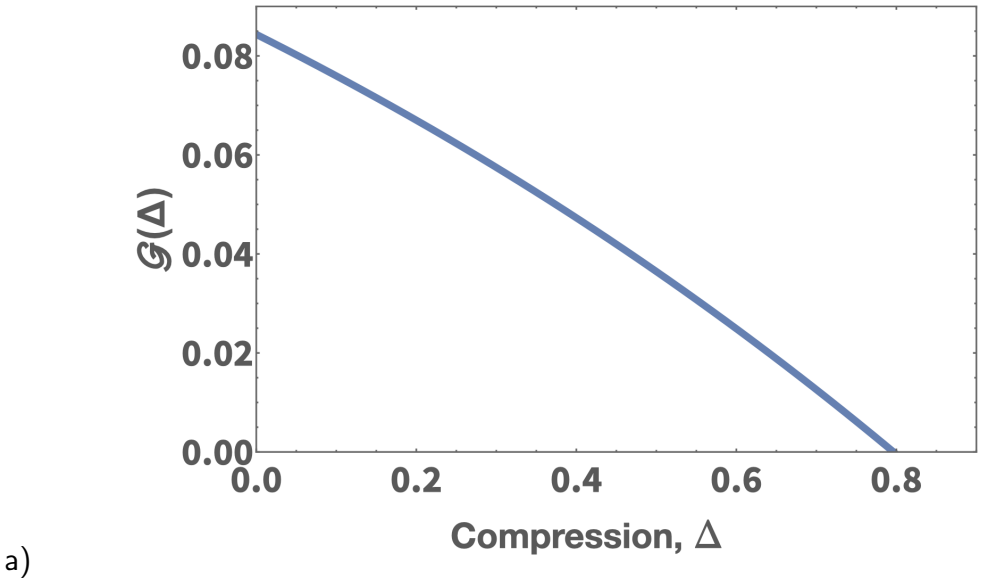

a)

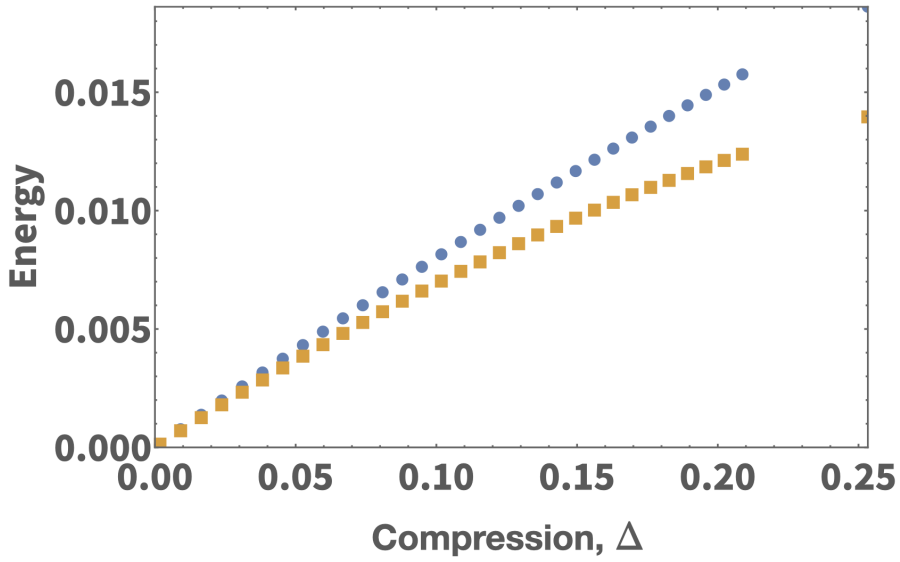

b)

Figure 3.8: (a) Variation of $\mathcal{G}$ with compression Δ, for constant tilt $\tau = 0.025$ (corresponding to the vertical red line on the phase diagram, Figure 3.7). Detachment occurs at the intersection with the horizontal axis, $\Delta = 0.795$. (b) Energy, relative to the energy of a tilted straight chain, as function of compression for fixed tilt $\tau = 0.025$. Dotted blue line: work-energy theorem, Eqn (3.15). For low values of ϕ the energy can also be expressed in the integral form of Eqn (3.16), see dashed yellow line.

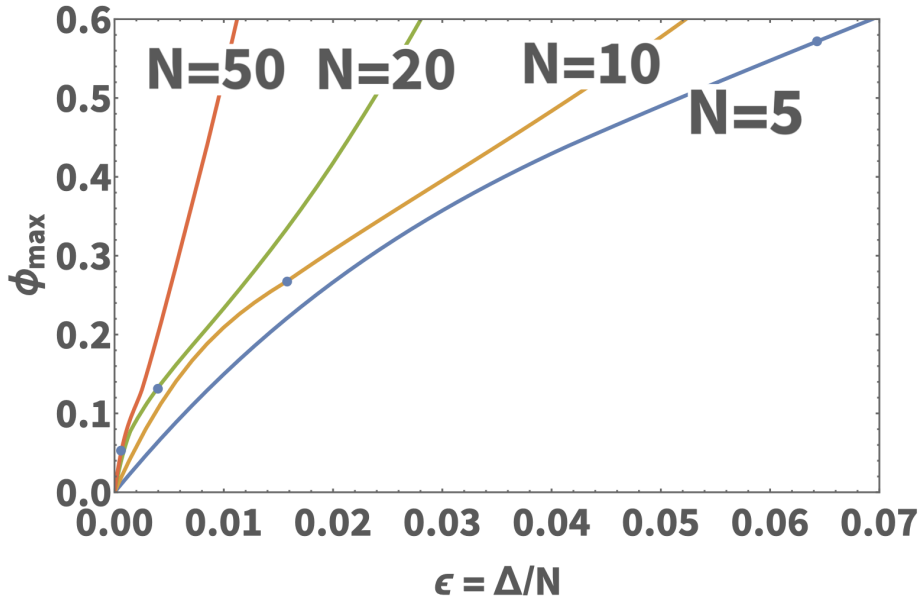

Figure 3.9: Variation of the peak height, ϕ_{max}, as a function of the compressive strain (Δ/N) for tilt $\tau = 0$. Shown are the curves for $N = 5, 10, 20, 50$. The points indicated by blue dots are the point at which the compressive force of the solution $\mathcal{G} = 0.25$ (see Appendix A1). Below this point, the variation of the peak height may be fitted with a square root function prior to this point, after it the variation is approximately linear.

formulation. This is shown in Appendix A3.1, leading to:

$$E \simeq \frac{1}{8}\int_0^N \frac{\phi^2(u)}{1+\phi^2(u)}du + \tau\left(\int_0^N \frac{udu}{\sqrt{1+\phi^2(u)}}\right) \simeq \frac{\Delta}{4} - \frac{\tau}{2}\int_0^N u\phi^2(u)du. \quad (3.16)$$

This equation allows for the direct computation of the energy from solutions $\phi(u)$ of the full continuum equation, Eqn 3.2. Figure 3.8(b) shows this formula replicates the linear increase in energy for low compression, i.e. solutions with small values of ϕ. See Figure 3.10.

3.5 Conclusions

The continuum model captures many of the fascinating details of this system, while providing an insight into its more obscure properties. The model provides transparent interpretations of the effects of localisation, N-dependence of quantities such as energy, and the effect of tilt on a system. Its analytic approximations allow us to lean

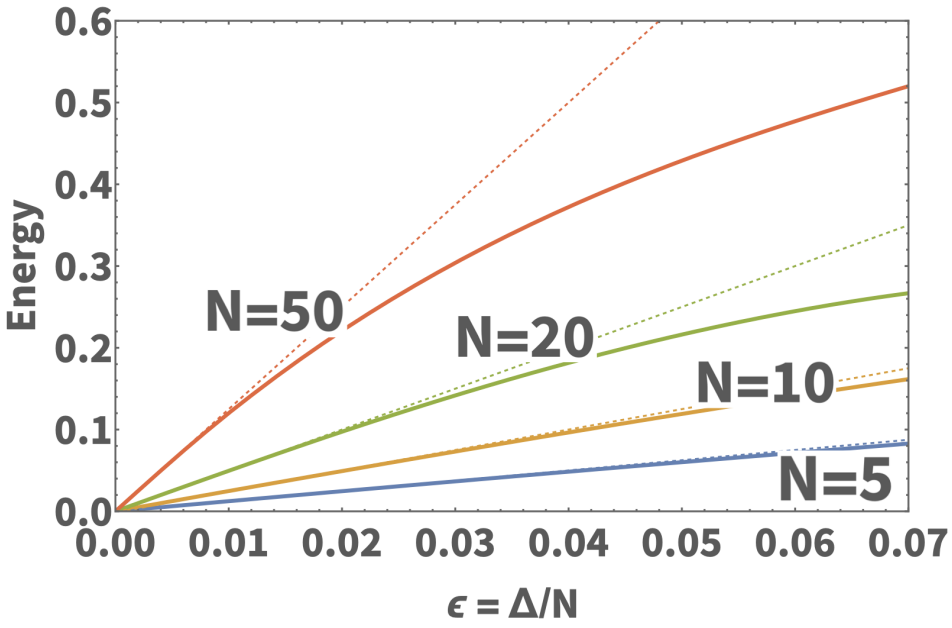

Figure 3.10: Variation of the energy as a function of compressive strain (Δ/N) for $N = 5, 10, 20, 50$, $\tau = 0$, as calculated from Eq (3.16). The dashed lines represent the leading term of $\Delta/4$ given in Eq (3.16), demonstrating the efficacy of this approximation when compressive strain (and thus ϕ_{max}) is small.

on established mathematical work to interpret these effects.

Our interpretation may be extended to experimental systems, such as the evolution of ion crystals in linear traps (see Section 1.1). It has already been shown that the optical and conductance properties is important depend heavily on the arrangement of these structures [4]. Our simplified approach may be used as a baseline model for characterising the change in structure as the confining potential of the trap is weakened.

The approach, however, is limited by its breakdown at large buckling amplitude, which entails transitions to the doublet state, where second-neighbour contacts arise. Through other simulation methods, we are also aware of a dearth of other possible solutions (see Chapter 2), however the continuum model may only access the 'ground state' structures: the symmetric structures in the case of no tilt, and the single-peak tilted structures when $\tau > 0$. One may envisage an extension of the continuum model to include such structures, however it would require reworking the original iterative equations proposed in Chapter 2.

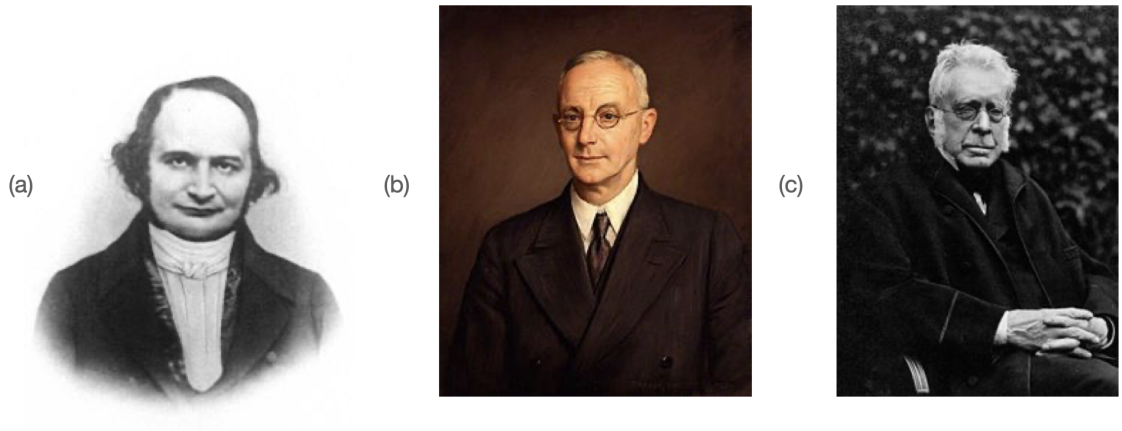

Figure 3.11: Portraits of the three mathematicians whose work was discussed in this chapter. (a) Carl Gustav Jacob Jacobi (1804-1851), a German mathematician most famous for the development of his 'elliptic functions', which find applications in the cases of the pendulum, the Euler top and the Kepler problem. Here they find a new use in describing the buckling profiles in the absence of tilt. We shall discuss these in more detail in the next chapter. (b) Edmund Taylor Whittaker (1873-1956), an English mathematician known for his work in mathematical physics and numerical analysis. He is the eponym of the Whittaker function, which we discussed in this chapter. He also has an Irish connection, having served as the Andrews Professor of Astronomy and the Royal Irish Astronomer in Trinity College Dublin (1906-1912). (c) George Biddell Airy (1801-1892), an English mathematician and astronomer famous for his work in planetary dynamics and optics. We apply his Airy functions to our problem of a buckled line of spheres under the action of compression and tilt. (Portraits and biographical details are taken from Wikipedia: `https://www.wikipedia.org`)

In the next chapter, we will explore the approximation of Eqn (3.2) in the case of $\tau = 0$. This relates the continuum approach to the Jacobi equation, and its solutions to the Jacobi elliptic functions. This approach gives a greater insight into the effects of localisation and N-dependence for the case of the system under compression.

4 Jacobi elliptic functions

Here we extend the analysis of the previous section, and provide a thorough exploration of the role of Jacobi elliptic functions in describing the angle profiles of our buckled structure. As we discussed in Section 1.1, Jacobi elliptic functions already feature in the problem of elastic Euler buckling, making their appearance here worthy of further investigation.

4.1 The 'reduced equation' and Jacobi functions

Results obtained for the continuous formulation are a good approximation to those of the original discrete problem, except at the limit of high compression Δ, and are readily analyzed, which providing a "bird's eye view" of solutions, for all N and Δ.

We may rewrite the key differential equation, Eqn (3.2), in terms of the angle profile $\theta(u)$ (remembering that $\phi(u) = \tan\theta(u)$),

$$\frac{d^2 \tan\theta(u)}{du^2} + 4\left(\tan\theta(u) - \left(1 + \frac{\kappa^2}{4}\right)\sin\theta(u)\right) = 0. \tag{4.1}$$

In the following the compressive force $\mathcal{G}$ exerted at both ends of the chain is represented by the quantity κ^2, which is defined as

$$\kappa^2 = \mathcal{G}^{-1} - 4. \tag{4.2}$$

It may be positive or negative, so that the square root κ may be real or imaginary.

Again, we will limit our discussion to properties of solutions of Eqn (4.1) for the hard wall boundary conditions ($\theta(u) = 0$ at the two end points of the chain, at $u = 0$ and $u = N$) which are imposed on our present experiments and discrete calculations.

By substituting $\phi = \tan\theta$ and neglecting terms of order $\mathcal{O}(\phi^5)$, Eqn (4.1) may be reduced (see Appendix A3.1) to arrive at the following nonlinear differential equation which we may call the *reduced equation*,

$$\phi'' = \kappa^2\phi - 2\left(1 + \frac{\kappa^2}{4}\right)\phi^3. \tag{4.3}$$

In Section 4.4 we show that its analytical solutions compare well with numerical solutions of the full equation, Eqn (4.1), for sufficiently small values of compression. (This is also the case for solutions of $\theta'' = \kappa^2\theta - 2\theta^3$, the reduced equation that we had originally formulated [34].)

The reduced equation is one form of the Duffing equation [50], well known in the theory of oscillations, where it serves as an analytically tractable approximation to a wide range of dynamical systems including the non-linear pendulum, the forced oscillations of beams and cables, as well as non-linear electrical circuits. In its most general form the Duffing equation is given by

$$\ddot{x}(t) = -\delta\dot{x} - \beta x - \alpha x^3 + \gamma\cos(\omega t),$$

in the absence of both a damping term ($\delta = 0$) and a driving force ($\gamma = 0$) it can be seen that the Duffing equation is equivalent to Eqn (4.3). The character of the phenomena described by the Duffing equation depends on the non-linear term $-\beta x - \alpha x^3$. For $\beta > 0$ it describes an oscillator with a non-linear restoring force, while for $\beta < 0$ it describes the dynamics of a point mass in a double well potential. In our case this cross-over is governed by the value of κ^2, as we shall show in the following section by plotting the phase portraits of both the full and reduced equations (i.e. Eqn (4.1) and Eqn (4.3), respectively).

While much of the analysis of the Duffing equation is directed towards understanding dynamic properties, the present problem of a chain of hard spheres in a transverse potential represents a realisation of the Duffing equation in a static system. It is well recognised that the solutions of the Duffing equation are in terms of scaled Jacobi functions, these functions are also an excellent approximations to the full differential equation Eqn (4.1).

4.1.1 Properties of the reduced equation

Many of the general properties of the full equation, Eqn (4.1), and its reduced form, Eqn (4.3), are obvious and well illustrated by their phase portraits shown in Figure 4.1. These include symmetry under $\theta \to -\theta$ and $u \to -u$, periodicity (with an exception noted below) and the dependence on the sign of κ^2. The key feature that can be seen in the phase portraits as κ^2 goes from $\kappa^2 < 0$ to $\kappa^2 > 0$ is the transition from a system with one stationary point to a system with two stationary points (the case of $\kappa^2 = 0$ is intermediate between these two regimes).

For $\kappa^2 > 0$ the solution of the reduced equation has inflection points ($\phi'' = 0$) wherever

$$\phi = 0, \quad \text{or} \quad \pm\sqrt{\frac{\kappa^2}{2(1+\kappa^2/4)}}. \tag{4.4}$$

(In our case, θ (and thus ϕ) is always positive.) For $\kappa^2 < 0$ the second type of inflection point does not arise.

For the hard wall boundary conditions applied here, the solutions are symmetric about the midpoint of the system. It is clear therefore that for $\kappa^2 < 0$, the relevant solution is "cosine-like" (see Section 4.3, Figure 4.4, example G).

For $\kappa^2 > 0$ the solution develops a more or less prominent peak at the centre (localization of buckling), see Figure 4.4, example C). This type of solution may extend to infinity with exponential tails, $\theta \sim \exp(\pm\kappa u)$, if the separation of the hard walls is taken to the infinite limit.

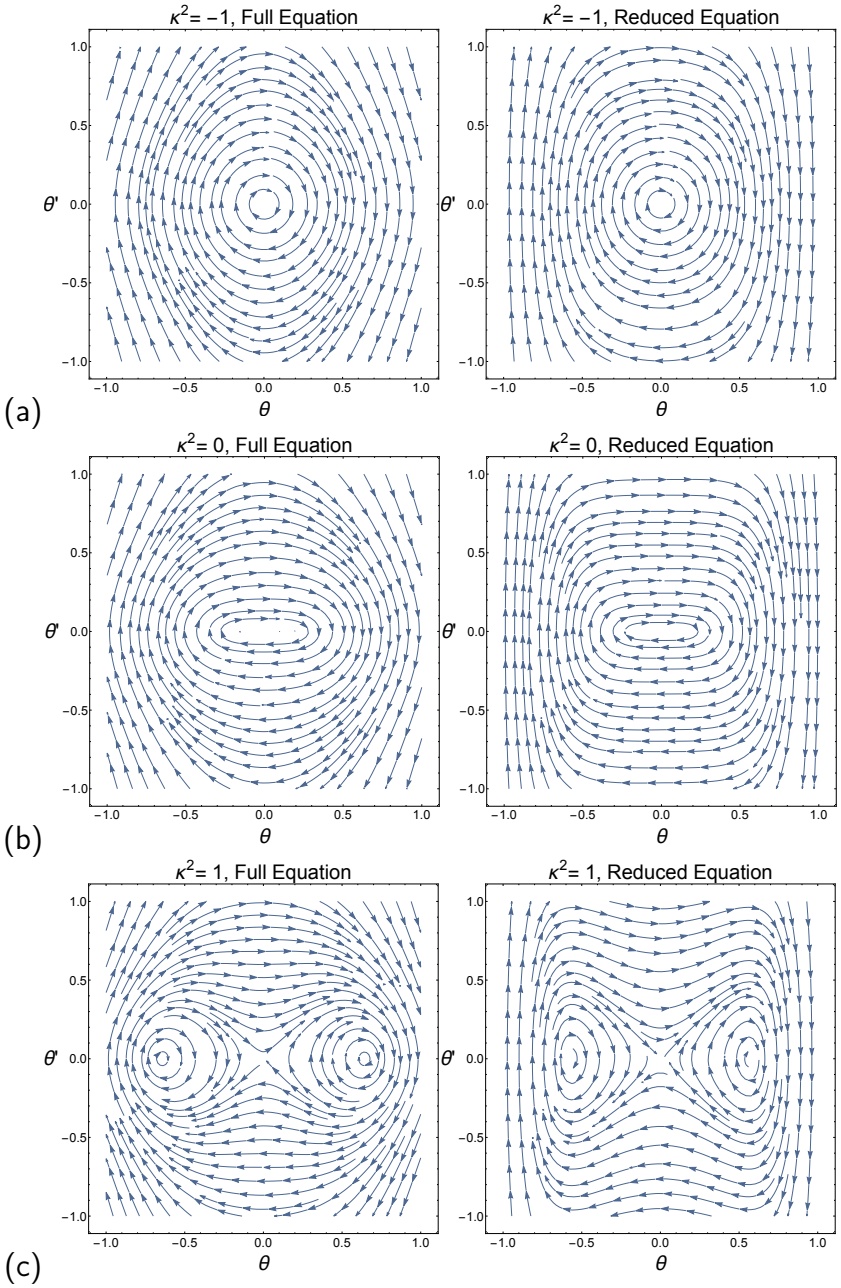

Figure 4.1: Phase portraits for both full equation Eqn (4.1) (left) and reduced equation, Eqn (4.3) (right). (a) For $\kappa^2 < 0$ the trajectory orbits the stationary point at (0,0), shown also for $\kappa^2 = 0$ in (b). For $\kappa^2 > 0$ (c) the trajectory may orbit either one or both of the two stationary points at $\left(\arctan\left(\pm\sqrt{\frac{\kappa^2}{2(1+\kappa^2/4)}}\right), 0\right)$, depending on the boundary conditions.

The intermediate case $\kappa = 0$ has solutions with second, third, and fourth derivatives at the two edges, so that it takes a roughly triangular form (see Figure 4.4, example E). In this case the following approximate relationship holds, $\Delta \approx \frac{4}{3}N^{-1}$, where compression Δ is computed using the expression given below (Eqn (4.5)).

4.2 Jacobi functions

While not entirely elementary the reduced equation does have *analytic* solutions in the form of Jacobi functions. The solutions which are categorized in the following are for the boundary condition $\theta(0) = \theta(N) = 0$ (and thus $\phi(0) = \phi(N) = 0$), thus requiring a Jacobi function with real zeroes.

As an example, Fig 4.2 shows both the numerical solution of the full differential equation and the analytical solution of the reduced equation (i.e. where $\tan\theta$ is a rescaled Jacobi *cn* function, to be derived below) corresponding to the calculation for the discrete case as discussed in Chapter 2.

In the continuum formulation compression Δ is given by the integral

$$\Delta = \int_0^N (1 - \cos\theta(u))\, du, \tag{4.5}$$

where the integration has generally to be performed numerically for given $\theta(u)$.

The reduced equation, Eqn (4.3), is only an approximation to the full one, but offers many opportunities to develop the mathematics of its solutions, including bringing the Jacobi functions into play. In doing so, we shall here restrict the analysis to the case of hard wall boundary conditions with walls perpendicular to the axis: the treatment of other boundary conditions entails the introduction of further Jacobi functions.

4.2.1 Notation for Jacobi functions

There are twelve different Jacobian elliptic functions whose primary definition is framed in terms of the inversion of integrals. These functions are solutions of first and second

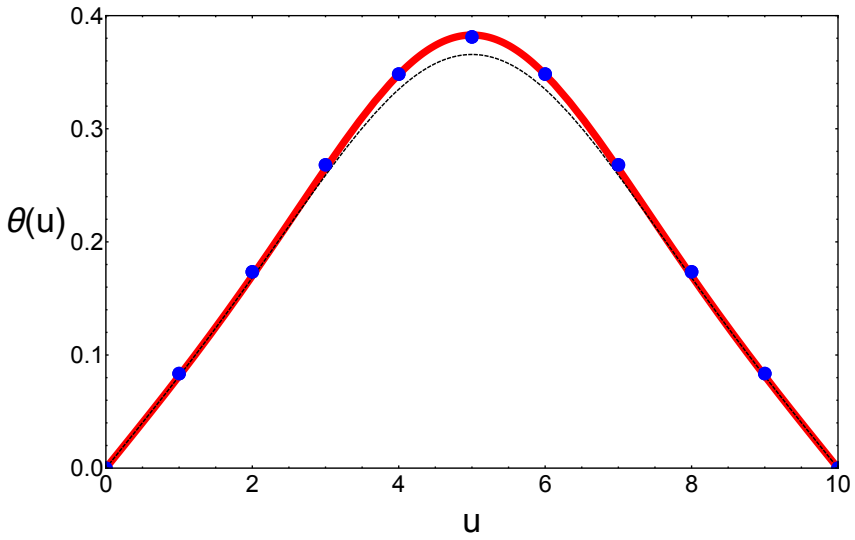

Figure 4.2: Results for the continuum model applied to a system of ten spheres with a compressive force $\mathcal{G} = 0.2435$ (corresponding to $\kappa^2 = 0.1068$, Eq (4.2)). The solid line is an accurate numerical solution for $\theta(u)$ for the full continuum differential equation Eq (3.2) under the same conditions. The dashed line is the analytical solution $\theta = \arctan\phi$ of the reduced equation, Eq (4.3), where ϕ is the scaled Jacobi *cn* solution, Eq (4.7), discussed in Section 4.2.2. Compression Δ is computed using Eqn (4.5). Also shown are the data points for the corresponding discrete system.

order differential equations and it will be this aspect which concerns us here.

Only four Jacobi functions satisfy differential equations which may be transformed into the reduced equation, Eqn (4.3). These functions may be rescaled, as detailed below, to give explicit analytic solutions of the equation. However, our present restriction to hard wall ($\theta = 0$) boundary conditions further reduces the available function types to two, which have zeroes. These are *cn* and *sd*, but these are related by a translation (like the *sin* and *cos* functions), so that only one of them is required: we choose *cn*.

There is a one-parameter set of *cn* functions, each being generally denoted by $cn(x|m)$, and the individual function is identified by m, where $\sqrt{m}$ is called the modulus. It is real for our purposes. The parameter m is related to the period of the Jacobi functions, which is stated in terms of the complete elliptic integral of the first kind; see Section 4.2.2.

By convention, m is restricted to the range $0 < m < 1$. Elliptic functions with a value

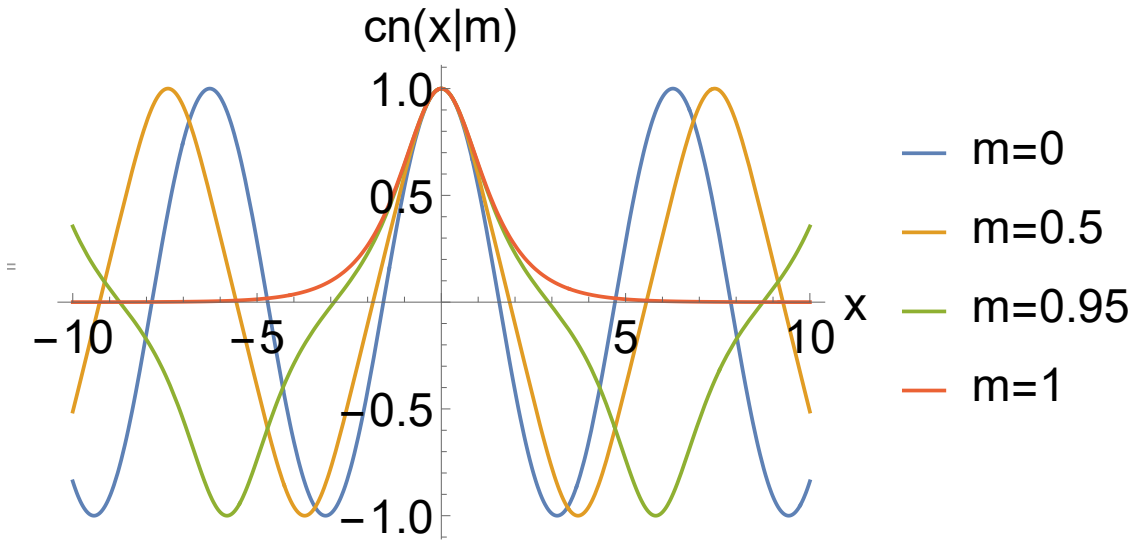

Figure 4.3: Examples of the Jacobi function $cn(x, m)$ for different values of the modulus $m^{1/2}$. Their shape varies smoothly between cos(x) (for m=0) and the hyperbolic secant, $\mathrm{sech}(x) = \frac{2}{e^x + e^{-x}}$ (for $m = 1$).

of m outside this range can be rewritten as other elliptic functions where m lies between 0 and 1. Hence the set of functions used here is that of $cn(x, m)$ for this range.

4.2.2 Jacobi function solution of the reduced equation

The Jacobi $cn(x|m)$ function is a periodic even function with zeroes, and a maximum of 1 at $x = 0$, see Figure 4.3. Its (real) period is $4K(m)$, where $K(m)$ is the complete elliptic integral of the first kind.

For the range $0 < m < 1$ the function $y(x) = cn(x|m)$ satisfies the differential equation

$$y'' = -(1 - 2m)y - 2my^3. \tag{4.6}$$

which is to be compared with the reduced equation. Matching the two forms, Eqns (4.6) and our reduced equation (4.3), it is easily shown (see Appendix A4) that a solution of Eqn (4.3) for given κ^2 (with $\kappa^2 > -4$ for finite positive compressive force $\mathcal{G}$) and satisfying the hard wall boundary conditions may be written as a *scaled* Jacobi *cn* function,

$$\phi(u) = \tan\theta(u) = \phi_{max}\ \mathrm{cn}(\sqrt{\kappa^2/(2m-1)}u|m), \tag{4.7}$$

The peak value ϕ_{max} of the variable ϕ (at $u = 0$) is given by

$$\phi_{max} = \sqrt{\frac{m}{(1+\kappa^2/4)(2m-1)}\kappa^2} \text{ for } 0 < m \leq 1. \tag{4.8}$$

The peak value of the corresponding angle variable θ (at $u = 0$) is

$$\theta_{max} = \arctan \phi_{max}. \tag{4.9}$$

For ϕ_{max} (and thus θ_{max}) to be real, real values for κ (i.e. $\kappa^2 > 0$) require $m > 1/2$, while imaginary κ (i.e. $\kappa^2 < 0$) requires $m < 1/2$, with $\kappa = 0$ for $m = 1/2$. This defines the solution space that we will explore in section 4.3, see Fig. 4.4.

As with other special functions, $cn(x|m)$ (and thus $\theta(u)$ (Eqn 4.7)) is readily called up from, for example, Mathematica [53], as is the complete elliptic integral of the first kind $K(m)$. Examples were already shown in Figs. 4.2 and 4.3.; several more will be shown in what follows.

For $m = 1$ and $m = 0$ the Jacobi functions simplify to more familiar forms, that is, $cn(x|1) = \operatorname{sech} x$ and $cn(x|0) = \cos x$, respectively. For $m = 1$ the solution, i.e. the scaled Jacobi function $\phi(u)$, is given by $\phi(u) = \sqrt{\kappa^2/(1+\kappa^2/4)}\operatorname{sech}\left(\sqrt{\kappa^2}u\right)$, for $\kappa^2 > 0$. In the limit $m \to 0$ (with $\kappa^2 < 0$) the solution $\phi(u)$ asymptotes to $\cos(\sqrt{-\kappa^2}u)$ with a prefactor asymptoting to zero ($\phi(u) \to 0 \times \sqrt{-\kappa^2/(1+\kappa^2/4)}\ \cos(\sqrt{\kappa^2}u)$). For the special case of $m = \frac{1}{2}$ we have $\phi(u) = cn\left(\sqrt{2}u|\frac{1}{2}\right)$ (see Appendix A4).

In the continuum representation N is half the period of the scaled Jacobi function, Eq (4.7) (for the rescaled variable $u = x\sqrt{(2m-1)/\kappa^2}$), and thus given by

$$N = 2K(m)\sqrt{\frac{2m-1}{\kappa^2}}, \tag{4.10}$$

where $K(m)$ is the complete elliptic integral of the first kind. For the case $N \to \infty$ ($\kappa^2 \to 0$, $m \neq 1/2$) the solution asymptotes to zero in the limits $u \to \pm\infty$.

In later sections we shall examine the variety of these solutions for hard wall boundary conditions, an arbitrary number N of spheres and an arbitrary value of compression Δ, which are the parameters defining a typical experimental measurement.

4.3 Solution diagrams

The solution space is rich in details, but the many parameters involved make it difficult to comprehend. The graphical method introduced here offers a transparent way to explore it.

Every solution for the specified boundary condition ($\phi, \theta = 0$ at the end points, for N spheres) must satisfy the reduced equation for some value of κ^2 (corresponding to the compressive force) and, from the above, can be expressed as an appropriately scaled Jacobi *cn* function, Eq (4.7), with squared modulus m. We will use the parameters, m and κ^2, to label all of the solutions which they uniquely define when subjected to scaling. This leads us to construct "solution diagrams", with every solution (for the stated boundary conditions) represented by a point. We have found it convenient to use a nonlinear scale for κ^2 for graphical purposes, so that all values of κ^2 are captured on the diagrams. Hence, instead of κ^2, we use

$$\hat{\kappa}^2 = \kappa^2/(1 + |\kappa^2|) \tag{4.11}$$

when making these plots.

The form of such a diagram is shown in Figure 4.4. This $\kappa^2 - m$ plane will be our "playing field" in describing all of the different forms of solutions that can arise, and their variation.

The requirement of having a real value for θ_{max}, Eq (4.9), leads to the identification of forbidden regions, i.e. areas in the $\kappa^2 - m$ plane for which no solutions exist (see section 4.2.2). Furthermore, the maximum angle θ_{max}, Eq (4.9), is basis of Figure 4.5. In the original discrete system [34, 43] this never exceeds $\pi/2$ because additional contacts are

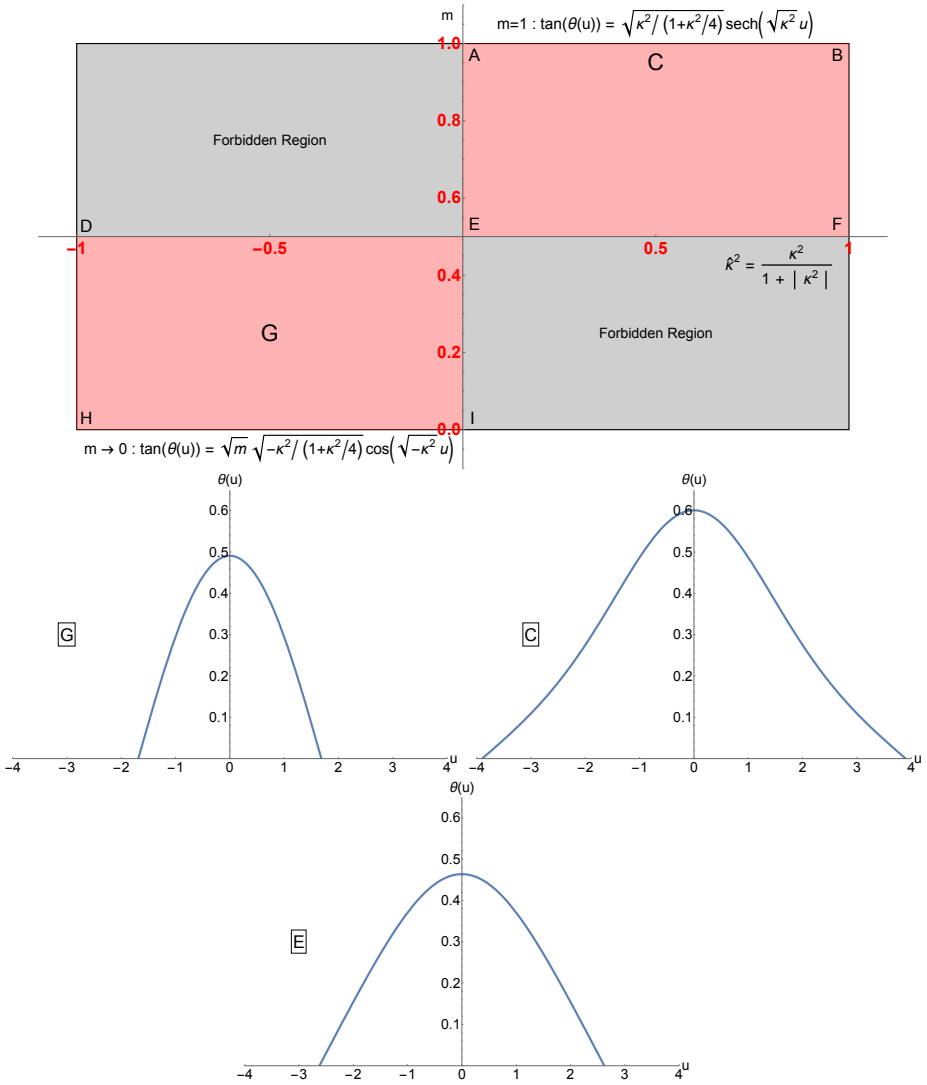

Figure 4.4: Jacobi *cn* functions can be scaled to give solutions $\theta(u)$ (Eq (4.7)) of the reduced equation, Eq (4.3), between two values of u at which the boundary condition is $\theta = 0$. These solutions are qualitatively different in the two pink domains indicated in the $\kappa^2 - m$ "solution diagram", where $m^{1/2}$ is the modulus of the Jacobi function ($\hat{\kappa}$ is defined by Eqn (4.11)). Typical profiles are shown for the points G, (-1/2, 1/4), and C, (1/2, 0.95). Solutions at the boundaries have the following properties, A-B: θ_{max} is finite and N infinite, except at the limits; θ_{max} is zero and N is infinite at A. The intermediate solution at E, (0, 0.5), is given by the scaled Jacobi *cn* function of roughly triangular form, $cn(\sqrt{2}u|1/2)$. At F, (1/2,1), the amplitude diverges while the period is zero.

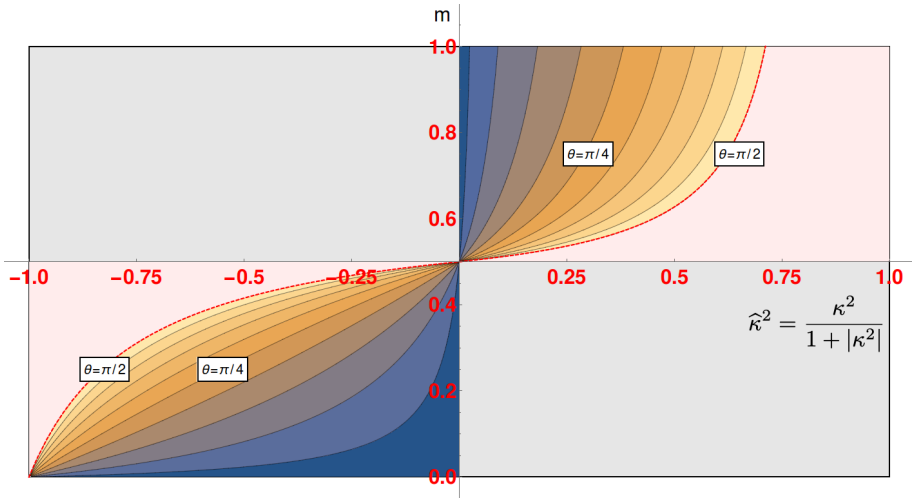

Figure 4.5: Contours of constant maximum angle θ_{max}, Eq (4.9). The dashed red contour corresponds to $\theta_{max} = \pi/2$ (as given by Eq (4.12)), the region beyond this contour cannot be realised in an experiment, but arises in the continuum formulation. For $m = 1$ and $\kappa^2 \geq 0$ one obtains $\theta_{max} = \kappa$.

formed beyond the limit of the theory. However, although there is no such limitation inherent in the continuum formulation, nevertheless the contour defined by

$$\frac{mk^2}{2m-1} = \frac{\pi^2}{4} \tag{4.12}$$

is to be regarded as representing the boundary beyond which the continuum model is unphysical, and indeed it is not a good representation of the discrete system for somewhat lower values of θ_{max}. As such we cut off all solution diagrams beyond this contour as indicated by a dashed red line. For further discussion see Section 4.4.

Figure 4.4 shows sample solutions for both negative and positive values of κ^2, together with the only solution at $\kappa^2 = 0$. Special forms (solution or absence of any finite solution) are to be found on the various boundaries of the allowed regions.

As anticipated in Section 4.1.1, the solutions are qualitatively different in the two allowed regions, as exemplified by those associated with the points G (for $\kappa^2 < 0$) and C (for $\kappa^2 > 0$). The first type has no inflection points, while the second has inflection points (at $\theta = \arctan\sqrt{\kappa^2/2}$), giving rise to a localized peak.

In Figure 4.6 we show how the number of spheres N varies with m and κ^2, by plotting

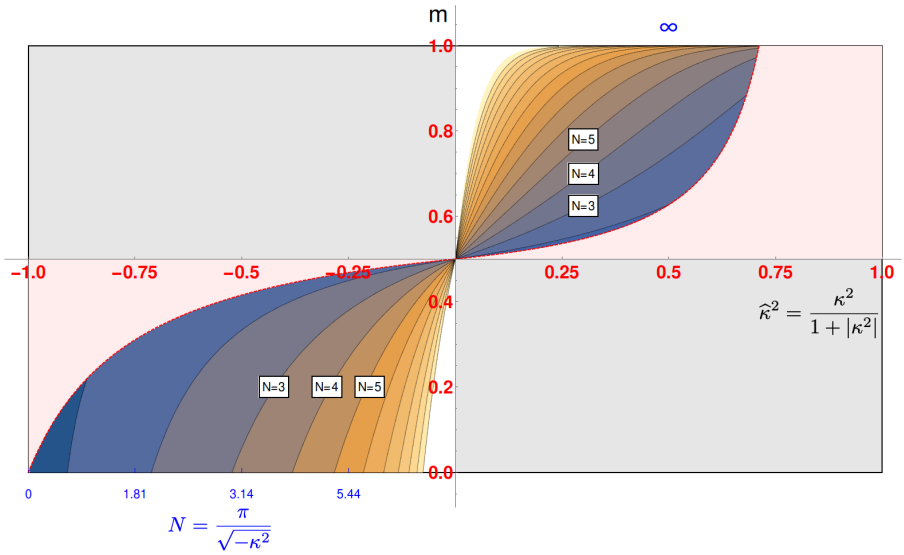

Figure 4.6: Contours of constant number of spheres N, up to N=15. All contours pass through the point $\kappa^2 = 0, m = 1/2$. In the limit $N \to \infty$, the contours coincide with the vertical axis, i.e. $\kappa^2 = 0$ (c.f. Eqn (4.10)). The dashed red curve corresponds to the contour $\theta_{max} = \pi/2$ beyond which the model is unphysical. In the limit $m \to 1$ we find $N \to \infty$ and for $m \to 0$ we have $N \to \frac{\pi}{\sqrt{-\kappa^2}}$, these limits are indicated in blue on the diagram along with some computed values.

contours of N using Eqn (4.10). (The dependence of N (periodicity) on the values for κ^2 and m is also visible in the examples of Figure 4.4.) All of the contours pass through the point $m = 1/2$, $\kappa^2 = 0$, so that the function $cn(x|m)$ can be scaled to provide a solution for κ^2 and any N. The contours asymptote to the m axis as $N \to \infty$.

Figure 4.7 shows the variation of compression Δ, computed using Eqn (4.5) using contours. These intersect the line $m = 1$.

An appropriate characteristic of a solution is its degree of localization. This may be defined by

$$D(m, \kappa^2) = \left(\int_{-N/2}^{+N/2} \theta(u) du \right)^2 \Big/ \left(N \int_{-N/2}^{+N/2} \theta^2(u) du \right), \qquad (4.13)$$

with N given by Eqn (4.10),

This participation ratio, used for example in the treatment of Anderson localisation in solid state theory [54], answers the question: roughly speaking, over what proportion of the spheres is buckling concentrated?

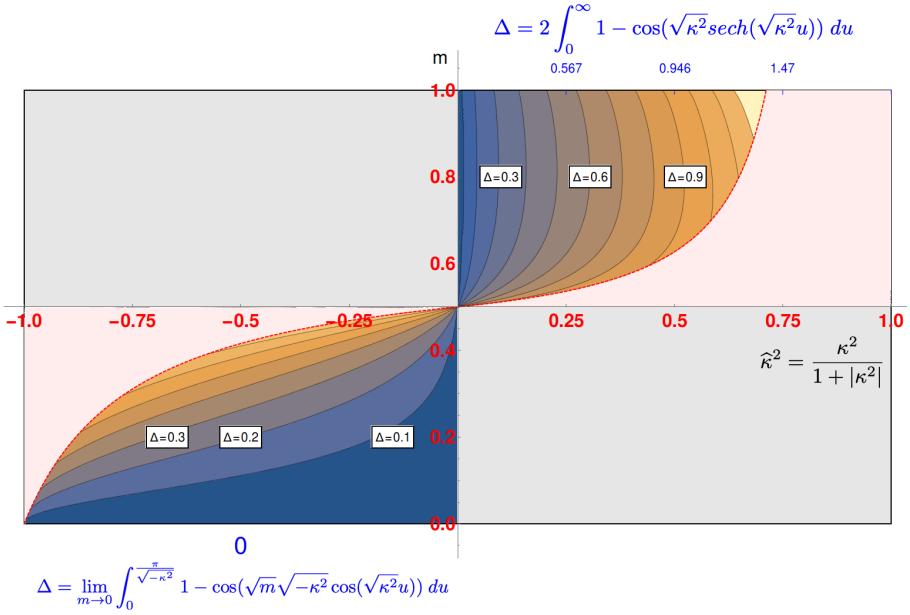

Figure 4.7: Contours of constant compression Δ. The dashed red curve corresponds to the contour $\theta_{max} = \pi/2$ beyond which the model is unphysical. In the case of the limit of $m \to 0$ the compression is found to be zero, while in the case of $m \to 1$ the compression is given by an integral which can only be computed numerically and we have indicated some of these values in blue.

We may express $D(m, \kappa^2)$ in terms of the scaled Jacobi *cn* solutions, $\phi = \tan\theta$ (Eqn (4.7)) as

$$D(m,\kappa^2) = D_\phi(m)\left[1 - \frac{\kappa^2/3}{(2m-1)}\left(\frac{\sqrt{m(m-1)}}{\arcsin\sqrt{m}} + 2m - 1\right)\right], \tag{4.14}$$

correct to order ϕ^3.

The participation ratio D_ϕ for the scaled Jacobi functions, defined as $D_\phi = \left(\int_{-N/2}^{+N/2}\phi(u)du\right)^2 / \left(N\int_{-N/2}^{+N/2}\phi^2(u)du\right)$, can be computed analytically, and depends only on the value of m,

$$D_\phi(m) = \frac{\arcsin^2\sqrt{m}}{K(m)\left(E(m) + (m-1)K(m)\right)}. \tag{4.15}$$

Here $K(m)$ and $E(m)$ are the complete elliptic integrals of the first and second kind, respectively. The limiting values of $D(m, \kappa^2)$ are $D(0, \kappa^2) \simeq 0.8105$ and $D(1, \kappa^2) = 0$. The case $m = 1/2$ requires $\kappa^2 = 0$, with $D(1/2, 0) \simeq 0.7854$. The participation ratio as a function of m is shown in Figure 4.8.

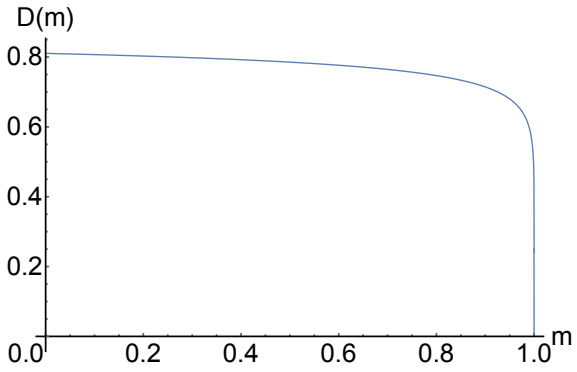

Figure 4.8: Localization measure ("participation ratio") $D(m)$ as a function of the square of the modulus of the scaled Jacobi *cn* function (Eqn (4.15)).

A further measure of localization which can be expressed analytically also for the case of the full differential equation, Eqn (4.1), is examined in the next Section.

4.4 Accuracy of the reduced equation

The previous sections described analytical solutions of the reduced equation, Eqn (4.3), in terms of scaled Jacobi functions. Here we will introduce a quantitative measure to assess how well the reduced equation approximates the full equation, Eqn(4.1). This involves the introduction of an alternative measure of localization, in terms of a *peak width* w_p, which can be expressed analytically for both equations.

A peak width w_p may be defined as

$$w_p = 2\sqrt{\frac{2\theta_{max}}{-\theta''(\theta_{max})}}, \tag{4.16}$$

where θ_{max} is the peak, and thus $\theta''(\theta_{max}) < 0$. (The quantity w_p simply corresponds to the distance between the two zeros of an inverted parabola with maximum θ_{max} at $u = 0$.) The merit of this definition lies in providing an analytical expression for comparing solutions of the full equation to those of the reduced equation.

From the full equation, Eqn (4.1), we obtain

$$w_{p,full} = \sqrt{2\theta_{max}}\left(\tan\theta_{max} - \frac{1}{1+\kappa^2/4}\frac{\sin 2\theta_{max}}{\cos\theta_{max}(1+\cos 2\theta_{max})}\right)^{-1/2}, \tag{4.17}$$

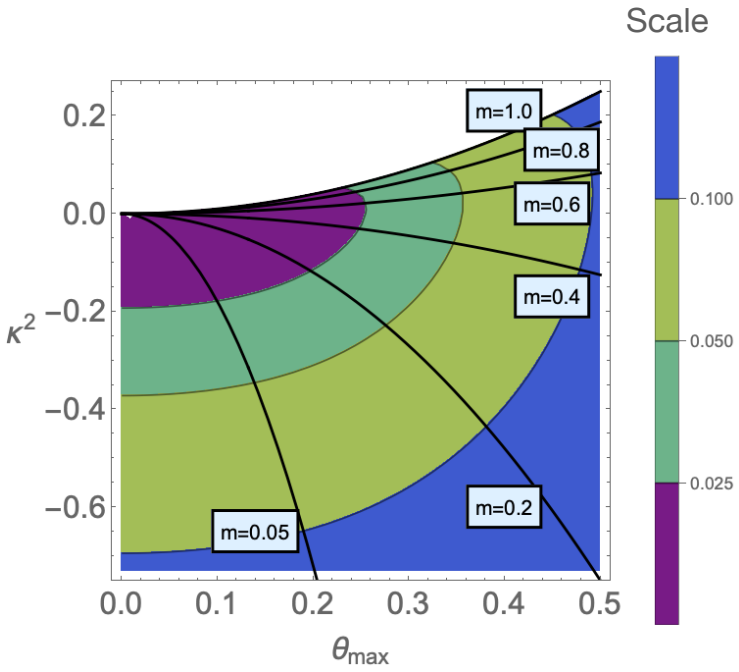

Figure 4.9: Contour plot showing an estimate of the difference between solutions for the full equation and for the reduced equation. The contours are lines of constant values for ϵ_{w_p}, Eq (4.19). Errors less than 10% are achieved for $-0.6 < \kappa^2 < 0.1$ and $\theta_{max} < 0.4$, approximately. The thick black lines show the variation of κ^2 as a function of θ_{max}, computed from Eqn (4.9), for six different values of the squared Jacobi modulus m.

while the reduced equation, Eqn (4.3), gives

$$w_{p,reduced} = 2\sqrt{\frac{2\theta_{max}}{1+\theta_{max}^2}}\left[\arctan\theta_{max}\left(2(1+\kappa^2/4)\arctan^2\theta_{max}-\kappa^2\right)\right]^{-1/2}. \quad (4.18)$$

The relative difference in width w_p, defined as

$$\epsilon_{w_p} = |w_{p,full} - w_{p,reduced}|/w_{p,full}, \quad (4.19)$$

may then serve as an estimate of the error of the solutions of the reduced equation in relation to the full equation, Eqn (4.1); ϵ_{w_p} may be expressed analytically in terms of θ_0 and κ^2, using Eqns (4.17) and (4.18).

Figure 4.9 shows contours of constant error ϵ_{w_p}. In line with our expectations the relative error vanishes in the limit of $\theta_0, \kappa^2 \to 0$, and thus of compression.

4.5 Conclusions

Jacobi functions provide a full range of approximate solutions, easily evaluated and visualized, minimizing numerical calculations, elucidating qualitative features, and providing an accessible guide to the relationships of the several parameters ($N, \Delta, G_0, \theta_{max}, ...$) that characterize the chain buckling.

The analysis presented here was confined to hard wall boundary conditions. Other scaled Jacobi solutions arise when different boundary conditions are imposed, and some of these should also be accessible to foreseeable experiments. Sloping the walls of the pistons should induce different buckled structures, which could be described by other members of the family of Jacobi elliptic functions.

We now move away from the continuum theory and the description of a line of hard spheres held in confinement and under compression and/or tilt. We will now consider systems of soft, elastic spheres in their place. While the system is not amenable to the same analytic treatment as described in the previous two chapters, we will discuss various methods of describing and simulating such systems in Part II.

Part II

Soft Spheres

5 Background theory: Simulating bubbles and Morse-Witten theory

The simulation of soft, elastic, deformable particles is a focal point in computational physics and engineering. Understanding how these particles deform under the action of external forces is important for comprehending phenomena in cell biology [55],fluid dynamics [56] and materials science [57].

Our focus here will be to explore the techniques used to model soft, elastic particles. Given the application of this work, we will focus on systems of bubbles. We will explore three computational methods: the soft sphere model [58], the Surface Evolver program [59] and finally we will introduce the implementation of the Morse-Witten theory in three dimensions [44, 60]. In the next chapter we will discuss how we implement the latter theory in computer simulation.

We will focus on our usual system of a line of bubbles between two hard walls and confined in a transverse harmonic potential. The system demonstrates many features that are absent in the chain of hard spheres. Under an infinitesimal compression, the linear chain is no longer unstable. Instead the linear chain remains stable until a critical value of compression is reached. This critical value, and the predictions of the various theories and simulations methods, will be discussed in this chapter.

Figure 5.1: A bubble show in Kraków, Poland. Many of the interesting properties of bubbles are on display here. Most interesting to us are the bubble shapes. We note that the smaller bubbles are more spherical, while the larger bubbles show more deformations. This corresponds to the Bond number of these bubbles, as defined in Eqn (5.2). Larger bubbles, with larger Bond numbers, deform more under external forces. The smaller bubbles are more easily able to maintain their spherical shape.

5.1 Bubbles

Bubbles have been an object of fascination for people of all ages and at all levels of scientific literacy. They are associated with youth and playfulness (as seen in the work of artist Jean Simeon Chardin), but also with melancholy. The fleeting lifetime of a bubble alludes to the transience of life [61].

We shall leave such musings to artists and philosophers, however, as in the scope of this thesis we are interested in a bubble's shape (i.e. the surface defined by the liquid film) and its response to forces applied to it. The bubble's captivating spherical shape is due to the interplay between the bubble's surface tension, γ, and the difference between internal and external pressures. This is elegantly summarised by the equation of local equilibrium for a bubble surface, the Laplace-Young equation [62]:

$$\gamma \mathcal{C} = \Delta p, \tag{5.1}$$

where γ is the bubble's surface tension, $\mathcal{C}$ is the total curvature of the interface, and $\Delta p = p_{internal} - p_{external}$, the difference in internal/external pressures. If the pressure difference and surface tension are constant across the bubble surface, this defines the spherical shape we expect.

In the scope of this thesis, we shall assume that the bubble's internal gas is of low density and incompressible. As a consequence of this assumption, the internal pressure and volume of our bubble will be constant throughout. The external pressure, however, may vary due to contacts with other bubbles and/or surfaces, or due to a pressure gradient induced by gravity. In these cases the local curvature and therefore the bubble shape will change.

To characterise a bubble response to these contacts and/or pressure gradients we shall use the Bond number (or Eötvos number) [63], defined as:

$$Bo = \frac{\Delta\rho g R_0^2}{\gamma}. \tag{5.2}$$

Here $\Delta\rho$ is the density difference between the between the density of the internal and external media of the bubble, R_0^2 is the equivalent spherical radius of the bubble and again γ is the surface tension. The Bond number defines the relative importance of surface tension forces to external forces (in this case gravitational). For bubbles with a low Bond number, surface tension dominates and the bubbles tend to maintain their spherical shape; bubbles with larger Bond numbers are relatively unaffected by surface tension effects. Intermediate values indicate some balance between the two factors, which may be non-trivial to interpret. See Figure 5.1 for a classic illustration of the effect of Bond number on bubble shape.

The Laplace-Young equation may be solved numerically to calculate the profile of a bubble under the action of external forces [46], however the method is not amenable to systems containing multiple bubbles. Thus approximate models or numerical simulation are used to model the behaviour of systems of multiple bubbles. We shall briefly

discuss two of those here: The soft sphere model and the Surface Evolver.

5.2 The soft sphere model

In the soft sphere model (sometimes referred to as the Durian model [58]), soft particles are not deformable but instead maintain their spherical shape under applied external forces. Instead, these spheres are permitted to overlap with each other and boundaries. Overlaps are resisted with a Hookean force, with overlap δ_{ij} for two spheres of the same diameter defined as:

$$\delta_{ij} = |\mathbf{R}_i - \mathbf{R}_j| - D, \tag{5.3}$$

where $|\mathbf{R}|$ are the centre positions and D is the sphere diameter. As the interaction between particles is modelled like a Hookean spring, the energy associated with this overlap is then defined to be:

$$E_{ij}^2 = \frac{1}{2} k \delta_{ij}^2, \delta_{ij} \leq 0, \tag{5.4}$$

and zero otherwise, where k is an analogue to a Hookean spring constant. The advantages of such a model is its ease of computation, and that the choice of parameter k may be chosen to match experiment (for two contacting monodisperse bubbles, for example, it is often related to the surface tension [64]). However, the model has shortcomings in that it does not capture the non-local deformation of the soft particles due to applied forces.

We have already applied this model in previous sections to probe the stability of structures of hard spheres, Chapter 2. This was done by choosing a value of k that is much larger than the strength of the harmonic confining potential, so that the bubbles are approximately hard.

5.3 The Surface Evolver software

Developed in the 1990s by Ken Brakke, the Surface Evolver has become a 'workhorse' for modern soft matter physics [59, 60]. It is an interactive program, aimed for studying surfaces whose shapes are governed by surface tension and other energies.

Surface Evolver is designed to create and manipulate complex 2D and 3D geometries, making it valuable for studying surfaces, interfaces, and structures in different dimensions. Users can define the geometry of surfaces by specifying vertex coordinates, edge lengths, and surface curvatures. The level of refinement of the tesselation of the surfaces may be specified, allowing for a high degree of accuracy.

One of the central features of Surface Evolver is its ability to minimize the total surface energy of a given configuration. It employs variational methods to iteratively adjust the geometry of the surfaces to reach a state of equilibrium, where the surface energy is minimized. This is particularly useful for simulating the behavior of liquid-gas interfaces, soap films, and other surface-related phenomena. It supports a wide range of physical models and boundary conditions, allowing users to simulate various phenomena involving surface tension, gravity, capillarity, and more. This flexibility enables modelling a broad spectrum of real-world problems accurately, such as soap bubbles [59], foams [60], emulsions [65] , and the behavior of biological systems [55].

Surface Evolver offers tools to help users visualize and analyze their simulations. This includes features for plotting surface properties, tracking interface evolution, and generating graphical representations of simulated systems. It is also extensible, and interfacing with other software tools and data analysis packages is straightforward.

5.4 Morse-Witten theory

Surface Evolver and other similar simulation methods struggle when the size of contacts is small relative to the size of a bubble. In these cases, the tesselating faces of the Surface Evolver structure are comparable to the size of the contact faces, causing numerical problems. Therefore models such as the soft sphere model are often used. This model is not without its limitations, however. The soft sphere model defines an exclusively pairwise force between bubbles, which is not the case in many bubble structures [66]. The soft sphere model also makes use of a free parameter, the spring constant of the repulsive force between overlapping spheres, which is usually fitted to match with experimental data. This limits the predictive power of the model.

Here we will examine a theory first proposed by Morse and Witten [44] and extended to systems of multiple bubbles by Hoehler and Weaire in [60]. This theory begins with the Laplace-Young equation as presented in Eqn (5.1), and produces a linearised theory which is exact in the limit of small forces and deformations. Here we shall present the derivation as proposed in [60], and examine its predictions as compared with Surface Evolver and directly solving the Laplace-Young equation. In the next chapter we shall discuss how it may be implemented in a simulation of multiple bubbles.

To explain the derivation of the Morse-Witten model, we return to the problem proposed in the original paper [44], that of a single bubble pressed against a plate by buoyancy.

5.4.1 A single bubble buoyed against a plate

We shall proceed using dimensionless quantities, lengths are normalised by R_0 (the natural spherical radius of the bubble, for this case we shall consider only monodisperse systems, see Appendix A7 for a discussion about the effects of polydispersity), energies are normalised by γR_0^2 and forces by γR_0. We then may write dimensionless pressures P, z coordinate Z and curvature C (thus far we have used small letter to denote

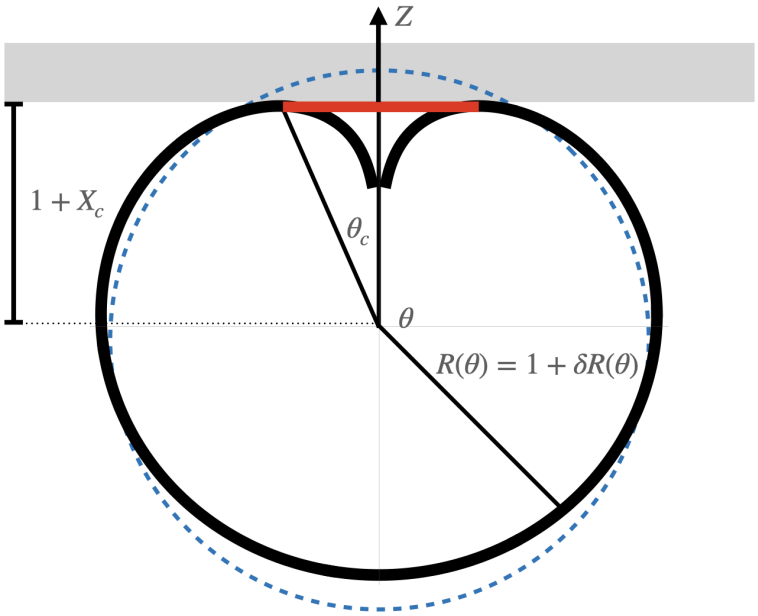

Figure 5.2: A cross-section of a 3D Morse-Witten bubble profile. The original spherical shape of the bubble (of radius 1) is shown as a dashed blue line, the deformed Morse-Witten profile is shown in black. Also shown is the 'cap', in red, used to account for the logarithmic divergence of the Morse-Witten profile. The distance from the centre of the mass of the bubble to the cap, $1 + X_c$, is given by Eq (5.10).

dimensionless quantities, however in this section we defer to the notation presented in [60, 64] where the dimensionless quantities are referred to with capital letters).

In the presence of a buoyancy force, there is a pressure difference across the height of the bubble. Thus the Laplace-Young equation, Eqn (5.1) becomes:

$$C = \Delta P_0 + 2 + BoZ, \tag{5.5}$$

where ΔP_0 is the pressure difference across the height of the bubble and Bo is the Bond number as defined in Eqn (5.2).

We now refer to Figure 5.2. We note that the structure is axially symmetric around the z-axis, thus we may describe the bubble surface profile with a single polar angle in spherical polar coordinates, placing the origin of the coordinate system on the centre of mass of the bubble.

Thus we write the equilibrium profile as:

$$R(\theta) = 1 + \delta R(\theta). \tag{5.6}$$

By linearising Eqn (5.5) with respect to $\delta R(\theta)$, an expression for $\delta R(\theta, Bo, \Delta P_0)$ can be found [60]. ΔP_0 may be found from the volume conservation constraint, noting that $\delta R(\theta, Bo)$ must average to zero across the bubble surface. This gives the expression for $\delta R(\theta)$ as:

$$\delta R(\theta) = 3Bo(1/2 + 4/3\cos\theta + \cos\theta \log(\sin^2(\theta/2))). \tag{5.7}$$

However, we may note that the force exerted on the bubble by the contact with the surface may be written as:

$$F = -\Delta\rho\frac{4\pi}{3}R_0^3\frac{1}{\gamma R_0} = -4\pi Bo/3. \tag{5.8}$$

Thus we write the deformation of the bubble surface in terms of this force by substituting into Eqn (5.7):

$$\delta R(\theta) = -FG(\theta), \tag{5.9}$$

where $G(\theta)$ is a Green's function which depends only on the angle θ.

Notably this Green's function, and thus the function $\delta R(\theta)$ diverges at the $\theta = 0$. The point force is "covered up" by a plane which sits tangentially on the bubble around the divergence, defined as a circular liquid film for $\theta < \theta_c$. For $\theta \geq \theta_c$, $\delta R(\theta)$ defines the profile. This cap does slightly increase the bubble volume, however this has shown to be negligible for small values of F [64]. This cap is represented by the red line in Figure 5.2. Note that the choice to place the plane of contact tangential to the bubble profile sets the contact angle between the bubble and the surface to zero.

Although the logarithmic divergence is "covered" by this cap and does not feature in

the bubble profile, it forms an important part of the expressions for force and energy. Most notably, when considering the distance between the centre of mass of the bubble and the point of contact (X_c in Figure 5.2), which is given as follows:

$$X_c = \frac{1}{24\pi}\left(5 + 6\ln(F/8\pi)\right)F, \tag{5.10}$$

the logarithmic term features. This interaction law is thus softer than the Hookean interaction used in models such as the soft sphere model, consistent with other analytical approaches. Also we note here that a positive displacement X_c means the bubble surface is compressed at the contact. It is also possible to have an extensive force, such that $X_c < 0$, and this case is discussed in Appendix A5.

Eqn (5.10) has an exact inverse given in terms of the *Lambert function*, or the product logarithm [52]. This multivalued function has the property that for any complex numbers z, w, then $we^w = z$ if and only if $w = W_k(z)$, where k is some integer. This makes the Lambert function useful for solving equations with logarithmic terms. In this case, as we deal exclusively in real numbers, we need only consider the W_{-1} branch. This then gives the inverse of Eqn (5.10) as:

$$F = \frac{4\pi X}{W_{-1}(e^{5/6}X/2)}. \tag{5.11}$$

The energy associated with the deformation at the contact may be obtained from the Work-Energy theorem, considering the work done as the force is increased from 0 to its equilibrium value as in Eqn (5.8). This results in the expression:

$$E = \frac{F^2}{8\pi}(-4\pi/3 - \ln F + \ln 8\pi), \tag{5.12}$$

noting again the logarithmic dependence on F.

Given its origin from a linearisation of Eqn (5.1) with respect to $\delta R(\theta)$, the

Morse-Witten theory is only valid in the limit of small deformations, becoming exact as $F \to 0$. We demonstrate this accuracy in Figure 5.3, where we compare the predictions of Surface-Evolver, the Laplace-Young equation and Morse-Witten theory for the shape of a bubble held under a plate by buoyancy, as a function of Bond number. We note that Surface-Evolver is not capable of calculating the shape as $Bo \to 0$, however in this limit the Morse-Witten theory agrees with the direct numerical solution of Laplace-Young exactly. Thus we believe that Morse-Witten theory is well-suited to 'filling the gap' of Surface-Evolver when it comes to considering structures that have bubbles subject to small deformations. This is most obviously the case for simulating foams of air and water, where the foam is 'wet', i.e. the volume fraction of the liquid is high [67]. In this case the bubbles of the foam are approximately spherical with only small deformations, the limit where Surface Evolver is not effective. The soft sphere model may be used in this case, but it has been shown that it incorrectly predicts many physical characteristics of the foam [68].

To apply the Morse-Witten theory to such structures, or indeed the chain-like structures which are the focus of this thesis, we must consider how to implement a bubble with multiple contacts - which may be with other bubbles or boundary surfaces.

5.4.2 A single bubble with multiple contacts

We will now address the question of how to describe a bubble held in mechanical equilibirum by external forces, in the absence of buoyancy. We refer again to the review article [60], where this problem was addressed.

They propose a linearised theory, where solutions $\delta R(\theta, \phi)$ for each force (with each force compensated by a pressure gradient, like buoyancy), may be added together to produced the complete bubble profile. Given the condition of mechanical equilibrium, when these profiles are combined the net pressure gradient on the bubble will be zero; equivalent to a bubble in mechanical equilibrium in the absence of a pressure gradient. The compensating pressure gradients are a construction for this problem, and do not

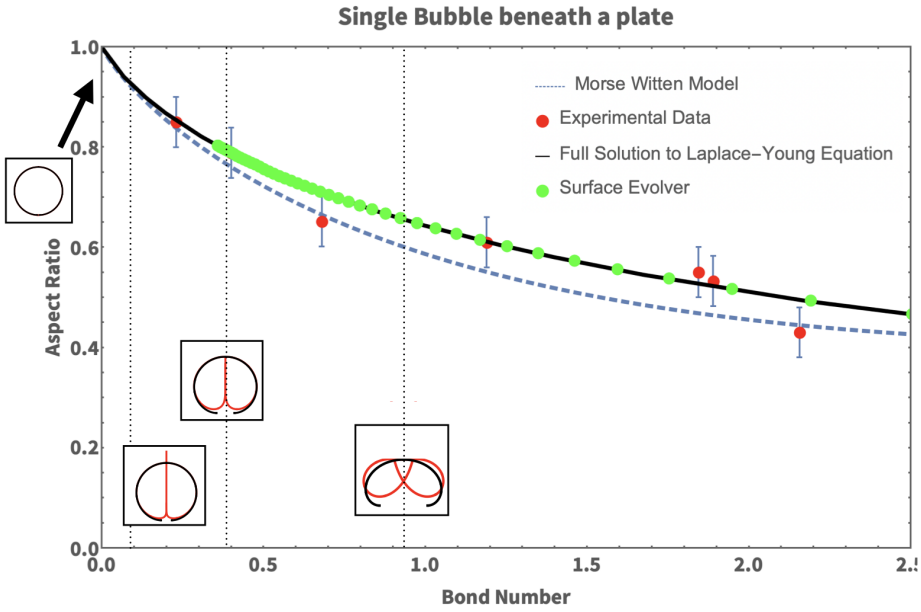

Figure 5.3: A comparison between the Laplace-Young equation, Surface Evolver and Morse-Witten theory for a single bubble buoyed against a plate. Here we plot the aspect ratio, i.e. the maximal extension of the bubble perpendicular to the plate h divided by the maximal extension of the bubble in a plane parallel to the plate w. We note that as $Bo \to 0$, the Morse-Witten model agrees with the Laplace-Young equation exactly. In this limit, Surface Evolver cannot accurately resolve the structure due to the shrinking contact area. Also included are some experimental points, in red with error bars (taken by Ali Irannezhad), to give context for these theoretical predictions. These measurements were made for a bubble under a flat plate, using the same parameters as those discussed in Figure 5.4.

feature in the final result.

For this linearised approach we must assume that in general that the contact points are far away from each other on the bubble surface, i.e. that the angle between contacts is greater than the sum of their 'capping' angles, θ_c. Otherwise the logarithmic divergence of the Green's functions in the vicinity of the contacts will interfere with the overall profile.

Employing all of this, therefore, we may write:

$$R(\theta, \phi) = 1 - \sum_i F_i G(\theta_i), \tag{5.13}$$

where θ_i is the angle between the vectors between the centre of mass, $R(\theta, \phi)$ and the contact f_i.

If we consider the displacement of the bubble surface at a contact, i, we may more explicitly see the form of a bubble-bubble interaction:

$$X_i = \frac{1}{24\pi} \left(5 + 6 \ln(F_i/8\pi)\right) F_i - \sum_{j \neq i} G(\theta_{ij}) F_j, \tag{5.14}$$

where θ_{ij} is the interior angle between contacts i and j. Here we see that there is a 'local' term, a deformation caused by the force acting at contact i. However, for each contact point $j \neq i$ there is also a contribution to the displacement: a non-local term. This form of a non-pairwise interaction has been observed between multiple bubbles in experiment [66], and is a feature of the Morse-Witten model.

Unlike Eqn (5.10), Eqn (5.14) does not have an analytic inverse. In the next chapter we will discuss a numerical method for determining the forces f from the displacements x. We also note that this equation only holds for the case of monodisperse bubbles in contact, due to the fact that all quantities are normalised by the bubble radius R_0. An extension to the case of bubbles of different size in contact is presented in Appendix A7 (this was also discussed in [60], however we note that there is an error in the

equations presented there for polydisperse bubbles).

5.5 Lines of soft spheres

We now return to the familiar set-up discussed in Part I of this thesis: a line of spheres, held in a transverse harmonic potential, confined between two hard walls. We now ask the question, what is the expected behaviour of a line of bubbles under compression and how does it compare to the system of hard spheres?

Firstly, we now modify our original definition of compression (Eqn (1.3)) to account for the possible non-spherical shape of our bubbles:

$$\Delta = (2NR_0 - L)/2R_0, \tag{5.15}$$

where L is the distance between the two hard walls, and R_0 is the equivalent spherical radius of the bubbles in our system. Again, we also define the related compressive strain $\epsilon = \Delta/N$.

We refer back to the experimental work done by Weaire *et al.* in [41], and as discussed in Section 1.3. Immediately it is obvious that the system bears more in common with the Euler buckling problem, see Section 1.1. Unlike the chain of hard spheres, the chain of bubbles is not rendered instantly unstable under an infinitesimal compression. In fact, the linear chain remains the preferred structure until a critical value of compression, Δ_c, is reached.

After this point, the structure moves into the zig-zag pattern familiar from the hard sphere case. It demonstrates a similar tendency to buckle locally, before reaching the doublet state. This doublet state once again remains stable under compression, until the transition to the zipper state occurs. Beyond this point, the structure moves into a 3-dimensional configuration similar to that of the hard sphere system. This evolution can be seen in Figure 1.10.

This is most easily understood by examining systems of 1, 2, and 3 bubbles under compression. Experimental results for these small systems are shown in Figure 5.4, obtained using the experimental method described in Section 1.3. There we plot the maximal extension of the bubbles in the direction perpendicular to the cylindrical axis as a function of the distance between the two hard walls. We note that initially, the increase in width is independent of the number of bubbles; this is more evident in Figure 5.4 (b), where the width is plotted as a function of compressive strain. It is only at the point where buckling occurs that the differences between the 2 and 3 bubble system become obvious.

In Appendix A6 we present a derivation of analytic expressions for the width of these small-N bubble systems, using Morse-Witten theory as the model for bubble-bubble interaction. It is possible to derive analytic curves for the expected width profiles as a function of Bond number. A representative comparison between experimental results and these analytic curves are shown in Figure 5.5. We will employ these expressions in the next chapter, where we will use it as a test case for simulations of Morse-Witten bubbles in 3D.

5.6 Conclusion

We have briefly discussed modern methods of simulating bubbles experiencing small deformations: the Soft Sphere model, the Surface Evolver and Morse-Witten theory. The advantages of Morse-Witten theory are apparent here, as it conforms exactly to solutions of the Laplace-Young equation in the limit of low Bond number; the region where Surface Evolver struggles to converge satisfactorily. Morse-Witten theory also captures non-pairwise interactions between bubbles, which the Soft Sphere model does not capture.

Moving to our familiar system of bubbles held in a harmonic confining potential, squeezed between two walls, we find that theoretical predictions of Morse-Witten correspond well to experimental findings. Morse-Witten accurately predicts the increase

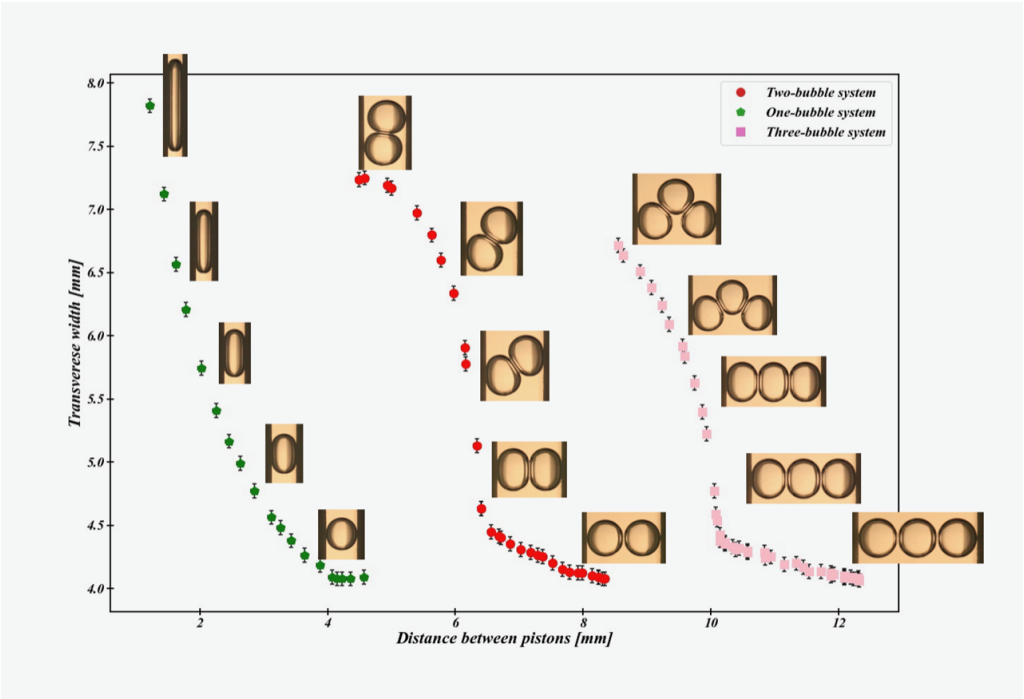

(a)

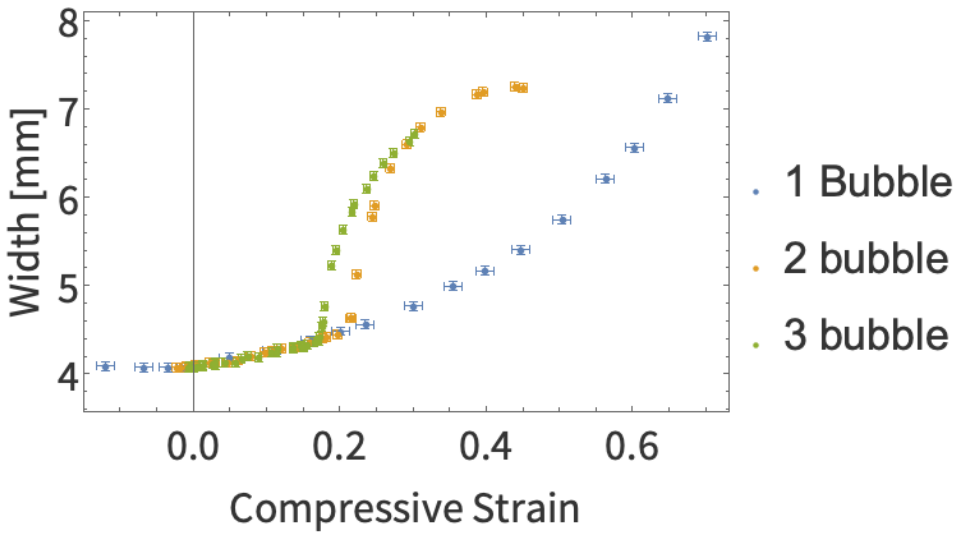

(b)

Figure 5.4: (a) Photographs and experimental data obtained for systems of 1, 2, 3 bubbles, measured by Ali Irannezhad. Here we show a plot of the maximal width as a function of the distance between the two pistons (these images are obtained from the experimental system discussed in Section 1.3). These experiments were performed with aqueous solutions of SDS at the critical micelle concentration (cmc). This was done to ensure an accuracte measurement of surface tension, and thus Bond number. Measured value of surface tension: 34.3 ± 0.1 mN/m (measured at 24 degrees Celsius). Tube diameter $2r = 15.6 \pm 0.03mm$, bubble diameter $D = 2R_0 = 3.727mm$, and thus ratio of bubble to tube diameter is $\simeq 0.24$. The Bond number of these bubbles, as defined in Eqn (5.2), is $Bo = 0.993$. (b) shows the width of these structures as a function of the compressive strain, defined as in Eqn (5.15), showing that the increase in width before buckling is independent of the number of bubbles. Note that the compressive strain may be negative for this experimental system, this is due to the fact that even when uncompressed by the walls, the bubbles are extended due to their contact with the surface of the cylinder, so the natural length of their linear arrangement is longer than $2NR_0$ (Eqn (5.15)). See Appendix A6 for more details.

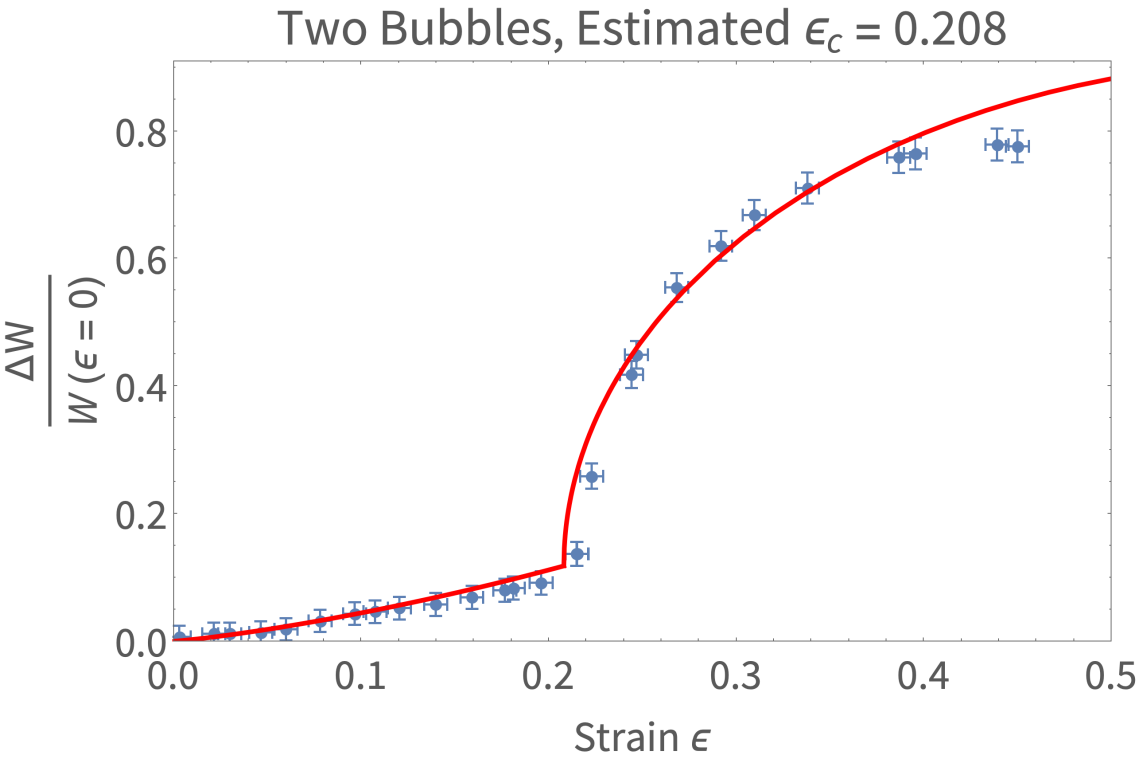

Figure 5.5: Here we plot the dimensionless increase in width as a function of the compressive strain for the 2 bubble system. The experimental data, in blue, is the same as presented in Figure 5.4. The red curves represent the analytic prediction of Morse-Witten theory, as derived in Appendix A6. Here the critical value of strain, where buckling occurs, is estimated from the experimental data: it is the only free parameter in the Morse-Witten curves. The discrepancy between the Morse-Witten prediction (which predicts a critical value $\epsilon_c \approx 0.25$) and the experimental result is attributed to the relatively large Bond number of the bubbles in experiment, $Bo = 0.993$.

in width of the system during the compression phase, and also correctly predicts the form of the buckling. There is a discrepancy in the predicted critical value of compression at which buckling occurs, but that can be attributed to the large value of the Bond number in the experiment; constructing bubbles with lower Bond number is difficult.

This simplified system will now be used as the test case for numerical simulations of Morse-Witten bubbles. In the next chapter we will discuss how Morse-Witten theory may be used to construct an algorithm to find structures of Morse-Witten bubbles in mechanical equilibrium. The two-bubble case presented here will be used as a test case for that simulation.

6 Chains of Morse-Witten bubbles under compression: Simulation

We now consider the same confining set-up as in Part I, spheres held in line between two pistons due to the action of a transverse, harmonic confining potential. In this case however, we shall consider bubbles. We note that now the bubbles do not buckle immediately under small compressions, rather the entire chain will 'squeeze' first, before moving into our familiar structures demonstrating localised buckling (similar to the process of Euler buckling discussed in Chapter 1.1). We will model these elastic bubbles using the aforementioned theory of Morse-Witten, both through the implementation of a simulation and full analysis of the simplest case, the two bubble system.

6.1 Morse-Witten simulation

Previously, Morse-Witten simulations have been limited to the 2D case [64] or the case where structures are highly ordered [45]. In both cases periodic boundary conditions were used. In this case we will implement a simulation of the 3D Morse-Witten model, where the bubbles are confined within a cylindrically symmetric potential. To begin with, we shall concern ourselves with finding systems in mechanical equilibrium. We will use simulated annealing to determine minimum energy structures for given parameters, such as chain length and the strength of the harmonic confining potential.

A flowchart demonstrating the iterative scheme to find equilibrium can be seen in Figure 6.1. A more detailed description of each step follows.

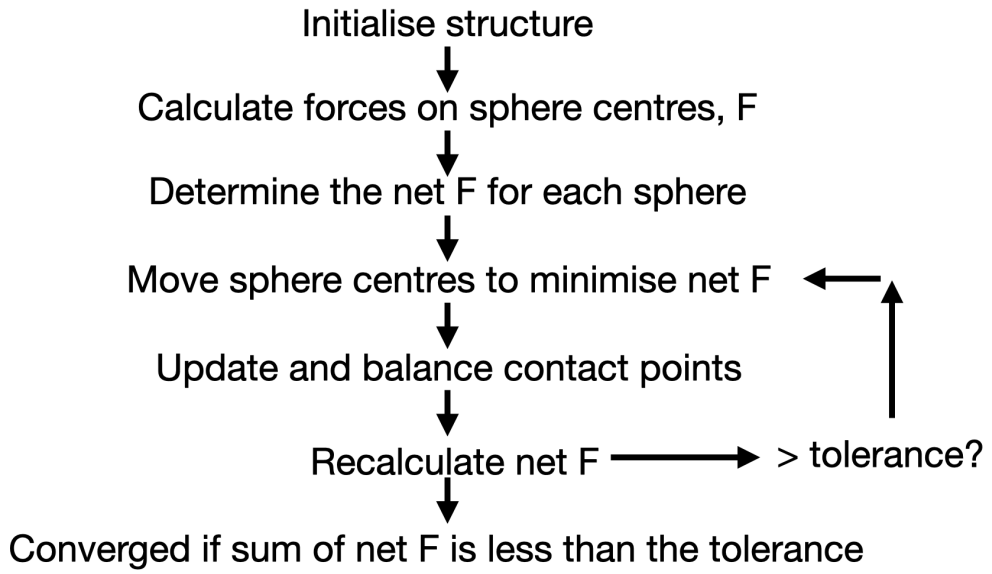

Figure 6.1: A flowchart of the iterative approach used for finding Morse-Witten structures in mechanical equilibrium.

The iterative approach

Initialising the bubbles

The initial input is loaded from a file listing the position of the bubble centres. Here we take advantage of the fact that Morse-Witten theory needs only the positions of the centres and the contacts in order to calculate the profile of a bubble. Thus the problem can be reduced to considering the positions of these centres and contacts. It is at this point that the parameters of the confining potential are also defined.

Calculating f_i

This represents the most computationally expensive step of the algorithm. Given the foam network, with its centre and contact points, we can calculate the displacements at $c_{i,j}$ directly. However, the corresponding f_i exerted by this contact point on its parent bubbles must be calculated by inverting Eqn (5.14), reminding ourselves:

$$x_i = \frac{1}{24\pi}\left(5 + 6\ln(f_i/8\pi)\right) f_i - \sum_{j\neq i} G(\theta_{ij}) f_j,$$

we note that this is a nonlinear matrix equation, containing a term with $\log(f)$, and must be solved algorithmically. Such a method was proposed in the review article of Hoehler and Weaire [69], and is what we implement here.

We can make an approximation of f_i using a variety of methods. The most straightforward is to use the 'Durian' model of soft bubbles, where the force f_i is proportional to the overlap of the equivalent spherical bubbles associated with this contact (see Section 5.2). We call this approximation $\tilde{f}$. Substituting $\tilde{f}_i$ into *only* the logarithmic term of Equation 5.14 produces an equation which is now *linear* in f, and can be solved using standard methods in Python [70].

This produces a solution for f, which we call $\tilde{f}^*$. We can now set $\tilde{f}_i = \tilde{f}_i^*$, and solve the linearised version of Equation 5.14 again. In the case of small deformations, i.e. the true value of f_i is small, this algorithm converges to $\tilde{f} = f$, the true value of the solution. This is implemented by calculating the residual vector between successive iterations. Once the magnitude of the residual vector falls below a defined threshold value, the algorithm is considered to have converged, and the result used as the solution to Eq (5.14).

Moving bubble centres

After calculating the net force f,on a bubble's center, we also compute the force, f_p due to the bubble's position in the potential field, which may be zero. This force is added to the net force. Then, we update the bubble center's position by moving it towards the net force direction. To prevent oscillations near equilibrium, we apply a dynamic damping term that scales inversely with the number of iterations. However, it's important to note that this method may not always eliminate oscillations close to equilibrium, as we will discuss later.

Updating Contact Points

After the movement of bubble centres, contact points may be created or destroyed. In alternative models, such as the soft sphere model, it is sufficient to check that the

distance between two bubble centres is less than the bubble radii to determine the validity of a contact.

In this simulation of Morse-Witten bubbles, we use the fact that the forces are small and that the bubbles are approximately spherical (and therefore the caps on contacts, θ_c are small enough), to justify checking the bubble extensions along their centre-centre lines to determine contacts. This would not be the case where f is large and bubble deformations are significant. Given that forces of these magnitudes are beyond our accepted range of validity of the Morse-Witten model ($f < 1$), we will not account for this effect here. A more sophisticated algorithm for determining bubble contacts is proposed in the Outlook chapter of this thesis.

In addition to the condition of mechanical equilibrium of the bubble centres, it is also necessary to determine mechanical equilibrium with respect to the contact points, i.e. that the forces across a contact are balanced, $f_{i,j} = f_{j,i}$. Unlike the soft-sphere model, the non-pairwise nature of the Morse-Witten interaction means that this contact point may not be at the midpoint of the centre-centre line between bubbles. We assume that in equilibrated structures that the contact does lie on the centre-centre line. This may not always be the case, and we will address this problem in the Outlook chapter of this thesis.

Therefore, after the validity of a contact has been determined, the contact point is moved along the centre-centre line until the equilibrium position is found, using Eqn (5.14).

Sum of $|F|$ and Convergence

Using the updated positions of the bubble centres and contact points, the net force f of each bubble is calculated and summed. The criterion for convergence for this algorithm is mechanical equilibrium, and so when this quantity falls below a pre-defined threshold value (usually $|f_{tot}| \approx 10^{-8}$), the system is considered to have converged (assuming the condition of mechanical equilibrium across contact points is also

satisfied). Examples of converged structures, and plots of the magnitude of the net force as a function of equilibration step, are shown in Figure 6.4.

Determining structures of lowest energy

There is, of course, no guarantee that this iterative approach will produce minimum-energy structures, and thus the discovered structures may not correspond to those found in experimental systems. To account for this, we implement an annealing process in addition to the iterative method. Once an equilibrium structure is found, the positions of the centres within that structure are 'kicked' by some displacement s, proportional to a temperature parameter T. The structure is then re-equilibrated, and may or may not return to the original result. After this, the annealing step is repeated, with T decaying after each successive iteration.

Given a sufficient number of iterations, we expect to find one or more different structures. Each of these structures is in equilibrium, with Morse-Witten theory satisfied. Therefore the energies of each structure can be calculated and compared, and a minimum energy structure can be determined.

Another method for this was recently proposed by D. Weaire, based on approaches to similar problems in molecular dynamics. Unlike the annealing process detailed above, where the bubble centres are displaced in order to explore the energy landscape, the proposed method varies the forces acting on the bubble centres while maintaining their positions. The forces are then chosen such that the structures are of minimum energy, then the position of the centres are moved such that the Morse-Witten equations are satisfied.

The advantage of this approach would be that each step of the equilibration method would correspond to an equilibrium Morse-Witten structure, albeit with constructed forces used to hold the structure in equilibrium. This means that, analogously to molecular dynamics simulations, calculated quantities such as the total energy of the system could be measured at each step of the equilibration process [71].

We have implemented this method, but have found it more involved and slower to find the equilibrium structures. It has been more practical to use the annealing method. However, this approach could be used in future applications of the Morse-Witten model, and may even be more appropriate to use in the case of systems such as bulk foams, where the minimum energy equilibrium configuration may not be so obvious.

Visualisation

Once equilibrated, our structures are stored in the JSON format [72] containing the positions of the centres, the positions of the contacts, and the forces associated with each bubble centre. This information can be straightforwardly loaded into the open-source 3D CG Technology software, Blender [73]. There we may represent our structures in two ways. Firstly we may plot the profiles $R(\theta)$, as defined by the Morse-Witten model.

However, we may also take advantage of the fact that the Morse-Witten bubbles are completely defined by the positions of the centres, the position of the contact points, and the forces associated with those contacts. This means we may represent the structure as a 'force network' (previously implemented for the 2D Morse-Witten foam in [64]). Here the bubble centres are represented as small bubbles, and a contact between bubbles is represented by a connecting bar. The radius of this bar is proportional to the magnitude of the force associated with that contact. We will use both visualisation methods in the results section of this chapter.

6.2 Tests

Here we will describe the evolution of two extremely simple systems: the case of two and three Morse-Witten bubbles held between two pistons in the usual transverse harmonic potential. These two examples will demonstrate the usefulness of the annealing approach, as well as verifying the iterative method with analytic

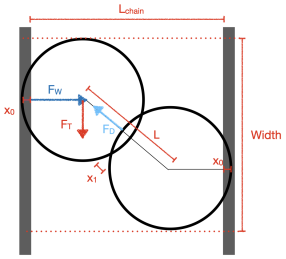

(a)

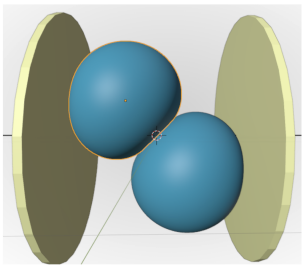

(b)

Figure 6.2: (a) A rough schematic of two Morse-Witten bubbles held between two pistons and confined by a transverse, harmonic potential. Indicated are the length of the chain and width of the system, the two quantities used to characterise the buckling arrangement. (b) A visualisation of two Morse-Witten bubbles held between two pistons using Blender, see Section 6.1 for more details. Clearly visible are the deformations of the bubbles away from their spherical shape.

Morse-Witten results.

To start with, we shall test the simplest system of two bubbles held between two pistons (represented by flat surfaces). This system demonstrates the usefulness of the annealing approach most simply. The linear structure is always mechanically stable, however we expect there to be a critical value of compression Δ (where we define compression as in Eq (5.15)) at which the linear chain is no longer the energetically favourable solution, and in experiments, one would see the movement from the linear chain to the buckled structure.

We may derive analytic expressions using Morse-Witten for the 2-bubble system, expressing the maximal transverse width of the system as a function of compressive strain (Δ/N). We can also express the critical value of strain as a function of the ratio of the surface tension (a measure of the hardness of the bubbles) and the spring constant of the confining potential k_p. These expressions are given below, and their derivation may be found in Appendix A6.

The initial increase in width is given by:

$$w = 2\left(1 - \frac{\epsilon}{W_{-1}(-\epsilon/2)}\right), \tag{6.1}$$

where W_{-1} is the -1 branch of the Lambert function (or product log) [74].

We may also write an expression for the critical value of strain using the Morse-Witten equations, here written in terms of the ratio k_p/γ, a measure of the stiffness of a Morse-Witten bubble against the strength of the confining potential:

$$\epsilon_c = \left(1 - \frac{\gamma}{k_p} f_c\left(Bo, \gamma/k_p\right)\right). \tag{6.2}$$

And finally, we can also derive an expression for the width as a function of ϵ for $\epsilon > \epsilon_c$:

$$\Delta\omega = \frac{1}{w(\epsilon = 0, Bo)}\left(w(\epsilon_c, Bo) + 4\sqrt{\Delta\epsilon(1-\epsilon)}\right), \Delta\epsilon = \epsilon - \epsilon_c. \tag{6.3}$$

A comparison of these theoretical curves and the results found from simulation are shown in Figure 6.3. They are found to be in good agreement for a range of values of the confining potential k_p.

6.3 Results

Simulations of chains have been run for systems containing up to 40 bubbles, at compressions ranging from $\Delta = 0$ to approximately $\Delta = N - 2$. We show examples of structures for $N = 9$ in Figure 6.4.

An often-used parameter to characterise structures, most usually in the study of granular materials [75] or the study of foams [76], is the valence number. This is simply the average number of contacts per bubble, which we will present here as a function of the compression of the chain $Z(\Delta)$. An example of the variation of this quantity for a system of 40 bubbles is shown in Figure 6.5. On this figure we have also marked the regions of compression in which our defined kinds of structures occur (focussing on the linear, zig-zag, doublet and zipper structures, see Figure 1.11).

Initially Z plateaus as the structure remains in the linear to zig-zag phase and bubbles only maintain a nearest neighbour contact. Then there is a narrow region of

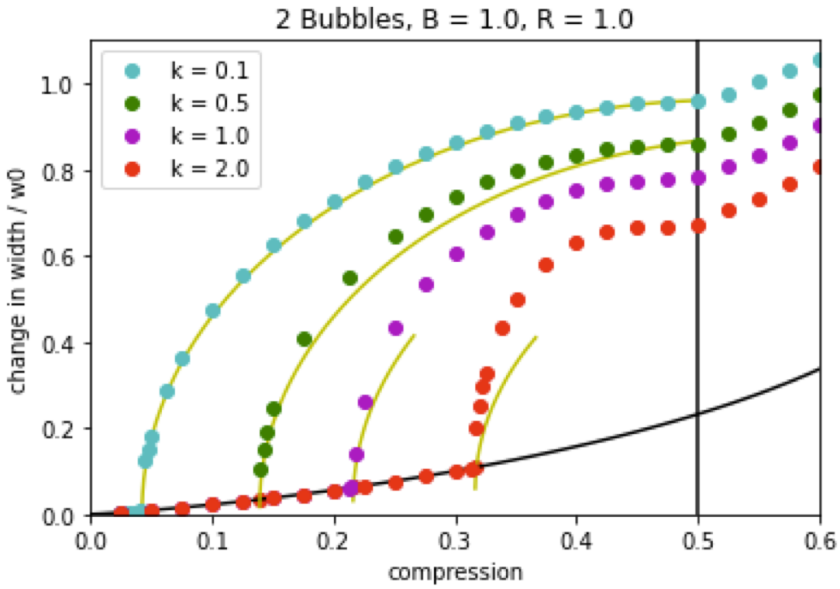

Figure 6.3: A comparison of the theoretical curves given by Eqs (6.1),(6.2) and (6.3) for varying values of the strength of the confining potential k, and we find them to be in good agreement with the simulation results, in particular at low values of Bond number where Morse-Witten theory is most accurate. We notice that Eq (6.3) holds up until the point indicated by a vertical line. At this point, each bubble makes contact with the opposite piston and forms what we call the doublet structure. The increase in width beyond that point is approximately linear.

compression at which the doublet forms. Similar to the linear chain, the doublet structure remains stable under a small range of compressions, until it forms the beginning of the zipper structure.

The region of the 'zipper' is actually a heterogeneous mix of a zipper and zig-zag structure. As compression increases, the value of Z also increases as bubbles join the zipper structure. The structure then becomes a homogenous zipper structure at a value of $Z = (4N - 2)/N$ (where the subtraction of 2 accounts for the fact that the bubbles in contact with the wall have one fewer contact than those in the zipper structure).

Beyond this point, the zipper structure twists into a 3D structure, and each bubble gains additional contacts as compression increases. This is accompanied by sharp increases of $Z(\Delta)$ close to the maximal compression, as bubbles also make contact with the confining walls.

This matches the expected behaviour of our system, however we still lack the ability to make a detailed comparison with other methods. Methods such as the Surface Evolver or soft sphere model could be used, but Surface Evolver struggles with determining the topological rearrangements of the bubbles under compression, and the soft sphere model does not capture many of the essential features of the system.

Currently, our best comparison is with the test-case system discussed in the previous section, where we also have access to experimental data. As we showed in the previous chapter, our analytic results do match the experimental data, and these are consistent with our experimental results. Thus we claim that the results of the simulations presented here are broadly accurate. Methods for more detailed comparisons with experiment will be detailed in the Outlook chapter of this thesis.

Unconverged structures

Similar to the case of 2D Morse-Witten structures [64], the 3D simulations often run into problems with convergence. Currently our systems are limited in scale to

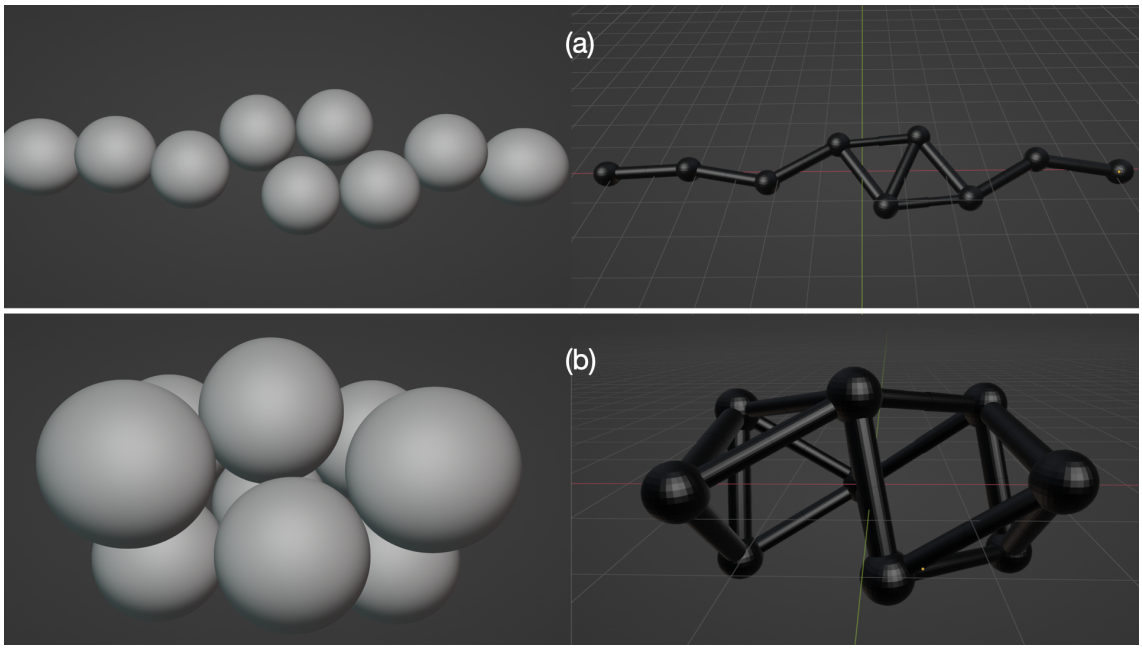

Figure 6.4: Examples of the Blender renders and force networks for chains of two different lengths, both containing 9 spheres: (a) $\Delta = 2.7$ and (b) $\Delta = 6.2$. (a) shows a planar structure, a portion of the 'zipper' structure as discussed in Section 1.3. (b) shows a 3D structure.

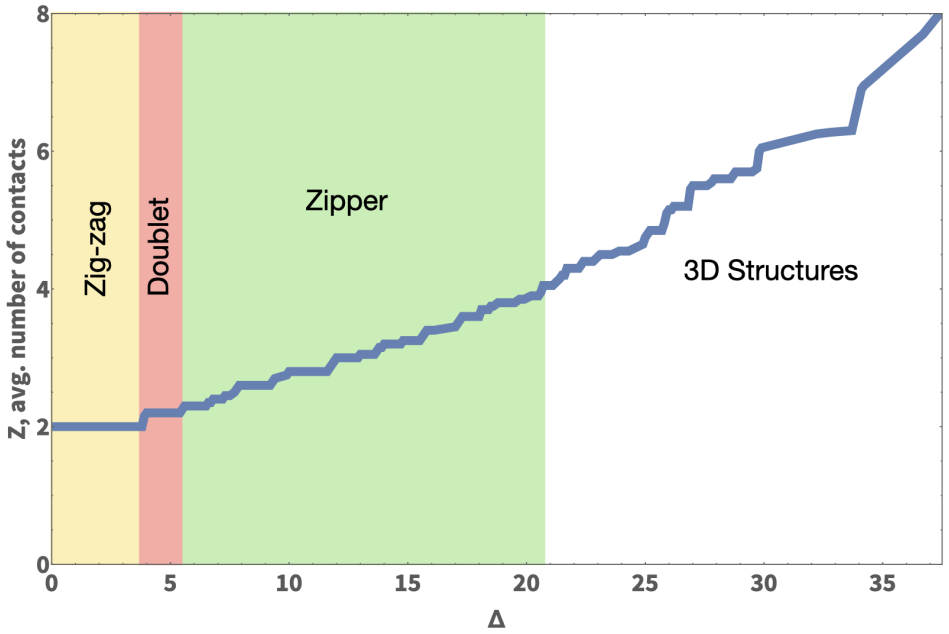

Figure 6.5: A plot of the average number of contacts per bubble, Z, as a function of compression, for a chain of $N = 40$ bubbles, $k_p = 0.25$. Initially Z remains at 2, through the compression phase and the zig-zag phase. The formation of the doublet is clearly visible, then Z continues to increase as more bubbles join the 'zipper' structure (Figure 1.11). The continuing increase of Z represents the compression of this structure, as well as the beginning of the twisting. Eventually, Finally, Z increases again as bubbles form additional contacts as the twisting increases. The categorisation of these 3D structures is the subject of ongoing work.

approximately $N = 50$ bubbles, which is a significant obstacle to progressing work on this topic. While we will propose some methods for correcting this issue in the Outlook, it is instructive to examine the nature of a non-convergent run to explain the difficulties.

A plot of the net-force of each bubble, and the resulting structure, for a system of $N = 12, \Delta = 4$ is presented in Figure 6.6. We allow the simulation to run for half a million iterations, demonstrating that this is not an issue of computational time. As can be seen, some of the forces on bubbles enter an oscillatory behaviour (such as that in green), oscillating between two values of f at a rate of per iteration. However two bubbles make the majority of the contribution to the unbalanced force, settling at around $f = 10^{-1}$. These two bubbles are also indicated on the force network diagram.

In spite of the dynamic dampening implemented, these oscillations do not diminish with iteration number. It is for this reason that we believe the non-convergent results are due to contact loss/gain, where structures may be losing or gaining contacts at a rate close to once per iteration. This constant changing topology makes obtaining an equilibrium structure difficult.

Visually inspecting the structures reveals no obvious abnormalities (other that in the case of Figure 6.6, it is unlikely to be the minimum energy structure for this value of compression). Thus we conclude that the approach is mostly correct and finds structures which are close to mechanical equilibrium relatively quickly (again in the example in Figure 6.6, it settles into this oscillatory behaviour in less than 20% of the total equilibration time), but cannot fully equilibrate due to the changing topology. This is as much a physical problem as a numerical one, and we will propose methods for ameliorating it in the Outlook.

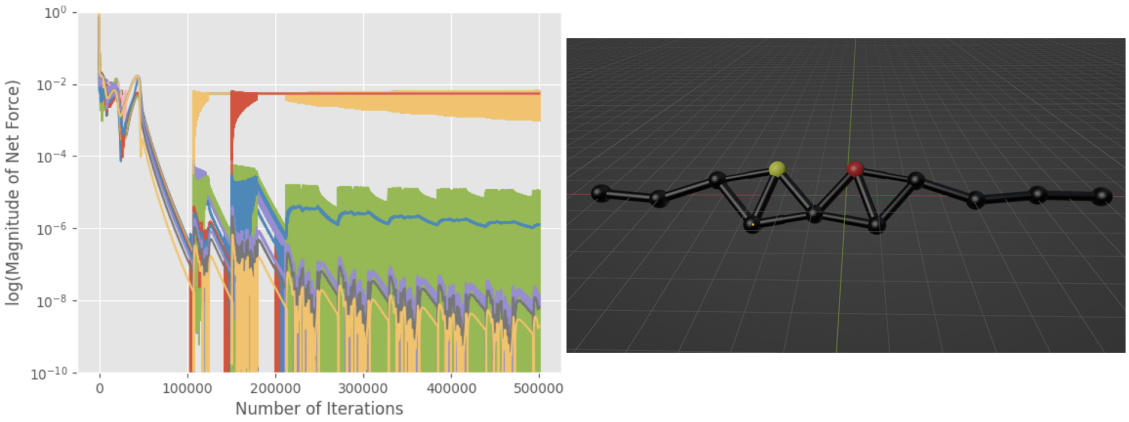

Figure 6.6: An example of an unconverged simulation for $N = 12, \Delta = 4$. Here we plot the contribution of each bubble to the total net force separately, represented by different colours in the figure on the left. We note that two bubbles, given by the red and yellow curves, are primarily responsible for the non-convergence, and are highlighted in the force network diagram shown on the right. The oscillatory behaviour of the non-convergent simulations can clearly be seen. Visually there are no obvious abnormalities with this structure, other than the fact that it is unlikely to be the minimum energy structure for this value of compression. We will propose methods for ameliorating these issues with non-convergence in the Outlook chapter.

6.4 Conclusion

Although much of this work is still in a preliminary stage, the method shows great promise in its ability to accurately simulate and visualise structures of Morse-Witten 3D bubbles. Here we have proposed an algorithm to find structures of 3D Morse-Witten bubbles, focusing on the system of bubbles confined along the axis of a cylindrically symmetric, harmonic confining potential. We have noted the transitions between linear, planar and three-dimensional structures and verified the output of the simulation with analytical expressions.

The issue of non-convergent simulations is a pertinent one, however we believe it requires a rethinking of the physics of the problem, rather than a total reinvention of the simulation method. We will propose methods of improving the simulation method in these cases. However, as previously noted, we believe that even 'unconverged' solutions may provide interesting data, given that they are indeed close to the true equilibrium structure.

The ability of the Morse-Witten theory to fully describe a structure of bubbles using only a contact network diagram makes it attractive for problems beyond the scope of those presented here. In particular, it would be useful for the description of foams close to the "jamming point" [67]. In that case, the foam has a low enough liquid volume fraction such that the bubbles in the foam are 'kissing', i.e. making very small contact areas with each other. Work has been done in simulating such foams with Surface Evolver [59], and other similar simulation methods, but methods such as Surface Evolver do not allow for zero contact angle. We believe that this simulation approach to Morse-Witten, provided that the issues are addressed, would be a good fit for this problem.

7 Outlook

We have presented a thorough analysis of our proposed model: a line of spheres confined by a transverse harmonic potential and axially two hard walls. We first examined the structures formed by hard spheres in our system. We extended the original iterative equations proposed in [43] to include the longitudinal force of tilt.

We then extended those iterative equations to a contiuum approach, replacing the discrete parameters of the original system with continuous functions. The resulting differential equation was explored numerically, and we solved it analytically in various limiting cases. In particular, we focussed on the Jacobi elliptic functions, which appeared both in the compression-only systems as well as the problem of Euler buckling.

We extended the model to include soft spheres, determining the critical points where structural transitions occur for different models of bubbles. We then applied Morse-Witten theory to the problem, simulating 3D structures using an algorithmic approach to find structures in mechanical equilibrium.

We will now present a number of avenues in which the work presented in this thesis may be extended. We will start with extensions to the continuum model approach, and then discuss how the 3D Morse-Witten simulation may be extended.

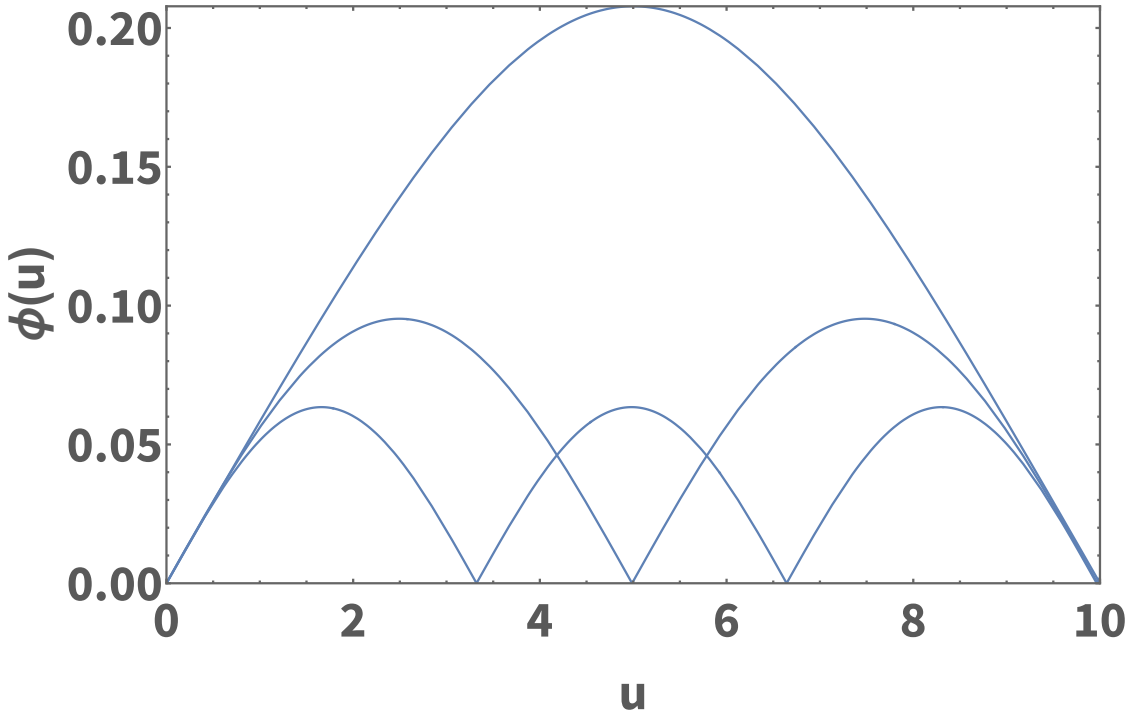

Figure 7.1: Here we plot a variety of solutions to Eqn (4.1). We show the absolute value to as to compare with the original single-peak positive solution. Here we match the slope of the solutions at the $\phi = 0$ boundary. These solutions still satisfy the required boundary conditions $\phi(0) = \phi(N) = 0$, but it is unclear how these solutions correspond to the physical system.

7.1 Extensions to the continuum model

Higher buckling modes

Analogously to the Euler buckling problem (Section 1.1), we expect there are higher buckling 'modes' that are solutions to the key differential equation, Eqn (4.1), but have internal zeroes. The periodic nature of the analytic solutions (see Figure 3.2) certainly suggests so. An example of one of these solutions, $\phi(u)$, with internal zeroes is shown in Figure 7.1.

It is unclear how to interpret such solutions. An underlying assumption of the iterative equations (Eqn (2.5), Eqn (2.6)) is that the displacements and angles y_n, ϕ_n are assumed to be positive. Interpreting the negative values of $\phi(u)$ in this case requires further analysis.

Figure 7.2: It is possible to vary the value of the boundary angle, $\phi(0)$, by modifying the experimental method detailed in Section 1.3. Here the originally straight boundaries are replaced with sloped stoppers, influencing a more uniform zig-zag profile. Although the stoppers pictured here are parallel, they do not necessarily need to be. Image credited to Ali Irannezhad.

Varying boundary conditions

An assumption throughout the thesis is that the boundary conditions $\phi(0) = \phi(N) = 0$ hold for these solution profiles. However, the reality in experiment is that this initial angle can be varied. An experimental example of this is shown in Figure 7.2, where the boundary angles of the experiment (using the experimental method detailed in Chapter 1.3) are varied through the use of slanted pistons. We briefly proposed this idea in Chapter 4, as a possible application of the other members of the Jacobi elliptic function family, see Figure 7.3.

7.2 Morse-Witten 3D Software

Improvements to be made to the software

The largest issue facing the current implementation of the Morse-Witten model is that of scalability. Currently the iterative implementation has poor scaling with N, the number of bubbles in the system, with computation time going with $\approx \mathcal{O}(N^2)$. This is primarily due to the exhaustive search done for contact gain and/or loss at each iterative step.

Aside from computation time, however, there is also the issue of large N systems not terminating satisfactorily when each bubble has > 2 contacts associated with it.

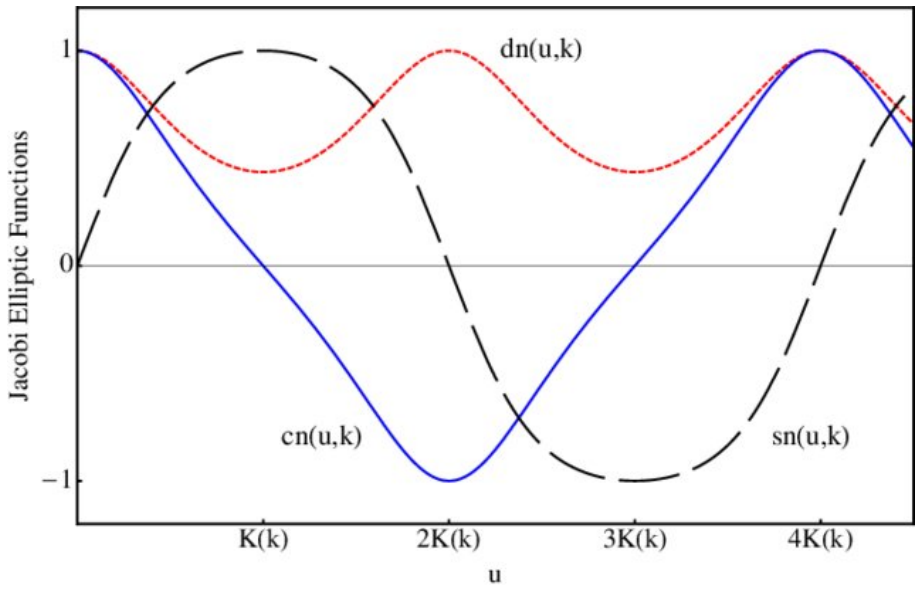

Figure 7.3: Here we plot the Jacobi elliptic functions *cn*, *sn*, *dn*, only one of which was used in 4. These other functions may be used to model solutions to the reduced equation, Eqn (4.3), with varying boundary conditions. This corresponds perhaps tilting the pistons of an experimental system, no longer having them perpendicular to the cylindrical axis of symmetry. This figure was reproduced from [77].

Currently, we believe this issue stems from the naive contact checking procedure which does not account for possible bubble deformation. Leaving aside equilibrated structures for now, where the deformations are generally small, there is no guarantee that the forces acting on a pair of bubbles will remain sufficiently small such that the assumption that the contact point lies on the centre-centre line will hold.

A suggestion made by Reinhard Hoehler, during discussions about the 3D Morse-Witten theory, for a more sophisticated contact checking algorithm is detailed in Figure 7.4. The bubble surface at the point which lies along the centre-centre line could be approximated as a paraboloid, and a new contact created if the paraboloids of a bubble pair intersect. Such a process would be able to capture contacts that would be made between bubbles with larger deformations, and would almost certainly be necessary if the software were to be extended to a polydisperse system of bubbles.

It is unclear at the moment whether this more advanced check of contacts is worth the computational expense incurred. It is a possibility that such spurious contacts may be the cause of the failure of systems with $N > 20$ to converge.

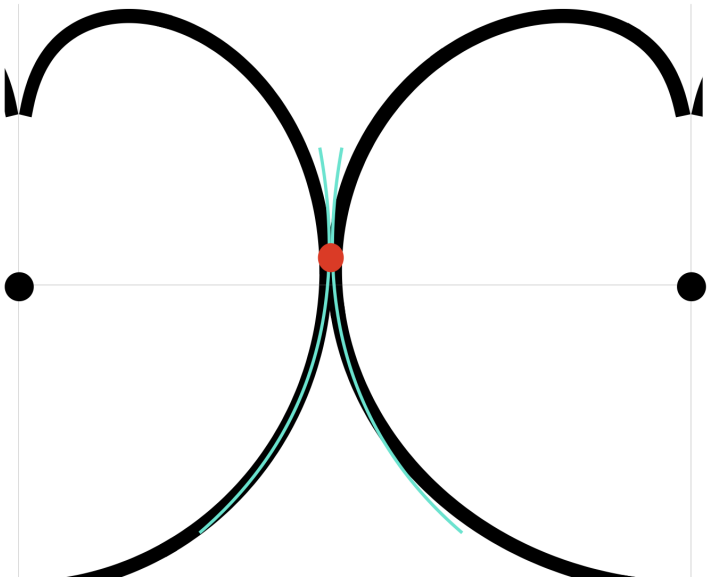

Figure 7.4: A cross-section of two Morse-Witten bubbles which are in contact, but a naive check of the extensions along the line between their centres (indicated in light grey) would fail to capture the contact. The plane of the cross-section is defined by the centres of the bubbles and their true contact point, in red. The method suggested generates the light blue curves, which are parabolic approximations to the bubble surface on the centre-centre line. This contact-check then checks if the parabolic curves intersect, and determines the contact point to be at their intersection if so. In the 3D case, these approximations are paraboloids rather than parabolic curves.

Modelling monolayer structures using the Morse-Witten software

Bubble "rafts", a single layer of bubbles floating on top of a liquid, offer a practical and visual framework for understanding the structural principles of crystals [78] or 2D materials [79]. In this analogy, each bubble within the raft represents an individual particle or atom within a crystalline lattice. The critical aspect is the regular and repeating pattern of these bubbles, which closely mirrors the highly ordered atomic arrangement found in crystals. By observing and manipulating the bubble raft, one can gain insights into fundamental concepts of crystallography.

This model is particularly helpful for illustrating the concepts of crystal symmetry, unit cells, and crystal planes. The symmetrical patterns evident in the bubble raft can effectively convey the fundamental principles of crystal symmetry, which underlie the diverse crystal structures found in nature. Additionally, bubble rafts can be intentionally

disrupted to simulate defects or irregularities found in real crystals, offering a tangible way to explore imperfections like vacancies, dislocations, and grain boundaries.

From our simulations, we may assemble these bubble rafts by setting the confining walls of the system to be slightly less than a single bubble diameter apart. Such systems are often realised experimentally to study quasi-2D foams. Here we refer to these structures as monolayers.

The application of these monolayer structures may adapted and expanded to include a variety of other scenarios, one notable example being the task of determining the ground state arrangement for N mutually repelling charges on a plane, which are confined by a harmonic potential. Several interaction potentials - like the well-studied Coulomb interaction, the Yukawa interaction, or the Logarithmic potential - have been rigorously scrutinised to understand their role in charge arrangement. Despite the multitude of interaction potentials examined, there's a surprising regularity in the resulting patterns. Particularly for a small number of charges, N, the charges tend to assemble into highly symmetric configurations that are often identical, irrespective of the specifics of the interaction. The geometric features of these equilibrium structures and their associated energies have been extensively cataloged.

A selection of such minimum energy structures for a given monolayer of Morse-Witten bubbles are shown in Figure 7.5. The deformable nature of these particles gives rise to interesting arrangements, and we believe this work could be further expanded to be compared with work on 2D materials [80] or mathematical studies of packing [81].

7.3 Simulating foams using Morse-Witten theory

Foams have numerous applications in our daily lives, from the frothy head of a beer or the lather of shampoo to the insulating properties of foamed materials in construction. Developing accurate simulation techniques that can capture these bubble packings is essential to gain insights into foam behavior and optimize foam-based processes in

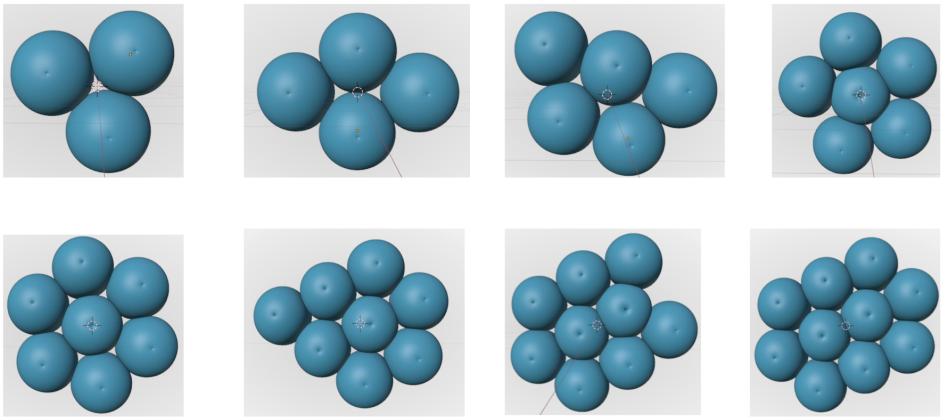

Figure 7.5: Visualisations of the minimum energy arrangements of monolayers of Morse-Witten bubbles with $N = 3 - 10$. Not pictured here are the confining pistons, which lie in the plane of the page and have been removed for visual clarity (though the effect of the contact they form with the bubbles is represented by the 'dimple' of the logarithmic divergence of the Morse-Witten bubble). These structures closely resemble those formed by particles which interact through some long range repulsive interaction, such as the Coulomb or Yukawa potentials.

various industries, ranging from food production to materials science. Accurate simulations are indispensable for advancing our understanding of foam systems and for designing more efficient and tailored applications in both research and industry.

It has been proposed that foams could be modelled as a collection of soft, elastic particles, and that Morse-Witten theory may be employed to study them. In particular, this is useful near the so-called "jamming transition", where contact forces between bubbles are small and bubbles are approximately spherical. To probe this possibility, we have employed the simulation method detailed in Chapter 6, however we have replaced the cylindrically symmetric confining potential with a spherically symmetric one. This has allowed us to study structures which we may expect to find in the interior structure of a bulk foam. An example of such is shown in Figure 7.6. This is just the beginning of applying this simulation method to foams, and we hope to extend its application in future work.

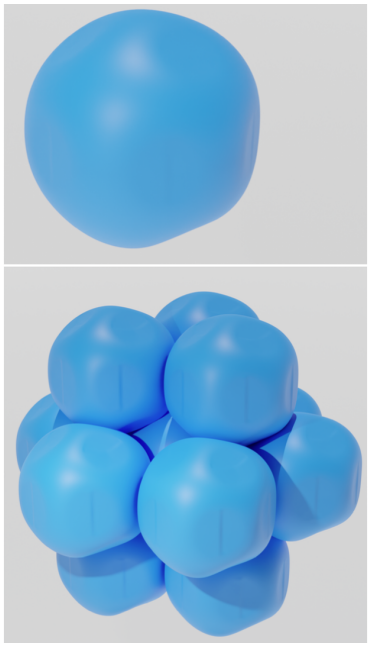

Figure 7.6: An example of a simulation of a unit cell of an FCC foam done within a spherically symmetric confining potential. In this example, the external bubbles of the FCC structure are subject to a harmonic restoring force which acts to move them towards the origin. The upper plot shows the interior bubble and the deformation it experiences due to the action of the exterior bubbles in the cell.

Applying BlenderPhotonics for optical simulations

Monte Carlo photon simulations are sophisticated computational methods employed to emulate the behavior of photons when they interact with substances. These simulations are grounded in principles of probability and ray optics, enabling them to meticulously trace the journey of individual photons as they traverse through a medium and engage with objects or particles [82, 83].

In these simulations, each photon's path is determined through random sampling, taking into account probabilities associated with various possible interactions such as absorption, scattering, and reflection. These probabilities are derived from physics-based models that describe how photons behave in different materials and under varying conditions.

Recently, a package has been developed for Blender which integrates these simulations into the Blender environment. BlenderPhotonics is a Blender add-on that integrates 3-D tetrahedral mesh generation and mesh-based Monte Carlo photon simulations into

the Blender environment. The add-on supports three key workflows: converting 3D Blender objects into labeled tetrahedral meshes and triangular surfaces, converting volumetric images from NIfTI files into labeled tetrahedral meshes, and defining optical properties and light sources for Monte Carlo photon simulations. Users can perform these tasks with a single click on the graphical user interface.

BlenderPhotonics [84] leverages Blender's intuitive computer-aided-design (CAD) interface to combine interactive 3D shape creation and editing with advanced modeling capabilities. This integration enables users, including those with limited experience, to easily create complex domains and perform sophisticated optical simulations, particularly in biophotonics applications [85].

Given the visualisation of our 3D Morse-Witten structures in Blender, we believe that this could be a useful application of this program in order to probe the optical properties of our bubble structures. Interpreting bubble structures using optical methods is essential for determining structures within bulk foams and monitoring foam coarsening [86]. A future application of these 3D Morse-Witten structures could therefore be applying these simulation techniques to probe the optical parameters of bubble structures.

Attractive forces between bubbles: Hanging bubble chains

The transverse confining potential has been a key element of both the experimental and theoretical work done in this thesis. However, it could be asked, how do bubbles arrange themselves in the absence of confinement? Can structures be formed from the balance of forces due to surface tension and gravity?

The idea of 'hanging' bubble chains is not a new one, and one can even obtain a Guinness World Record for chains of exceptional length (at time of writing the record stands at 87!) [7]. Such structures have been modelled experimentally by the group, and presented by photographer Kym Cox as an art exhibition [13].

Work has been done by the group, using Surface Evolver, to model these structures.

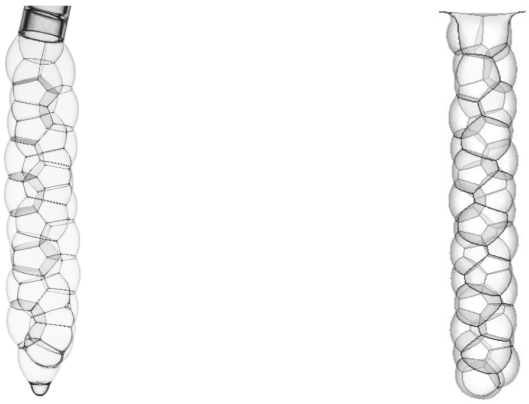

Figure 7.7: Hanging bubble chains. A photo of an experimentally produced example on the left, produced by bubbling air through a narrow tube. The weight of the liquid pulls the resulting bubbles down, assembling the chain shown here. On the right, a Surface Evolver simulation of the same structure. The Surface Evolver structure was generated by comparison with a topologically similar structure that was in a cylindrical confinement. Here the structure is maintained due to the balance between the forces of surface tension and gravity - no confining potential required.

An example of some of these structures is shown in Figure 7.7.

Of course, the addition of an attractive component to the Morse-Witten model could also assist in the other areas of physics where colloidal chains appear. In nanoscience, the assembly of chains of Janus particles [87] or patchy particles [88], which demonstrate a combination of repulsive and attractive interactions depending on their relative orientations, form an important part of the development of nano-machines.

Bibliography

[1] W. Degottardi, D. Sen, S. Vishveshwara, W. Degottardi, D. Sen, and S. Vishveshwara, "Majorana fermions in 1d superconducting wires subject to disorder and other spatial inhomogeneities," *APS*, vol. 2013, p. F27.001, 2013.

[2] Y. Qu, M. Q. Arguilla, Q. Zhang, X. He, and M. Dincă, "Ultrathin, high-aspect ratio, and free-standing magnetic nanowires by exfoliation of ferromagnetic quasi-one-dimensional van der waals lattices," *Journal of the American Chemical Society*, vol. 143, pp. 19 551–19 558, 11 2021.

[3] M. Herranz, C. Pedrosa, D. Martínez-Fernández, K. Foteinopoulou, N. C. Karayiannis, and M. Laso, "Fine-tuning of colloidal polymer crystals by molecular simulation," *Physical Review E*, vol. 107, 6 2023.

[4] R. C. Thompson, "Ion coulomb crystals," *Contemporary Physics*, vol. 56, pp. 63–79, 1 2015.

[5] K. Elibol, T. Susi, C. Mangler, D. Eder, J. C. Meyer, J. Kotakoski, R. G. Hobbs, P. A. van Aken, and B. C. Bayer, "Linear indium atom chains at graphene edges," *npj 2D Materials and Applications 2023 7:1*, vol. 7, pp. 1–8, 1 2023.

[6] C. S. Lacko, I. Singh, M. A. Wall, A. R. Garcia, S. L. Porvasnik, C. Rinaldi, and C. E. Schmidt, "Magnetic particle templating of hydrogels: engineering naturally derived hydrogel scaffolds with 3d aligned microarchitecture for nerve repair," *Journal of neural engineering*, vol. 17, 2020.

[7] Longest bubble chain (hanging) | Guinness World Records.

[8] D. Hoenig, F. Thielemann, L. Karpa, T. Walker, A. Mohammadi, and T. Schaetz, *Phys. Rev. X*, vol. 8, p. 021028, May 2018.

[9] X. Wang, B. Sprinkle, H. K. Bisoyi, T. Yang, L. Chen, S. Huang, and Q. Li, "Colloidal tubular microrobots for cargo transport and compression," *Proceedings of the National Academy of Sciences of the United States of America*, vol. 120, 9 2023.

[10] H.-K. Chan and J. Winkelmann, *Columnar Structures of Spheres*. Jenny Stanford Publishing, 2023.

[11] M. Cetina, A. Bylinskii, L. Karpa, D. Gangloff, K. M. Beck, Y. Ge, M. Scholz, A. T. Grier, I. Chuang, and V. Vuletić, "One-dimensional array of ion chains coupled to an optical cavity," *New Journal of Physics*, vol. 15, p. 053001, 5 2013.

[12] Y. Kikkawa, "Formation of 2d structures and their transformation by external stimuli: a scanning tunneling microscopy study," *Polymer Journal*, vol. 45, pp. 255–260, 2013.

[13] Kym Cox: Work + statement + exhibitions-work + statement + exhibitions.

[14] A. V. Straube, R. P. Dullens, L. Schimansky-Geier, and A. A. Louis, "Zigzag transitions and nonequilibrium pattern formation in colloidal chains," *Journal of Chemical Physics*, vol. 139, 10 2013.

[15] M. Mielenz, J. Brox, S. Kahra, G. Leschhorn, M. Albert, T. Schaetz, H. Landa, and B. Reznik, "Trapping of topological-structural defects in coulomb crystals," *Physical Review Letters*, vol. 110, 3 2013.

[16] L. Euler, *The rational mechanics of flexible or elastic bodies : 1638-1788 : introduction to Leonhardi Euleri Opera Omnia / vol. 10. et 11., seriei secundae.* Auctoritate et impensis Societatis scientiarum naturalium Helveticae, 1980.

[17] B. G. Johnston, "Column buckling theory: Historic highlights," *Journal of Structural Engineering*, vol. 109, pp. 2086–2096, 9 1983.

[18] W. Alhejaili, A. H. Salas, and S. A. El-Tantawy, "Novel approximations to the damped parametric driven pendulum oscillators," *Journal of Mathematics*, vol. 2023, 2023.

[19] C. H. Yoo and S. C. Lee, "Buckling of columns," *Stability of Structures*, pp. 1–73, 1 2011.

[20] D. Bigoni, "Nonlinear solid mechanics: Bifurcation theory and material instability," *Nonlinear Solid Mechanics: Bifurcation Theory and Material Instability*, vol. 9781107025417, pp. 1–532, 1 2012.

[21] B. Grzeszykowski and E. D. Szmigiera, "Experimental investigation on the vertical ductility of rectangular cfst columns loaded axially," *Materials 2022, Vol. 15, Page 2231*, vol. 15, p. 2231, 3 2022.

[22] G. Domokos, P. Holmes, and B. Royce, "Constrained euler buckling," *Journal of Nonlinear Science*, vol. 7, pp. 281–314, 1997.

[23] J. Halkyard, "Floating offshore platform design," *Handbook of Offshore Engineering (2-volume set)*, pp. 419–661, 1 2005.

[24] J. Rauch, "Earnshaw's theorem in electrostatics and a conditional converse to dirichlet's theorem," *Séminaire Laurent Schwartz EDP et applications Année 2013-2014*, 2013.

[25] W. Paul and H. Steinwedel, "Ein neues massenspektrometer ohne magnetfeld," *Zeitschrift fur Naturforschung - Section A Journal of Physical Sciences*, vol. 8, pp. 448–450, 7 1953.

[26] M. Drewsen, "Ion coulomb crystals," *Physica B: Condensed Matter*, vol. 460, pp. 105–113, 3 2015.

[27] H. Totsuji and J. L. Barrat, "Structure of a nonneutral classical plasma in a magnetic field," *Physical Review Letters*, vol. 60, p. 2484, 6 1988.

[28] H. Totsuji, "Two-dimensional system of charges in cylindrical traps," *Physical Review E*, vol. 47, p. 3784, 5 1993.

[29] M. G. Raizen, J. M. Gilligan, J. C. Bergquist, W. M. Itano, and D. J. Wineland, "Ionic crystals in a linear paul trap," *Physical Review A*, vol. 45, p. 6493, 5 1992.

[30] P. F. Herskind, A. Dantan, J. P. Marler, M. Albert, and M. Drewsen, "Realization of collective strong coupling with ion coulomb crystals in an optical cavity," *Nature Physics*, vol. 5, no. 7, pp. 494–498, 2009.

[31] D. Weaire, S. Hutzler, A. Irannezhad, and K. Cox, "Physics in a small bedroom," *Imagine Math 8: Dreaming Venice*, pp. 333–343, 9 2022.

[32] J. Winkelmann, A. Mughal, D. B. Williams, D. Weaire, and S. Hutzler, "Theory of rotational columnar structures of soft spheres," *Physical Review E*, vol. 99, 2019.

[33] J. Winkelmann, B. Haffner, D. Weaire, A. Mughal, and S. Hutzler, "Simulation and observation of line-slip structures in columnar structures of soft spheres," *Physical Review E*, vol. 96, 2017.

[34] S. Hutzler, A. Mughal, J. Ryan-Purcell, A. Irannezhad, and D. Weaire, "Buckling of a linear chain of hard spheres in a harmonic confining potential: Numerical and analytical results for low and high compression," *Physical Review E*, vol. 102, p. 022905, 2020.

[35] A. Irannezhad, D. Weaire, A. Mughal, J. Ryan-Purcell, and S. Hutzler, "Buckling of a tilted line of confined hard spheres," *Philosophical Magazine*, vol. 102, pp. 2506–2524, 2022.

[36] S. Hutzler, J. Ryan-Purcell, A. Mughal, and D. Weaire, "A continuum description of the buckling of a line of spheres in a transverse harmonic confining potential," *Royal Society Open Science*, vol. 10, 7 2023.

[37] T. Lee, K. Gizynski, and B. A. Grzybowski, "Non-equilibrium self-assembly of monocomponent and multicomponent tubular structures in rotating fluids,"

Advanced Materials, vol. 29, p. 1704274, 12 2017.

[38] J. Winkelmann, "Structures of columnar packings with soft and hard spheres," Ph.D. dissertation, 03 2020.

[39] H. L. Partner, R. Nigmatullin, T. Burgermeister, J. Keller, K. Pyka, M. B. Plenio, A. Retzker, W. H. Zurek, A. D. Campo, and T. E. Mehlstäubler, "Structural phase transitions and topological defects in ion coulomb crystals," *Physica B: Condensed Matter*, vol. 460, pp. 114–118, 3 2015.

[40] K. Pyka, J. Keller, H. L. Partner, R. Nigmatullin, T. Burgermeister, D. M. Meier, K. Kuhlmann, A. Retzker, M. B. Plenio, W. H. Zurek, A. D. Campo, and T. E. Mehlstäubler, "Topological defect formation and spontaneous symmetry breaking in ion coulomb crystals," *Nature Communications*, vol. 4, 2013.

[41] D. Weaire, A. Irannezhad, A. Mughal, and S. Hutzler, "A simple experimental system to illustrate the nonlinear properties of a linear chain under compression," *American Journal of Physics*, vol. 88, pp. 347–352, 5 2020.

[42] A. Mughal, D. Weaire, and S. Hutzler, "Peierls-nabarro potential for a confined chain of hard spheres under compression," *EPL*, vol. 135, p. 26002, 2021.

[43] J. Winkelmann, A. Mughal, D. Weaire, and S. Hutzler, "Equilibrium configurations of hard spheres in a cylindrical harmonic potential," *EPL*, vol. 127, p. 44002, 2019.

[44] D. C. Morse and T. A. Witten, "Droplet elasticity in weakly compressed emulsions," *Europhysics Letters*, vol. 22, p. 549, 6 1993.

[45] S. Hutzler, F. F. Dunne, A. M. Kraynik, and D. Weaire, "The energy of fcc and hcp foams," *Soft Matter*, vol. 16, pp. 8262–8271, 2020.

[46] S. Hutzler, J. Ryan-Purcell, F. Dunne, and D. Weaire, "A simple formula for the estimation of surface tension from two length measurements for a sessile or pendant drop," *Philosophical Magazine Letters*, vol. 98, 2018.

[47] C. A. Schneider, W. S. Rasband, and K. W. Eliceiri, "Nih image to imagej: 25 years of image analysis," *Nature Methods 2012 9:7*, vol. 9, pp. 671–675, 6 2012.

[48] A. Rogava, "Tennis-ball towers," *Physics World*, vol. 32, p. 25, 5 2019.

[49] O. Vallée and M. Soares, *Airy functions and applications to physics*. Imperial College Press, 2010.

[50] I. Kovacic, L. Cveticanin, M. Zukovic, and Z. Rakaric, "Jacobi elliptic functions: A review of nonlinear oscillatory application problems," *Journal of Sound and Vibration*, vol. 380, pp. 1–36, 10 2016.

[51] D. Weaire, A. Mughal, J. Ryan-Purcell, and S. Hutzler, "Description of the buckling of a chain of hard spheres in terms of jacobi functions," *Physica D: Nonlinear Phenomena*, vol. 433, p. 133177, 2022.

[52] M. Abramowitz and I. A. Stegun, *Handbook of Mathematical Functions*. Dover Publications, New York, 1965.

[53] Wolfram Mathematica: Modern technical computing.

[54] A. Yamilov, S. E. Skipetrov, T. W. Hughes, M. Minkov, Z. Yu, and H. Cao, "Anderson localization of electromagnetic waves in three dimensions," *Nature Physics 2023 19:9*, vol. 19, pp. 1308–1313, 6 2023.

[55] S. Hilgenfeldt, S. Erisken, and R. W. Carthew, "Physical modeling of cell geometric order in an epithelial tissue," *Proceedings of the National Academy of Sciences of the United States of America*, vol. 105, pp. 907–911, 1 2008.

[56] B. A. Puthenveettil, A. Saha, S. Krishnan, and E. J. Hopfinger, "Shape parameters of a floating bubble," *Physics of Fluids*, vol. 30, p. 112105, 11 2018.

[57] N. Vogel, M. Retsch, C. A. Fustin, A. D. Campo, and U. Jonas, "Advances in colloidal assembly: The design of structure and hierarchy in two and three dimensions," *Chemical Reviews*, vol. 115, pp. 6265–6311, 7 2015.

[58] D. J. Durian, "Bubble-scale model of foam mechanics:mmelting, nonlinear behavior, and avalanches," *Physical Review E - Statistical Physics, Plasmas, Fluids, and Related Interdisciplinary Topics*, vol. 55, pp. 1739–1751, 1997.

[59] K. A. Brakke, "The surface evolver," *Experimental Mathematics*, vol. 1, pp. 141–165, 1992.

[60] R. Höhler and D. Weaire, "Can liquid foams and emulsions be modeled as packings of soft elastic particles?" *Advances in Colloid and Interface Science*, vol. 263, pp. 19–37, 2019.

[61] F. Behroozi, "Soap bubbles in paintings: Art and science," *American Journal of Physics*, vol. 76, pp. 1087–1091, 12 2008.

[62] D. L. Weaire and S. Hutzler, *The physics of foams*. Oxford University Press, 1999.

[63] S. Misra and Y. Jin, "Effects of wettability of conductive and nonconductive particles on the multifrequency electromagnetic response of porous material," *Multifrequency Electromagnetic Data Interpretation for Subsurface Characterization*, pp. 145–170, 1 2021.

[64] F. F. Dunne, J. Winkelmann, D. Weaire, and S. Hutzler, "Implementation of morse–witten theory for a polydisperse wet 2d foam simulation," *https://doi.org/10.1080/14786435.2019.1624852*, vol. 99, pp. 2303–2320, 9 2019.

[65] M. Rayner, G. Trägårdh, C. Trägårdh, and P. Dejmek, "Using the surface evolver to model droplet formation processes in membrane emulsification," *Journal of Colloid and Interface Science*, vol. 279, pp. 175–185, 11 2004.

[66] G. Ginot, R. Höhler, S. Mariot, A. Kraynik, and W. Drenckhan, "Juggling bubbles in square capillaries: an experimental proof of non-pairwise bubble interactions," *Soft Matter*, vol. 15, pp. 4570–4582, 6 2019.

[67] M. Pasquet, N. Galvani, A. Requier, S. Cohen-Addad, R. Höhler, O. Pitois, E. Rio, A. Salonen, and D. Langevin, "Coarsening transitions of wet liquid foams under microgravity conditions," *Soft Matter*, vol. 19, pp. 6267–6279, 8 2023.

[68] H. Elghannay, D. Tafti, and K. Yu, "Evaluation of physics based hard-sphere model with the soft sphere model for dense fluid-particle flow systems," *International Journal of Multiphase Flow*, vol. 112, pp. 100–115, 3 2019.

[69] D. Weaire, R. Höhler, and S. Hutzler, "Bubble-bubble interactions in a 2d foam, close to the wet limit," *Advances in Colloid and Interface Science*, vol. 247, pp. 491–495, 9 2017.

[70] scipy.optimize.fsolve — scipy v1.11.2 manual.

[71] S. Y. Joshi and S. A. Deshmukh, "A review of advancements in coarse-grained molecular dynamics simulations," *Molecular Simulation*, vol. 47, pp. 786–803, 7 2021.

[72] F. Pezoa, J. L. Reutter, F. Suarez, M. Ugarte, and D. Vrgoč, "Foundations of json schema," in *Proceedings of the 25th International Conference on World Wide Web*. International World Wide Web Conferences Steering Committee, 2016, pp. 263–273.

[73] B. O. Community, *Blender - a 3D modelling and rendering package*, Blender Foundation, Stichting Blender Foundation, Amsterdam, 2018.

[74] E. W. Weisstein, "Lambert w-function," *Wolfram Research, Inc.*, 2023.

[75] Z. Lai, Y. Xia, and Q. Chen, "Discrete element modeling of granular hopper flow of irregular-shaped deformable particles," *Advanced Powder Technology*, vol. 34, 9 2023.

[76] D. Weaire, V. Langlois, M. Saadatfar, and S. Hutzler, *Foam as granular matter*. World Scientific Publishing Co., 1 2007.

[77] T. E. Baker and A. Bill, "Jacobi elliptic functions and the complete solution to the bead on the hoop problem," *American Journal of Physics*, vol. 80, pp. 506–514, 6 2012.

[78] B. Behera and C. Kalelkar, "The inveterate tinkerer: Bubble raft," *Resonance*, vol. 22, pp. 801–807, 8 2017.

[79] K. Burson, M. Heyde, and H.-J. Freund, "Looking into the structure of glass by designing a new 2d material," *Bunsen-Magazin*, vol. 19, no. 1, pp. 4–12, 2017.

[80] G. Zou, X. Yi, W. Zhu, and H. Gao, "Packing of flexible 2d materials in vesicles," *Journal of Physics D: Applied Physics*, vol. 51, no. 22, p. 224001, 2018.

[81] A. Irannezhad, A. Baragry, D. Weaire, A. Mughal, and S. Hutzler, "Packing soft spheres: experimental demonstrations with hydrogels," *European Journal of Physics*, vol. 44, p. 065501, 2023.

[82] D. Rogers, "Fifty years of monte carlo simulations for medical physics," *Physics in Medicine & Biology*, vol. 51, no. 13, p. R287, 2006.

[83] Q. Fang and D. A. Boas, "Monte carlo simulation of photon migration in 3d turbid media accelerated by graphics processing units," *Optics express*, vol. 17, no. 22, pp. 20 178–20 190, 2009.

[84] Y. Zhang and Q. Fang, "Blenderphotonics–an integrated computer-aided design, meshing and monte carlo simulation environment for biophotonics," in *Optics and the Brain*. Optica Publishing Group, 2022, pp. BM2C–4.

[85] F. Verhaegen and J. Seuntjens, "Monte carlo modelling of external radiotherapy photon beams," *Physics in medicine & biology*, vol. 48, no. 21, p. R107, 2003.

[86] J. Guerrero, E. Mejia-Ospino, and R. Cabanzo, "Monitoring foam coarsening using a computer optical mouse as a dynamic laser speckle measurement senso," *Pramana - Journal of Physics*, vol. 81, pp. 987–994, 12 2013.

[87] H. Su, C. A. H. Price, L. Jing, Q. Tian, J. Liu, and K. Qian, "Janus particles: design, preparation, and biomedical applications," *Materials Today Bio*, vol. 4, p. 100033, 9 2019.

[88] Z. Zhang and S. C. Glotzer, "Self-assembly of patchy particles," *Nano Letters*, vol. 4, pp. 1407–1413, 8 2004.

[89] A. T. Tyowua, A. M. Echendu, and S. O. Adejo, "Influence of particle fluorination on the stability of honey foam," *Frontiers in Soft Matter*, vol. 3, 6 2023.

[90] K. Takahashi and N. Masumoto, "A non-iterative method to evaluate surface tension and contact angle simultaneously by a sessile drop in gravity using universal figures," *Welding International*, vol. 35, pp. 230–239, 2021.

[91] M. Song, N. Mehrabian, S. Karuturi, and M. D. Dickey, "Jumping liquid metal droplets controlled electrochemically," *Applied Physics Letters*, vol. 118, p. 081601, 2 2021.

[92] J. Winkelmann, F. F. Dunne, V. J. Langlois, M. E. Möbius, D. Weaire, and S. Hutzler, "2d foams above the jamming transition: Deformation matters," *Colloids and Surfaces A: Physicochemical and Engineering Aspects*, vol. 534, pp. 52–57, 12 2017.

[93] H. Hu, C. R. Weinberger, and Y. Sun, "Effect of nanostructures on the meniscus shape and disjoining pressure of ultrathin liquid film," *Nano Letters*, vol. 14, pp. 7131–7137, 12 2014.

A1 The discrete system: Uniform zig-zag

If periodic boundary conditions are applied to a finite chain (with even sphere number) then a simple solution is provided by a sphere arrangement where all transverse displacements are identical. This corresponds to $\theta_n = \theta$ and $F_n = F$ for all values of n. We refer to this as the *uniform zig-zag structure*.

From the discrete iterative equations (Section 2.2) we obtain the following relationship between transverse forces (displacements) F and compressive forces G, for this structure

$$F = 2G \sin\theta. \tag{A1.1}$$

The geometry of the zig-zag structure results in $\sin\theta = 2F$, i.e. $G = 1/4$ for the compressive force between contacting spheres, independent of the value of compression. The longitudinal component of this force, G_0 is thus given by

$$\mathcal{G} = G\cos\theta = \frac{1}{4}\cos\theta. \tag{A1.2}$$

The compressive force at each end of the chain, thus *decreases* with compression, since compression leads to an increase in the angle θ. This implies the instability of the uniform zig-zag structure.

A2 Non-dimensional quantities for the experimental system

In our experiments with hard spheres the restoring transverse force is provided by the curvature of the cylinder, see Fig A2.1. Transverse displacement Y of a sphere of mass m is opposed by a gravitational force $(2Ymg/(D_T - T))\,[1 - 4(Y/(D_T - D))^2]^{-1/2} \simeq (2Ymg/(D_T - T))\,(1 + 2(Y/(D_T - D))^2)$, where D_T and D are cylinder and sphere diameter, respectively. The maximum displacement is about $D/2$ (doublet structure) and we thus obtain $2(Y/(D_T - D))^2 \simeq 0.08 \ll 1$. The restoring force is thus approximated linear in displacement Y with a force constant k_p of

$$k_p = 2mg/(D_T - D). \tag{A2.1}$$

In a cylinder tilted by an angle α against the horizontal, a sphere exerts a longitudinal force $mg \sin\alpha$ on its contacting neighbouring (in the direction of tilt) sphere. As in our modelling of the discrete system we introduce τ as a non-dimensional tilt variable via

$$\tau = mg \sin\alpha/(k_p D). \tag{A2.2}$$

Inserting for k_p (Eqn A2.1) we obtain

$$\tau = \frac{1}{2}\left(\frac{D_T}{D} - 1\right)\sin\alpha. \tag{A2.3}$$

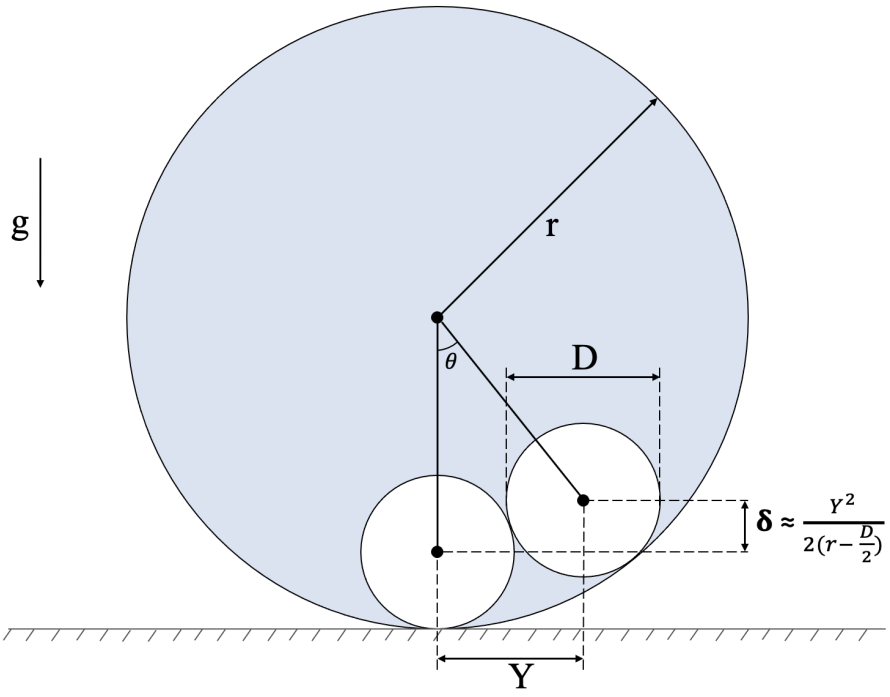

Figure A2.1: Diagram showing the geometry of the hard spheres held against the curved surface of the tube, which can be used to relate the physical dimensions of the system to k_p, the (approximate) spring constant of the confining potential. (See also [51]).

A3 The continuum model

A3.1 Transition to the continuous formulation

In a continuum description both the angle θ (or ϕ) and the transverse force F are functions of a continuous variable u. The approximate continuum representation of the iterative relations, Section 2.2, may then be obtained as follows, where for the simplicity of the argument we initially set $\tau = 0$.

Using the first of the iterative equations Eqn (2.6), we obtain

$$y_n + y_{n+1} = \mathcal{G}(\phi_{n+1} + 2\phi_n + \phi_{n-1}). \tag{A3.1}$$

Re-expressing the left hand side using the second iterative equation, Eqn (2.5), results in

$$\frac{\phi_n}{\sqrt{1+\phi_n^2}} = \mathcal{G}(\phi_{n+1} - 2\phi_n + \phi_{n-1}) + 4\mathcal{G}\phi_n, \tag{A3.2}$$

where $\phi_n = \tan\theta_n$.

The term in brackets on the r.h.s. may be identified as a central difference approximation of the second derivative of a continuous function $\phi(u)$ with respect to a continuous variable u, evaluated at $u = n$. A continuum formulation of this equation is thus given by

$$\phi''(u) = -4\phi(u) + \frac{\phi(u)}{\mathcal{G}\sqrt{1+\phi^2(u)}}, \tag{A3.3}$$

$\mathcal{G}$ is the compressive force exerted at both ends of the chain.

As in the discrete formulation, the presence of tilt makes the compressive force between contacting spheres a linear function of the sphere number. We thus replace the constant $\mathcal{G}$ by

$$G(u) = \mathcal{G} + \tau u, \tag{A3.4}$$

to arrive at

$$\phi''(u) = -4\phi(u) + \frac{\phi(u)}{G(u)\sqrt{1+\phi^2(u)}}. \tag{A3.5}$$

We will call Eqn (A3.5) the *full continuous equation with tilt*. This is the differential equation that is the basis of the continuous description used here.

A3.2 Compression and energy in the continuous formulation

It remains to develop corresponding expressions for compression Δ and energy E, for a given profile $\phi(u)$. Compression in the discrete representation is given by Eqn (2.7); in the continuous formulation (with $\phi = \tan\theta$) this translates into

$$\Delta = \int_0^N (1 - \cos(\arctan\phi(u)))\, du = \int_0^N \left(1 - (1+\phi^2(u))^{-1/2}\right) du. \tag{A3.6}$$

For $\phi(u) \ll 1$, consistent with the approximation that is the general basis of the continuous formulation, we obtain

$$\Delta \simeq \frac{1}{2}\int_0^N \frac{\phi^2(u)}{1+\phi^2(u)/2} du \simeq \frac{1}{2}\int_0^N \phi^2(u) du. \tag{A3.7}$$

An expression for the energy of a solution $\phi(u)$ of the continuum equation requires an integral formulation of Eqn (2.2). Similar to the transition from ϕ_n to $\phi(u)$ we introduce a continuous function $F(u)$ with respect to a continuous variable u, which corresponds to F_n when evaluated at $u = n$. Using the linear interpolation $F(u+1/2) \simeq \frac{1}{2}(F(u) + F(u+1)$, together with the original iterative relationship

Eqn (2.6) we obtain an approximate expression for the displacement $F(u+1/2)$ in terms of $\phi(u)$,

$$F^2(u+1/2) \simeq \frac{1}{4}\frac{\phi^2(u)}{1+\phi^2(u)}. \tag{A3.8}$$

Using the expression for the total energy in the discrete case, Eqn (2.10), we can write its equivalent for the continuum formulation as

$$E = \frac{1}{2}\int_1^N F^2(u)du + \tau\left(\int_0^N \frac{udu}{\sqrt{1+\phi^2(u)}}\right) \simeq \frac{1}{8}\int_0^N \frac{\phi^2(u)}{1+\phi^2(u)}du + \tau\left(\int_0^N \frac{udu}{\sqrt{1+\phi^2(u)}}\right). \tag{A3.9}$$

We note that for the case of the straight chain ($\phi(u) = 0$ for $0 \leq u \leq N$) this expression reduces to $E_s = \tau N^2/2$, i.e. the same expression as in the discrete case (Eqn (2.10)).

For $\phi(u) \ll 1$, and correct to order ϕ^2, we thus obtain

$$E \simeq \frac{\Delta}{4} + \frac{\tau}{2}\left(N^2 - \int_0^N u\phi^2(u)du\right), \tag{A3.10}$$

where we have used Eqn (A3.7) for compression Δ.

If we approximate $\phi(u)$ by a triangular profile, Eqn (A3.10) can be evaluated to give the following expression for E_b, i.e. the energy difference between straight and buckled chain,

$$E - E_s \simeq \frac{\Delta}{4}(1 - 2\tau N), \tag{A3.11}$$

to lowest order in compression Δ and tilt τ.

A3.3 Relation to the Airy equation

To study the variation of the displacement peak for small compression, Δ, we found it sufficient to consider a linearisation of the full equation, Eqn(A3.5), in both ϕ and τ,

$$\phi'' = \left[\frac{1}{\mathcal{G}}\left(1 - \frac{\tau u}{\mathcal{G}}\right) - 4\right]\phi. \tag{A3.12}$$

By introducing a linear change of variables from u to x via

$$x = \left(\frac{\tau}{\mathcal{G}^2}\right)^{-2/3} \left[\frac{1}{\mathcal{G}}\left(1 - \frac{\tau u}{\mathcal{G}}\right) - 4\right], \tag{A3.13}$$

and renaming $\phi = y$ we can rewrite this linearised reduced equation as

$$y''(x) = xy(x). \tag{A3.14}$$

This is the Airy differential equation which has analytical solutions in terms of the Airy *Ai* and *Bi* functions,

$$y(x) = c_1 \mathrm{Ai}(x) + c_2 \mathrm{Bi}(x) \tag{A3.15}$$

with constants c_1 and c_2.

We want to find a solution $\phi(u)$ which is zero at the two endpoints $u = 0$ and $u = N$. Expressed in terms of $y(x)$ this corresponds to (from Eqn (A3.13)) $y(x_1) = y(x_2) = 0$, with

$$x_1 = \left(\frac{\tau}{\mathcal{G}^2}\right)^{-2/3} \left[\frac{1}{\mathcal{G}} - 4\right], \quad x_2 = \left(\frac{\tau}{\mathcal{G}^2}\right)^{-2/3} \left[\frac{1}{\mathcal{G}}\left(1 - \frac{\tau N}{\mathcal{G}}\right) - 4\right]. \tag{A3.16}$$

It remains to fix the constants c_1 and c_2 in Eqn A3.15. From the boundary condition $y(x_1) = 0$ we obtain

$$c_2/c_1 = -\frac{\mathrm{Ai}(x_1)}{\mathrm{Bi}(x_1)} = -\frac{\mathrm{Ai}(x_2)}{\mathrm{Bi}(x_2)}, \tag{A3.17}$$

and we can thus write the solution $y(x)$, Eqn (A3.15), as

$$y(x) = c_1 \left(\mathrm{Ai}(x) - \frac{\mathrm{Ai}(x_1)}{\mathrm{Bi}(x_1)}\mathrm{Bi}(x)\right). \tag{A3.18}$$

The constant c_1 can be expressed in terms of compression, Δ, as follows.

For $\phi \ll 1$ compression, Δ, is given by Eqn (A3.7) as

$$\Delta = \frac{1}{2}\int_0^N \phi^2(u)du = f(\tau,\mathcal{G})\int_{x_1}^{x_2} y(x)^2 dx, \tag{A3.19}$$

with the prefactor $f(\tau,\mathcal{G}) = \frac{4-\frac{1}{\mathcal{G}}(1-\frac{\tau N}{\mathcal{G}})}{2(\frac{\tau}{\mathcal{G}^2})^{1/3}}$. For our Airy function solution, Eqn (A3.15), this integral over $y(x)^2$ can be computed analytically to result in

$$\Delta = f(\tau,\mathcal{G})\left(y'(x_2)^2 - y'(x_1)^2\right) \tag{A3.20}$$

Compression is thus expressed in terms of the slopes $y'(x)$ at the two endpoints, x_1, x_2. Using our solution for $y(x)$, Eqn (A3.18), this results in

$$\Delta = c_1^2 f(\tau,\mathcal{G})\left[\left(Ai'(x_2) - \frac{Ai(x_1)}{Bi(x_1)}Bi'(x_2)\right)^2 - \left(Ai'(x_1) - \frac{Ai(x_1)}{Bi(x_1)}Bi'(x_1)\right)^2\right], \tag{A3.21}$$

and thus provides an expression for the constant c_1 in terms of compression Δ, tilt τ, compressive force $\mathcal{G}$ and sphere number N. We can revert from $y(x)$ to $\phi(u)$ via Eqn (A3.13) and thus have obtained an analytical solution of the linearised reduced equation with tilt, Eqn (A3.12), in terms of these parameters; see Fig 3.6. (Note that from experimenting with Mathematica we find that (for given N) not all pairs of $(\tau,\mathcal{G})$ lead to solutions which fulfill the boundary conditions $y(x_1) = y(x_2) = 0$, with x_1, x_2 defined in Eqn (A3.16).)

A4 Rescaling Jacobi functions

We will show that a solution $\phi(u)$ which satisfies the reduced equation, Eqn 4.3, can be expressed in terms of a Jacobi function $y(x) = cn(x|m)$ for appropriately rescaled variables. Back-substitution then results in the angle profile $\theta(u) = \arctan\phi(u)$.

We proceed by introducing real constants c_1 and c_2, whose value remains to be determined, and set $\theta = c_1 y$ and $u = c_2 x$. The second derivative of ϕ with respect to u is thus given by $\frac{d^2\phi}{du^2} = \frac{c_1}{c_2^2}\frac{d^2y}{dx^2}$.

In the new variables $y(x)$ the reduced equation, Eqn 4.3, is re-written as $\frac{c_1}{c_2^2}\frac{d^2y}{dx^2} = \kappa^2 c_1 y - 2c_1^3 y^3$. This results in our key equation for further analysis,

$$\frac{d^2y}{dx^2} = \kappa^2 c_2^2 y - 2c_1^2 c_2^2 y^3. \tag{A4.1}$$

In this rescaled equation the y^3 term features with a minus sign. This rules out 8 of the 12 Jacobi functions.

Eqn (A4.1) is solved by the Jacobi $cn(x|m)$ function if we set $c_1^2 c_2^2 = m$ and $\kappa^2 c_2^2 = 2m - 1$. Solving for c_1^2 and c_2^2 we obtain $c_2^2 = \frac{2m-1}{\kappa^2}$ and $c_1^2 = \frac{m\kappa^2}{(1+\kappa^2/4)(2m-1)}$.

Using $\phi = c_1 y$ and $x = u/c_2$ from above yields our scaled Jacobi cn solution $\phi(u)$ of the reduced Eqn (4.3),

$$\phi(u) = \tan\theta(u) = \sqrt{\frac{m\kappa^2}{(1+\kappa^2/4)(2m-1)}}\, cn\left(\sqrt{\frac{\kappa^2}{2m-1}}u \middle| m\right), \tag{A4.2}$$

with $\kappa^2 > -4$, as discussed in Appendix A3.1.

We have $0 \leq m \leq 1$, this requires $\kappa^2 < 0$ for $m < 1/2$ and $\kappa^2 > 0$ for $m > 1/2$. $m = 1/2$ can only lead to a solution for $\kappa^2 = 0$ (division 0/0).

Limiting cases:

$m \to 0 : \tan\theta(u) \to \sqrt{m}\sqrt{-\kappa^2/(1+\kappa^2/4)}\cos(\sqrt{-\kappa^2}u)$

$m = \frac{1}{2} : \tan\theta(u) = cn\left(\sqrt{2}u|\frac{1}{2}\right)$

$m = 1 : \tan\theta(u) = \sqrt{\kappa^2/(1+\kappa^2/4)}\mathrm{sech}\left(\sqrt{\kappa^2}u\right)$

Here the case for $m = \frac{1}{2}$ can be obtained by setting $\sqrt{\frac{m\kappa^2}{(1+\kappa^2/4)(2m-1)}} = 1$ and $\frac{\kappa^2}{2m-1} = 2$, from which it follows that $m = \frac{1}{2}$ and $\kappa^2 = 0$.

A4.1 Relevance to the pendulum

The reduced equation, Eqn (4.3), is also relevant to the theory of the mathematical pendulum. The pendulum equation for the angle of displacement $y(t)$ from the vertical is

$$\ddot{y}(t) = -\omega_0^2 \sin y(t), \tag{A4.3}$$

where ω_0^2 is the angular frequency for small amplitude oscillations (i.e. the case of the harmonic oscillator). An *exact* solution for all amplitudes may be expressed in terms of Jacobi functions, but various transformations are required to derive this. An intermediate approximation can be applied using

$$\sin y \simeq y - y^3/6, \tag{A4.4}$$

resulting in

$$\ddot{y}(t) = -\omega_0^2 y^2(t) + \frac{\omega_0^2}{6} y^3(t). \tag{A4.5}$$

This equation may be treated in the manner of Section 4.2.2 to derive a Jacobi solution of the following form:

$$y(t) = y_0 \; cd\left(\omega_0 \sqrt{1 - \frac{y_0^2}{12}} t \middle| \frac{y_0^2}{12 - y_0^2}\right) \tag{A4.6}$$

with initial displacement $y_0 = y(t = 0)$.

The period of this solution, $T = \frac{2\pi}{\omega_0}(1 + \frac{y_0^2}{16} + \mathcal{O}(y_0^4))$ agrees with that of the mathematical pendulum up to order y_0^2.

A5 Morse-Witten theory: Surface tension measurements

Although the presentation of the Morse-Witten theory in the main text focuses on the action of compressive forces on bubbles, it has been shown that the model also works for extensive forces, such as the case of the pendant drop [46].

Previous work on this idea resulted in a method of estimating surface tension of drops by only taking two measurements of the drop, based on the theory of Morse-Witten. The expression in its simplest form is as follows:

$$\gamma = \frac{\Delta\rho g \ln 2}{24} \frac{(L_x + L_y)^3}{|L_x - L_y|}. \tag{A5.1}$$

Where $\Delta\rho$ is the density difference between the droplet and external media, g is acceleration due to gravity, L_x is the maximum equatorial width of the drop, and the L_y is the maximal perpendicular from that width (See Figure A5.1).

Since this work, this formula has been applied to measure the surface tension of honey [89] and water droplets [90], and in metallurgy [91].

Our group, with thanks to Jennifer Quirke, was able to produce high quality images of water droplets. Using these images from both a Digital Single Lens Reflex camera (DSLR) and a Tensiometer, the formula was applied to find the estimated surface tension. The results are shown in Figure A5.2.

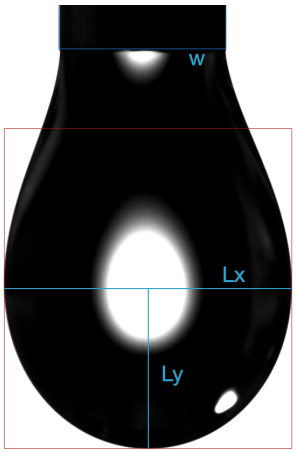

Figure A5.1: A pendant drop of millipore water hanging from a nozzle with width 2.08mm (thanks to Jennifer Quirke for this image). A bounding box is defined (in red) which sets the measurements L_x, L_y. The nozzle width w is used to define the conversion between pixels and mm.

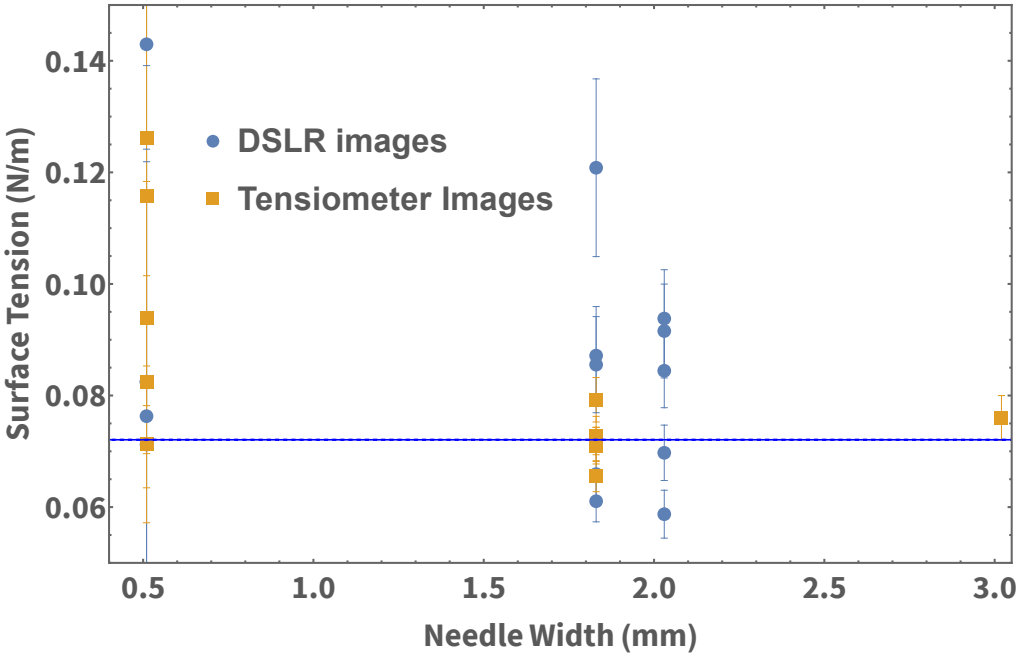

Figure A5.2: Predictions of the surface tension of a droplet of water taken from DSLR and Tensiometer images. The horizontal blue line represents the prediction made by standard experimental methods for measuring surface tension from a droplet profile. Of note is the improvement in agreement as the needle size is increased - an effect of the sensitivity of Eqn (A5.1) on the measurement of the parameters L_x and L_y.

Figure A5.3: A photo of the Trinity College Dublin pitch drop experiment (image credit Jennifer Quirke). At time of writing the experimental apparatus is available to view in the Library, and the current drop would be expected to break off around 6 years from now.

The issues raised in [46] persist in that, even with the correction factors proposed in that paper, the accuracy of the measurement has a large bearing on the resulting value of surface tension.

The method could be of use in situations such as the famous 'pitch drop' experiments, pictured in Figure A5.3. These long-running experiments, one of which is located in Trinity College Dublin (in the main Library at the time of writing), consist of funnels full of pitch (bitumen) , the viscosity of which is estimated to be two million times greater than that of honey. The pendant drop shape that develops could be used to make an estimate of the surface tension of the pitch, provided high enough quality photographs were available.

A6 Analytic expressions for buckled lines of bubbles

Let F be the force acting on a bubble due to contact with the other bubble. The bubble centres are a distance L apart. We will call the angle between the line of contact and the axial direction is called θ, the buckling angle. In equilibrium there is a balance of transverse forces exerted on a given bubble, i.e. the forces $F\sin\theta$ and the transverse restoring force $k_p\frac{L}{2}\sin\theta$, where k_p is the spring constant of the confining potential,

$$F\sin\theta = k_p\frac{L}{2}\sin\theta. \tag{A6.1}$$

Let the interaction between the spheres be governed by a generic function $F = F(L)$ which depends on the distance L between bubble centres. From Eqn (A6.1) we obtain

$$F(L) = \frac{k_p L}{2} \tag{A6.2}$$

This equation defines a value for L which is *independent* of the buckling angle θ, which w call L_c (the distance between sphere centres associated with a buckled arrangement).

The balance of axial forces exerted on a bubble, where F_w is the force due to the bubble-wall contact, is given by

$$F_w = F\cos\theta, \tag{A6.3}$$

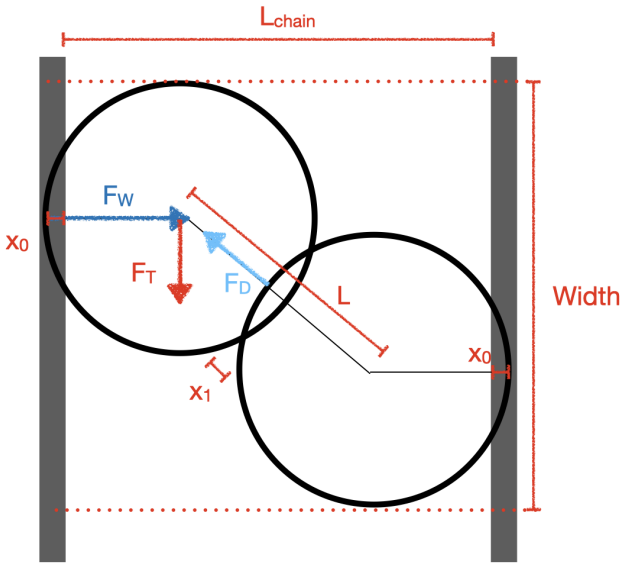

Figure A6.1: A schematic of two bubbles in a buckled structure between two hard walls. Here we represent Morse-Witten contact as overlaps (these will be related to the displacements at the contacts x_i). This diagram forms the basis of the approach used in Section A6

resulting in

$$F_w = \frac{k_p}{2} L_c \cos\theta. \tag{A6.4}$$

Now let us consider the straight chain, i.e. $\theta = 0$. Initially the distance between the two centres is some distance L, which must be determined and depends on the force law. As compression increases, the value of L is expected to decrease up until a critical value is reached. At this point, the system will buckle, and is described by a finite angle θ (which depends on compression), and a constant bubble separation L_c.

From Eqn (A3.7)) compression Δ is given by

$$\Delta = \frac{2W(Bo) - L_{chain}}{W(Bo)} \tag{A6.5}$$

where $W(Bo)$ is given by Eqn (12), i.e. the width of an bubble held under a plate by buoyancy. (In models where bubbles do not deform under applied force, or where there is no contact with a confining surface, $W(Bo) = 2R_0$)

The chain length L_{chain} is given by

$$L_{chain} = (W(Bo) + 2X_0) + (W(Bo) + 2X_1)\cos\theta, \tag{A6.6}$$

where $X_0 < 0$ is the deformation of a bubble at the bubble wall contact and $X_1 < 0$ is the deformation at the bubble-bubble contact, with $L_c = W(Bo) + 2X_1$.

We introduce the dimensionless quantities $x_0 = X_0/(R_0)$ and $x_1 = X_1/(R_0)$ and re-write the chain length of the buckled chain as $L_{chain} = (W(Bo) + 2R_0x_0) + (W(Bo) + 2R_0x_1)\cos\theta$. The compressive strain is then given by

$$\epsilon = 1 - \frac{L_{chain}}{2W(Bo)} = 1 - \frac{1}{2}\left((1 + \frac{2R_0x_0}{W(Bo)}) + (1 + \frac{2R_0x_1}{W(Bo)})\cos\theta\right). \tag{A6.7}$$

In the unbuckled state ($\theta = 0$) this reduces to

$$\epsilon = -\frac{R_0}{W(Bo)}(x_1 + x_0). \tag{A6.8}$$

.

In order to progress we need to relate X_1 and X_0 to each other. This will depend on the model of bubble interaction. In the next section, we shall apply Morse-Witten theory to this general approach.

Application of the Morse-Witten model

Let us again consider the experimental system where we have a pair of bubbles trapped under the top of a cylindrical tube by buoyancy. These bubbles are then compressed by two pistons.

For two contacting bubbles held under a flat plate by buoyancy, the displacement $X = xR_0$ at the bubble-bubble contact and the centre-to-centre distance L between

those two bubbles are related by

$$L = W(Bo)(1 + \frac{2R_0}{W(Bo)}x_1), \tag{A6.9}$$

where $x = x(f_b)$, as it depends on the magnitude of the buoyancy force.

The contact displacement–force relationship (Eqn (5.14)) in the Morse-Witten model for a bubble with three contacts (bubble-piston, bubble-bubble and bubble-top plate) is given by

$$x_i(f_i) = \frac{1}{24\pi}\left(5 + 6\ln(\frac{f_i}{8\pi})\right) f_i - G(\pi - \beta)f_j - G(\pi/2)f_b, \tag{A6.10}$$

where $f_{i,j}$ are non-dimensional forces, $f_{i,j} = F/(\gamma R_0)$. G is the Green's function. β is the buckling angle (see Figure A6.1). The buoyancy force due to the contact with the top plate is:

$$f_b = \frac{\frac{4\pi}{3}\rho g R_0^3}{\gamma R_0} = \frac{4\pi}{3}Bo. \tag{A6.11}$$

In the following we will consider the system *before* the onset of buckling, i.e. a linear chain where the angle β is 0. In this case $f_i = f_j = f$ We thus have $G(\pi - \beta) = G(-\pi) = \frac{5}{24\pi}$, and $G(\pi/2) = -\frac{1}{8\pi}$ resulting in

$$x(f) = \frac{1}{4\pi}f\ln\left(\frac{f}{8\pi}\right) + \frac{f_b}{8\pi} \tag{A6.12}$$

We can invert this equation to obtain $f(x)$ using the Lambert function W_{-1},

$$f = \frac{4\pi x - f_b/2}{W_{-1}(x/2)} \tag{A6.13}$$

We rewrite Eqn (A6.9) in terms of x and use the generic force relationship from Eqn(A6.2) to express the bubble centre-to-centre distance L in terms of the contact

force F. This results in

$$x = L/(2R_0) - \frac{W(Bo)}{2R_0} = \frac{2F}{2R_0 k_p} - \frac{W(Bo)}{2R_0}, \tag{A6.14}$$

i.e.

$$x(f) = \frac{\gamma}{k_p} f - \frac{W(Bo)}{2R_0}. \tag{A6.15}$$

Inserting Eqn (A6.12) for $x(f)$ results in the following equation which can be solved numerically using Mathematica to obtain a solution for f_c

$$\frac{W(Bo)}{2R_0} + \frac{f}{4\pi}\left(\ln\frac{f}{8\pi} - 4\pi\frac{\gamma}{k_p}\right) + \frac{f_b}{8\pi} = 0 \tag{A6.16}$$

It is now possible to relate this solution to the ratio γ/k_p, a measure of the 'hardness' of the bubbles relative to the strength of the transverse confining potential. We find that in the case of of bubbles trapped under the curved surface of a cylinder, we have:

$$\gamma/k_p = \frac{\frac{D_T}{D} - 1}{4/3\pi Bo}, \tag{A6.17}$$

(see Appendix A2), thus:

$$\frac{W(Bo)}{2R_0} + \frac{f}{4\pi}\left(\ln\frac{f}{8\pi} - \frac{3}{Bo}\left(\frac{D_T}{D} - 1\right)\right) + \frac{Bo}{6} = 0. \tag{A6.18}$$

The addition of the $Bo/6$ term is due to the contact with the top plate.

The length of the buckled chain is given by Eqn(A6.6). Below the critical compressive strain for buckling the displacements at the bubble-wall and the bubble-bubble contacts are identical, $x_0 = x_1$, $\theta = 0$, and we obtain $L_{chain} = 2(W(Bo) + 2X)$. From the compression $\Delta = -4X/W(Bo)$ we obtain for the compressive strain

$$\epsilon = -\frac{2x}{w(Bo)}, \tag{A6.19}$$

where we have introduced $x = X/R_0$, and $w(Bo) = W(Bo)/R_0$ is as can be obtained

from Eq (A6.8).

The compressive strain for buckling is thus given, from Eqn(A6.15), by

$$\epsilon_c = \left(\frac{w(Bo)}{2} - \frac{\frac{D_T}{D} - 1}{4/3\pi Bo} f_c \left(Bo, D_T/D \right) \right) \frac{2}{w(Bo)}. \tag{A6.20}$$

A6.1 Buckling in the Morse-Witten Bubble chain

Up to the onset of buckling the displacements/forces at bubble-bubble and bubble-wall contact were identical, $x_1 = x_2$. We know from our general treatment of buckling in the previous section that the centre-centre distance of the two contacting bubbles is independent of the buckling angle θ.

The displacement of the bubble-wall contact is given by

$$x_0(f_1, f_2, \theta) = \frac{1}{24\pi} \left(5 + 6 \ln(\frac{f_0}{8\pi}) \right) f_0 - G(\pi - 2\theta) f_1 - G(\pi/2) f_b. \tag{A6.21}$$

Its θ-dependence is only via the Green's function $G(\pi - 2\theta)$, which for small buckling angles can be approximated by a constant, $G(\pi - 2\theta) \simeq G(\pi) = 5/(24\pi)$. We can thus also treat x_0 as a constant just above the buckling onset, and maintain $x_0 = x_1 = x_c$ also for $\epsilon > \epsilon_c$.

Eqn (A6.7) is then readily re-written in terms of θ as

$$\theta = \arccos \left(\frac{1 - 2\epsilon - x_c}{1 + x_c} \right), \tag{A6.22}$$

where x_c is value at buckling. From Eqn A6.8 we obtain $x_c = -\epsilon_c$, and thus

$$\theta = \arccos \left(\frac{1 - 2\epsilon + \epsilon_c}{1 - \epsilon_c} \right). \tag{A6.23}$$

From Figure A6.1 we see that the width of the buckled structure Ω is given by

$$\Omega = W(\epsilon_c, Bo) + (R_0(1+x_c) + R_0(1+x_c))\sin\theta = W(\epsilon_c, Bo) + 2R_0(1-\epsilon_c)\sin\theta. \quad \text{(A6.24)}$$

As we have seen above, compression of a straight chain leads to an increase in bubble width, i.e., $W(\epsilon_c) > D$.

Using the identity $\sin\arccos x = \sqrt{1-x^2}$, and Eqns (A6.23) and (A6.24) we obtain:

$$\Delta\omega = \frac{1}{w(\epsilon = 0, Bo)} \left(w(\epsilon_c, Bo) + 2(1-\epsilon_c)\sqrt{1 - \left(\frac{1 - 2\epsilon + \epsilon_c}{1-\epsilon_c}\right)^2} \right), \quad \text{(A6.25)}$$

valid for $\epsilon \geq \epsilon_c$. This simplifies to:

$$\Delta\omega = \frac{1}{w(\epsilon = 0, Bo)} \left(w(\epsilon_c, Bo) + 4\sqrt{\Delta\epsilon(1-\epsilon)} \right), \Delta\epsilon = \epsilon - \epsilon_c. \quad \text{(A6.26)}$$

.

A7 Polydispersity in Morse-Witten theory

Although contacts between bubbles of differing sizes has been studied and implemented in 2D [64, 92], the theory has not been extended to three dimensions ([60] attempted to do so, but we note that the equations as presented in that article for polydisperse Morse-Witten bubbles is incorrect). Here we will generalise the approach detailed for contacts between bubbles with different radii.

We start with a generalisation of Figure 5.2, where we will write our quantities dimensionfully by multiplying by the bubble radius R_i, noting that we no longer have a common R_0 for all bubbles. Thus we find the expression for the displacement at the contact X_c is given by:

$$X_c = R_i(\theta_c)\cos(\theta_c) - R_i, \tag{A7.1}$$

where θ_c is the capping angle for the bubble, as shown in Figure 5.2. We will substitute for $R_i(\theta_c)$ using Eq (5.14):

$$X_c = R_i(1 - fG(\theta_c)\cos(\theta_c) - 1), \tag{A7.2}$$

where $f = F/\gamma R_i$. Assuming the force is small, as is usual for Morse-Witten bubbles, we will expand the Green's function to order θ^2, resulting in the simplified Green's

function:

$$G(\theta) \approx -\frac{1}{4\pi}(11/6 - 2\theta^2/3 + \log\theta^2/4). \tag{A7.3}$$

This results in the simplified form of Eqn (A7.2):

$$X_c/R_i = \frac{f}{24\pi}(11 - 4\theta^2 + 6\log(\theta^2/4)) - \theta^2/2. \tag{A7.4}$$

It can be shown, however, that for a Morse-Witten bubble $f \propto \theta_c^2$ (this can be done by considering the pressure across the circular cap). Thus we shall drop the θ^2 term from the calculation, as multiplication by the prefactor f would result in a term of order f^2, which may be neglected in this linearised theory.

For the case of two bubbles in contact, with radii R_1 and R_2, we must consider the disjoining pressure [93] across their contact:

$$P_d = 1/2\left(\frac{2\gamma}{R_1} + \frac{2\gamma}{R_2}\right). \tag{A7.5}$$

Considering the forces across their caps, we may write:

$$F = P_d\pi\theta_{c,i}^2 R_i^2 = \pi(\theta_{c,i}R_i)^2/2\left(\frac{2\gamma}{R_1} + \frac{2\gamma}{R_2}\right). \tag{A7.6}$$

In this calculation we assume that, as the bubbles are in contact, their capping surfaces have the same area. Thus $(\theta_{c,i}R_i)^2$ is the same for $i = 1, 2$. We can then relate the capping angle to F with:

$$\theta_{c,i}^2 = \frac{F}{\pi R_i\gamma(R_1^{-1} + R_2^{-1})}. \tag{A7.7}$$

Now we may rewrite the expression for the displacement at the contact, $x_i = X_i/R_i$, in terms of this capping angle.

$$x_i = f/24\pi \left(11 + 6\log\left(\frac{F}{4\pi R_i \gamma (R_1^{-1} + R_2^{-1})}\right)\right) - \frac{F}{2\pi R_i \gamma (R_1^{-1} + R_2^{-1})}. \quad \text{(A7.8)}$$

Rewriting $f_i = f/\gamma R_i$ and simplifying, we find the displacement at the contact in terms of f_i:

$$x_i = f_i/4\pi \left(11/6 - \frac{2R_1R_2}{R_i(R_1 + R_2)} + \log\frac{2R_1R_2 f_i}{4\pi R_i(R_1 + R_2)}\right). \quad \text{(A7.9)}$$

Which reduces to the monodisperse expression when $R_1 = R_2 = R_0$.